Faculty of Aerospace Engineering

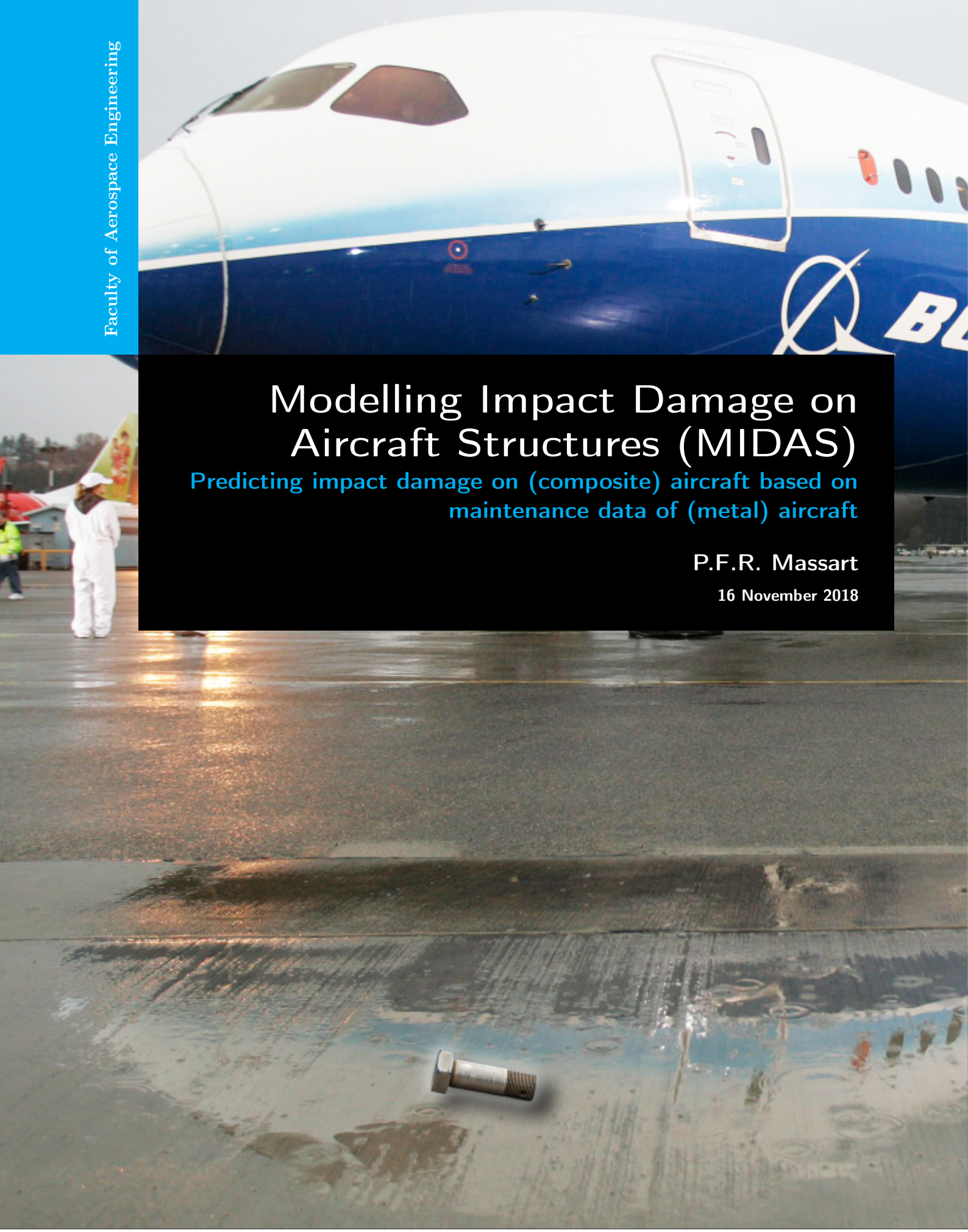

Modelling Impact Damage on Aircraft Structures (MIDAS)

Predicting impact damage on (composite) aircraft based on maintenance data of (metal) aircraft

P.F.R. Massart

16 November 2018

TU Delft Delft University of Technology

Challenge the future

Modelling Impact Damage on Aircraft Structures (MIDAS)

Predicting impact damage on (composite) aircraft based on maintenance data of (metal) aircraft

Master of Science Thesis

For obtaining the degree of Master of Science in Aerospace Engineering
at Delft University of Technology

P.F.R. Massart

16 November 2018

Faculty of Aerospace Engineering · Delft University of Technology

Delft University of Technology

Delft University Of Technology
Department Of
Aerospace Structures and Materials

The undersigned hereby certify that they have read and recommend to the Faculty of Aerospace Engineering for acceptance a thesis entitled **"Modelling Impact Damage on Aircraft Structures (MIDAS)"** by **P.F.R. Massart** in partial fulfillment of the requirements for the degree of **Master of Science**.

Dated: 16 November 2018

Readers:

Prof. dr. C. Kassapoglou

dr.ir. W. J. C. Verhagen

ir. J. Sinke

ir. V. S. V. Dhanisetty

Summary

Historically, civil passenger aircraft were primarily composed of metals. During their service, these aircraft are expected to encounter damage of varying severity. Research shows that impact damage accounts for 50-80% of the damages cases in aircraft structures [1, 2]. As a result, impact damage has a significant economic footprint in the airline industry, of which annual cost estimates range from 1 up to 20 billion USD for the entire airline industry [3–5]. Recently, large passenger aircraft (e.g. the Boeing 787 and the Airbus A350) were introduced into civil aviation using composite materials for more than 50% of the structural weight. The significance of impact damage has thereby only increased [6]. Impact on metal structures results in a dent or penetration of the structure's surface, which are either clearly or reasonably visible [7]. In comparison, impact on composites causes only minor residual indentation, but leads to subsurface damage such as delamination and fiber breakage [8]. These types of damages are generally referred to as Barely Visible Impact Damage (BVID). This reduces the feasibility of visual inspections. In addition, the residual strength is reduced by these subsurface damage types [2, 6, 8–10].

In this thesis, a methodology is presented to predict impact damage on next-generation (composite) aircraft based on maintenance data of in-service (metal) aircraft. To achieve this conversion, an analytical model is developed to Model Impact Damage on Aircraft Structures (MIDAS) for composite (-C) and metal (-M) aircraft. The model characterizes impact threats based on damage dimensions in two steps. First, for a given threat an impact event is approximated, and the corresponding damage is estimated. Second, the analytical model is reverse engineered to deduce the impact threat characteristics from the permanent damage. These two steps are respectively referred to as the inductive and deductive problem. Most methods in literature focus on the inductive problem [11–14], while the deductive problem is not explicitly addressed.

Several simplifications are made to approximate impact events. Aircraft structures are simplified to either clamped or simply supported flat plates. The impact events are assumed to occur on the target's center and perpendicular to its surface. In addition, an impact event is assumed to be boundary dependent and properly approximated as a quasi static event. The effect of mass and impact velocity on the type of impact response is thereby neglected.

To address the impact specific behaviour of metal and composite materials, the two variations of MIDAS are developed respectively referred to as MIDAS-M and MIDAS-C. To develop the functionality of MIDAS-M, this work combines elements of modelling methods proposed by Shivakumar *et al.* [15]; Abrate [11]; Simonsen and Lauridsen [13]; and Lee *et al.* [14]. MIDAS-C, on the other hand, continues on the work of Cairns [16] and Olsson and Block [17]. The methods differ from one another in terms of the assumed mode of deformation and the material specific damage creation. In the metal variant of MIDAS, a new transition region is implemented between the local and global deformation modes based on penetration limits. The composite variant only considers the conventional local and global deformations, but provides a novel approach for the permanent indentation in the post fiber breakage region

The verification of MIDAS is investigated by means of a finite element model (FEM), which is validated by experimental data of Fagerholt *et al.* [18] and Lopes *et al.* [19]. The predictions of MIDAS-M and the metal FEM are in excellent agreement. MIDAS-M is able to reproduce both the force-displacement path and the maximum or permanent deformation shapes in a fraction of the time of the numerical model (i.e. in 20 seconds compared to 12 hours). The predictions of the composite FEM and MIDAS-C, on the other hand, are in good agreement with experimental results before the Damage Threshold Load (DTL), whereas the composite FEM is unable to reproduce the experimental results beyond DTL. The verification of MIDAS-C is therefore deemed inconclusive. A validation of MIDAS-C using experimental impact data (including delamination and fiber breakage) shows that the residual indentation and impact response predictions are again in good agreement.

The novel deductive approach is validated in two conditions: either partially- or not-informed (i.e. with knowledge of the impactor size or without any information of the impact threat). The partially-informed procedure, which only depends on the residual indentation depth, provides estimates with errors below 10% and 30% for respectively the quasi-isotropic and orthotropic laminates. The prediction errors increase to approximately 100% and 200% for respective laminate types in the not-informed case. The increase of this error is directly related to the dent width measurements. These measurements are highly sensitive to human error due to the variation in perceived dent sizes.

The applicability of MIDAS is illustrated by a case study based on structural damage data provided by a major European carrier. Thereby, the feasibility to predict damage on next-generation (composite) aircraft is investigated using maintenance data of in-service (metal) aircraft. The conversion process of MIDAS provides a direct comparison of impact threats to metal and composite aircraft. The results are summarized in a threat map illustrating the low, and high consequence limits for both aircraft types in terms of impactor radius and impact energy.

Concluding, MIDAS provides damage estimates over a wide range of impact scenarios within several minutes compared to time intensive simulations of hours for single impact case using FEM. The promising potential of MIDAS, however, focuses on the cost benefits of relevant impact threat predictions. Such predictions provide a stepping stone for Maintenance, Repair and Overhaul (MRO) organizations to develop successful mitigation of impact risks, which can decrease aircraft down-time and reduce annual maintenance cost. This paves the way to move from a dents-to-dents conversion provided by MIDAS to a dents-to-dollars maintenance practice in airlines.

Table of Content

Summary v

Table of Content xi

List of Figures xiii

List of Tables xv

List of Acronyms xvii

List of Symbols xix

Introduction 1

1 Literature review 3
- 1.1 Definition of impact . . . 3
- 1.2 The impact threat to aircraft structures . . . 4
  - 1.2.1 Identification of impact threats . . . 4
  - 1.2.2 Certification aspects of impact . . . 9
  - 1.2.3 Maintenance aspects related to impact . . . 11
- 1.3 Damage . . . 14
  - 1.3.1 Difference of material response causing damage . . . 14
  - 1.3.2 Expected damage types as function of structural properties . . . 16
  - 1.3.3 Sequence of damage during impact event . . . 16
  - 1.3.4 Characterization of impact resistance . . . 18
  - 1.3.5 Surface damage . . . 19
  - 1.3.6 Damage morphology . . . 20
- 1.4 Modelling of impact event . . . 21
  - 1.4.1 Classification of impact regimes . . . 21
  - 1.4.2 Experimental techniques to perform impact test . . . 22
  - 1.4.3 Structural modelling of impact . . . 22

1.4.4 Finite Element Methods . . . 26
1.4.5 The influence of component properties on the impact response . . . 26

2 Methodology 29

3 Analytical approach of impact 33
3.1 Overview of MIDAS . . . 33
3.1.1 Simplification of impact event . . . 33
3.1.2 Solution procedure in MIDAS . . . 34
3.1.3 Difference between MIDAS-C and MIDAS-M . . . 35
3.2 Structural deflection by out-of-plane loading . . . 36
3.3 Development of MIDAS-C . . . 38
3.3.1 Local indentation behaviour . . . 38
3.3.2 Damage initiation and constitutive behaviour . . . 40
3.3.3 Determination of unloading behaviour and residual dent . . . 45
3.3.4 Summary of MIDAS-C . . . 46
3.4 Development of MIDAS-M . . . 48
3.4.1 Local impact behaviour . . . 48
3.4.2 Transition of plate deflection to indentation . . . 49
3.4.3 Unloading and permanent dent creation . . . 51
3.4.4 Summary of MIDAS-M . . . 51
3.5 Overview of the deductive approach of MIDAS . . . 53

4 Verification 55
4.1 Development of numerical impact problem . . . 55
4.1.1 General model . . . 55
4.1.2 Dimensional and geometry dependent model characteristics . . . 58
4.2 Verification of MIDAS-M . . . 59
4.2.1 Comparison of metal FEM with literature . . . 60
4.2.2 Comparison of MIDAS-M with the metal FEM . . . 62
4.3 Verification of MIDAS-C . . . 66
4.3.1 Definition of composite reference case from literature . . . 66
4.3.2 Comparison of composite FEM and MIDAS-C with literature results . . . 66

5 Validation 69
5.1 Set up of impact experiment: drop-weight test . . . 69
5.2 Data acquisition of impact series . . . 70
5.2.1 Post-processing of recorded impact response . . . 71
5.2.2 Characteristics of impact responses . . . 71
5.2.3 Measurement of permanent indentation . . . 74
5.3 Comparison of experimental results and MIDAS-C . . . 76
5.3.1 Validation of Inductive MIDAS-C . . . 77
5.3.2 Validation of Deductive MIDAS-C . . . 81

6 Application 85
6.1 Interpretation of the residual deformations . . . 85
6.2 Case study set up . . . 86

6.2.1 Definition of appropriate target plates . . . 86
6.2.2 Maintenance data . . . 88
6.3 Application of MIDAS . . . 89
6.3.1 Deductive procedure of MIDAS-M . . . 90
6.3.2 Inductive procedure of MIDAS-C . . . 91
6.3.3 Impact threat comparison . . . 92
6.4 Discussion of the conversion process . . . 93
6.5 The way ahead: from Dents to Dollars . . . 94

7 Conclusion, Discussion and Recommendations 95
7.1 Conclusion . . . 95
7.2 Discussion . . . 97
7.3 Recommendations . . . 98

A Experimental results and post-processing 101
A.1 Post processing of experimentally recorded force response . . . 101
A.2 Determination of characteristics of impact response . . . 103
A.2.1 Determine peak force . . . 104
A.2.2 Determine max displacement . . . 104
A.2.3 Determine residual displacement . . . 104
A.2.4 Determine Delamination Threshold Load (DTL) . . . 105
A.3 Human error in damage width measurements . . . 108
A.4 Experimental impact response results . . . 109

B Additional validation MIDAS-C 111
B.1 Comparison of DTL load drop estimates . . . 111
B.2 Comparison of IFB path estimates . . . 111
B.3 Deductive Solution procedure using plastic radius . . . 113
B.4 Comparison of all impact events with MIDAS . . . 114

C Case study 117
C.1 Design of case study plates . . . 117
C.1.1 In-plane failure requirement . . . 117
C.1.2 Buckling failure requirement . . . 118
C.1.3 Bi-axial compression buckling load . . . 121
C.2 Distributions of damage and impactor characteristics . . . 121

D Development of MIDAS code 123
D.1 Summary of MIDAS core components . . . 123
D.2 Plate object definition . . . 124
D.2.1 Review of Classical Laminated Plate Theory . . . 124
D.2.2 Comparison of plate stiffness approximations . . . 127

E additional Verification 129
E.1 Effect of friction coefficient in FEM . . . 129

Bibliography 131

List of Figures

1.1 Potential ground handling activities causing impact damage 8
1.2 Damage spectrum as function of energy due to blunt impact 9
1.3 Damage categories depending on the design load level and the damage severity . . 10
1.4 Type of damage due to hail as function of increasing impact energy 11
1.5 Example of sub surface damage in a 17ply AS4/8552 CFRP laminate 15
1.6 Simplified forces histories for impact on composite and metal targets 17
1.7 Knee point in permanent indentation as function of impact energy 19
1.8 Geometric representation of a surface damage 20
1.9 Types of impact response as function of impact time 21
1.10 Schematic representation of drop-weight impact experiments 23
1.11 Simplification of impact event by lumped parametric systems 24
1.12 Overview of indentation and corresponding pressure distribution 25

2.1 Overview of effect of impact damage on a metal and composite airframe 29
2.2 Overview of interaction between the inductive and deductive solution procedures . . 31

3.1 Assumed deformation profiles in MIDAS-C and MIDAS-M 36
3.2 Overview of indentation and the assumed pressure distributions 39
3.3 Deformation around the impact location due to delaminations 41
3.4 Approximation of delamination area with n^* of circular delaminations 42
3.5 Comparison of three alternative penetration paths 44
3.6 Flowchart of inductive procedure of MIDAS-C 47
3.7 Definition of loading state of metal plate during quasi-static indentation 49
3.8 The event's plate deflection based on weighted average of limit case solutions . . . 50
3.9 Flowchart of inductive procedure of MIDAS-M 52
3.10 Flowchart of deductive procedure of MIDAS 53

4.1 Schematic FEM model including boundary conditions and meshing partitions 58
4.2 Mesh convergence of metal FEM model 61
4.3 Representation of FE models including boundary regions and mesh size 61

4.4 Comparison of deformation profiles between the FEM and Fagerholt's experimental results . . . 62
4.5 Comparison of load history between the FEM and Fagerholt's experimental results . 62
4.6 Comparison of MIDAS-M with FEM simulations . . . 64
4.7 Verification of deformation profiles 2mm metal plate with an impact radius of 10 mm 65
4.8 Verification of deformation profiles 2mm metal plate with an impact radius of 75 mm 65
4.9 Verification of (metal) deformation profiles for varying plate thickness . . . 65
4.10 Comparison of composite FEM and Lopes' experimental data for an impact energy of 5J . . . 67
4.11 Comparison of composite FEM and Lopes' experimental data for post-DTL impact energies . . . 68

5.1 Overview of drop-weight impact test set-up . . . 70
5.2 Impact response of QI1-1 impacted by spherical steel indentor at 18.3J . . . 71
5.3 Variation of impact response with increasing impact energy . . . 72
5.4 Impact response characteristics of QI, OR and F layups at 27.1J . . . 72
5.5 Damage initiation and peak load of impact series in terms of force displacement . . 73
5.6 Indentation depth measurement approach using dial gauge . . . 74
5.7 Difference between residual indentation and deformation . . . 74
5.8 Measured permanent indentation as function of impact energy . . . 75
5.9 The relaxation of indentation 6 days after impact . . . 75
5.10 The measured dent width (min/max) versus the residual indentation depth . . . 76
5.11 Comparison of MIDAS-C with layup type QI . . . 78
5.12 Comparison of MIDAS-C with layup type F . . . 78
5.13 Comparison of MIDAS-C with layup type OR . . . 78
5.14 Difference in predicted loading slope of different layup types . . . 79
5.15 Comparison of dent estimates with relaxed dent of lay up type QI . . . 80
5.16 Comparison of dent estimates with relaxed dent of lay up type F . . . 80
5.17 Comparison of dent estimates with relaxed dent of lay up type OR . . . 80
5.18 Estimated impact energy given a known impactor radius as function of impact energy 81
5.19 Comparison of estimated impact threat with respect to experimental data . . . 82
5.20 The expected damage dimension as function of both impact energy and impactor size 83

6.1 Residual deformation profiles in MIDAS-C and MIDAS-M . . . 86
6.2 Histograms of measured damage dimensions with distribution fit . . . 89
6.3 Damage contour map of MIDAS-M with maintenance damage . . . 90
6.4 Histograms of measured damage dimensions with distribution fit . . . 91
6.5 Damage contour map of MIDAS-C with predicted threats from MIDAS-M . . . 92
6.6 Impact threat estimates with respect to metal and composite maintenance limits . . 93

A.1 Recorded and post-processed contact force over time of specimen QI2.6 . . . 101
A.2 Extraction of impact response from recorded signal . . . 102
A.3 Comparison of recorded force-time response with Savitzky-Golay filters . . . 103
A.4 Determination of DTL for specimen : OR1-11 . . . 106
A.5 Determination of DTL for specimen : F1-7 . . . 106
A.6 Determination of DTL for specimen : QI1-7 . . . 106
A.7 Variation of measured dent width of a group of 12 students . . . 109

A.8 Variation impact response of layup type F with constant impact energy. 109
A.9 Variation impact response of layup type QI with constant impact energy. 110
A.10 Variation impact response of layup type OR with constant impact energy 110

B.1 Comparison the three penetration path alternatives with respect to layup type F . . 112
B.2 Comparison the three penetration path alternatives with respect to layup type QI . 112
B.3 Comparison the three penetration path alternatives with respect to layup type OR . 113
B.4 Estimated impact energy given a known impactor radius as function of experimental impact energy 114
B.5 Comparison of MIDAS-C with layup type QI 114
B.6 Comparison of MIDAS-C with layup type F 115
B.7 Comparison of MIDAS-C with layup type OR 115

D.1 Flowchart summary of inductive procedure of MIDAS 123
D.2 Flowchart summary of deductive procedure of MIDAS 124
D.3 Flowchart summary of plate object in MATLAB 125
D.4 Bending stiffness approximations as function of plate thickness and square plate size 128
D.5 Bending stiffness approximations as function of plate thickness and square plate size 128
D.6 Bending stiffness approximations as function of aspect ratio for composite lay ups . 128

E.1 Percentage difference of a range friction coefficients w.r.t to $\mu = 0.15$ 130
E.2 Variation of peak force for a range friction coefficients 130

List of Tables

3.1 Definition of bending and membrane stiffness of a circular flat plate 37

4.1 Material properties of AA5083-H116 60
4.2 Material properties of Al2524 63
4.3 Range of wide-body aircraft fuselage dimensions 63
4.4 Impact energies, mass, velocities and drop weight heights. 66
4.5 Material properties of AS4/8552 carbon epoxy of Hexcel 66

5.1 Impact energies, mass, velocities and drop weight heights. 70
5.2 Material properties of AS4/8552 carbon epoxy of Hexcel 70
5.3 The measured indentation as function of impact energy for each layup type 75
5.4 Comparison of the recorded and predicted DTL 79

6.1 Range of wide-body aircraft fuselage dimensions 87
6.2 Material properties of Al2524 87
6.3 Properties of composite material assumed in case study 87
6.4 Failure loads of the composite plate and corresponding required metal plate thickness 88
6.5 Design of target plates used in case study† 88
6.6 Failure loads of target plates used in case study 88
6.7 Statistical distribution of measure of circularity of reported dent damages 89
6.8 Summary of sample data set conversion 91

C.1 Design of target plates used in case study 117
C.2 Failure loads of target plates used in case study 118
C.3 Required plate thickness dependent on the In-plane failure criteria 118
C.4 Required plate thickness dependent on the buckling criteria 119
C.5 Required plate thickness dependent on the In-plane failure criteria 119
C.6 Summary of goodness of fit comparison of distributions using Chi-square test . . . 121

List of Acronyms

AMC	Acceptable Means of Compliance
BVID	Barely Visible Impact Damage
CAI	Compression After Impact
CVID	Clearly Visible Impact Damage
DET	Detailed Inspection
DTL	Damage Threshold Load
DUL	Design Ultimate Load
FEM	Finite Element Model
FOD	Foreign Object Damage
FTE	Failure Threshold Energy
GSE	Ground Service Equipment
GVI	General Visual Inspection
HEWABI	High Energy Wide Area Blunt Impact
ICAO	International Civil Aviation Organization
IFB	Initiation of Fiber Breakage
LPM	Lumped Parametric Model
MIDAS	Model Impact Damage on Aircraft Structures
MIDAS-C	Model Impact Damage on Composite Aircraft Structures
MIDAS-M	Model Impact Damage on Metal Aircraft Structures
MRO	Maintenance, Repair and Overhaul
MSG-3	Maintenance Steering Group 3
NDT	Non Destructive Testing
OAM	Original Aircraft Manufacturer
OEM	Original Equipment Manufacturer
POD	Probability of Detection
QSI	Quasi-Static Indentation
SRM	Structural Repair Manual

VID Visible Impact Damage

List of Symbols

Greek Symbols

α	Indentation of impactor in structure
β	Bending stiffness mismatch coefficient of Morita *et al.*
δ	Indentation
δ_α	Indentation profile
ε	Strain
ν	Poisson ratio
ψ	Slope of cross-section
σ	Stress
θ	ply orientation
χ	Mesh size

Roman Symbols

$\bar{A}$	Area ratio of peanut shaped delamination area and circumscribing circle
a	Fracture length
C_0	Strength coefficient
D	Bending rigidity
E	Energy
F	Force
G_{IIc}	Mode II interlaminar toughness

K	Stiffness
p	Pressure distribution
q	Loading coefficient
R	Radius
t	Plate thickness
U	Kinetic impact energy
w	Deflection
Z_c	Compressive contact strength

Subscripts

0	Permanent/Residual dent depth
b	Bending
bs	Equivalent bending and shear
c	Contact
cr	Critical indentation depth
$d1$	DTL for single center delamination
dn	DTL for n delaminations
$e-0$	Elastic limit
e	Elastic
f	Fraction or penetration limit
i	Impactor
me	Max at end of loading
m	Membrane
n	Number of delaminations
p	Plastic
r	Radially averaged homogenised property
r	Distance to impact center
$r = 0$	Center of plate
rr	Radial
s	Structure
s	Shear
y	Yield

Superscripts

$*$	Fictive effective property
u	Unloading

Introduction

Historically, civil aircraft such as Boeing 777 and Airbus A330, were build primarily using metals. Recently, Boeing 787 and Airbus A350 have been introduced into civil aviation using composite materials for more than 50% of the structural weight. During their service, these aircraft are expected to encounter damage of varying severity. A significant amount of damages is caused by impact related events [2]. The Civil Aviation Authority even goes as far to claim that impact damage accounts for approximately 80% of damage to composite aircraft structures [1]. In comparison, Chen *et al.* [2] show that impact is the cause of approximately 50% of damage, based on maintenance records of B737-800 and B757-200 fleets over a time span of 10 years. As a result, impact damage has a significant economic footprint in the aerospace industry. Besides the direct costs, the industry suffers indirect costs such as delays and flight cancellations. The estimates of the combined annual costs ranges from 1 up to 20 billion US$ for the entire aerospace industry [3–5].

The significance of impact damage has only increased with the introduction of composite materials in aircraft primary structures, as replacement of metals [6]. Impact on metal structures results in a dent or penetrates of the structure's surface [7]. Both are either clearly or reasonably visible by the naked eye. In comparison, impact on composites causes only minor residual indentation, but leads to subsurface damage such as delamination and fiber breakage [8]. These types of damages are generally referred to as Barely Visible Impact Damage (BVID). This reduces the feasibility of visual inspections. In addition, the residual strength is reduced by these subsurface damage types [2, 6, 8–10]. The increased difficulty of damage detection, and the severe strength reductions in case of damage have resulted in conservative certification guidelines: composite structures with BVID should not fail under Design Ultimate Load (DUL). Because the damage in composite is instantaneous, composite design should predominantly adhere to a no-growth approach to maintain a damage tolerant design [2].

Due to the limited experience of the B787 and A350 in operations, a complete understanding of impact damage to be expected over a long operation lifetime is lacking. Clear estimates of maintenance costs are missing [21], but the additional required steps and lack of experience will inevitably increase maintenance cost [22]. Maintenance data of existing fleets provide information of typical impact damages sustained on in-service (metal) aircraft, but provide

limited feedback for the next-generation (composite) aircraft. This study aims at providing additional information to bridge this gap. The goal can therefore be summarized as to predict impact damage on next-generation (composite) aircraft based on maintenance data of in-service (metal) aircraft. This goal is based on the hypothesis that an impact threat can be deduced from a given structural damage, and vice-versa damage on structures can be predicted given an impact threat.

To achieve this goal, an analytical model is developed to Model Impact Damage on Aircraft Structures (MIDAS). This model characterizes impact threats based on damage dimensions in two steps. First, for a given specific threat an impact event is approximated, and the corresponding damage (i.e. permanent dent) is estimated. Second, the analytical model is reverse engineered to deduce the impact threat characteristics from the permanent damage. These two steps are respectively referred to as the inductive and deductive problem (i.e. determine the damage or estimate the impact threat). To the extent of the author's knowledge, methods found in literature solely focus on the inductive problem [11–14], while the deductive problem is not explicitly addressed.

To address the impact specific behaviour of metal and composite materials, chapter 3 describes the development of two variations of MIDAS referred to as MIDAS-M and MIDAS-C. To develop the functionality of MIDAS-M, this work combines elements of modelling methods proposed by Shivakumar *et al.* [15]; Abrate [11]; Simonsen and Lauridsen [13]; and Lee *et al.* [14]. MIDAS-C, on the other hand, continues on the work of Cairns [16] and Olsson and Block [17]. The methods differ from one another in terms of the assumed mode of deformation and the material specific damage creation. Within MIDAS-C, the local indentation is superimposed on the on the global deflection [11, 15], whereas MIDAS-M considers an additional 'transition' region between the local and global deformation modes. The added deformation region allows a more realistic approximation of the larger deflections and the plasticity created in impact events on metal plates. On the other hand, both delamination and initial fiber breakage have a quantifiable effect on the impact behaviour in the composite plates. The applicability of both versions of MIDAS are investigated in chapter 4. A finite element model (FEM) is developed based on reproducing the drop tests conducted by Fagerholt *et al.* [18] and Lopes *et al.* [19]. The FEM comparison verifies the use of MIDAS-M, while it is inconclusive for the composite model. To that extent, chapter 5, presents a validation step of MIDAS-C based on impact experiments.

The feasibility of damage conversion from metal to composite structures is investigated in chapter 6. A case study is developed in collaboration with V.S.V. Dhanisetty and is based on structural damage data provided by a major European carrier. With this feasibility study, a practical use of damage predictions for a Boeing 787 (composite) aircraft fleet based on data of an in-service Boeing 777 (metal) fleet is presented. The appropriate predictions provides a stepping stone for Maintenance, Repair and Overhaul (MRO) to develop successful mitigation of impact risks, which can decrease aircraft down-time and reduce annual maintenance cost. This paves the way to move from a dents-to-dents conversion provided by MIDAS to a dents-to-dollars maintenance practice in airlines.

Chapter 1

Literature review

There is a wide variety of research regarding impact. The focus of this review is providing insight in the general impact phenomena and the relevant modelling techniques applicable to aircraft structures. This literature review focuses on three general topics: (i) the impact threat to aircraft structures, (ii) damage characteristics of impact and (iii) an overview of impact events from both an experimental and a theoretical point of view. Section 1.2 discusses typical impact threats, basic certification and maintenance guidelines. Section 1.3 elaborates on typical damage encountered during an impact event, as well as differences between metal and composite materials. Finally, section 1.4 provides an overview of the understanding of impact events. This encompasses classification of impact events, modelling methods and the effect of several structural elements. Before these topics are addressed, a generic definition of impact is given in section 1.1. This definition highlights some relevant aspects to be considered in this study.

1.1 Definition of impact

In order to provide a relevant overview of the available research of impact, it is important to define an impact event. The Oxford English dictionary defines impact as: *"the action of one object coming forcibly into contact with another"* [23]. With respect to aircraft structures, an impact event is simplified to the interaction of a free moving object (impactor/indentor) having an initial velocity on a target, which is an assumed fixed structure (i.e. aircraft skin). Generally speaking the event considers the following two actors, which are defined by:

Impact Threat an impactor with an initial velocity, mass, shape and material

Target a structure of certain size, material, support structures and boundary conditions

The interaction results in a localized out-of-plane loading of the skin. The impact energy is dissipated by means of deformation and damage creation. This interaction defines the impact

event and results in temporary or permanent deformation of the skin and residual impactor velocity. This deformation behaviour and corresponding damage mechanisms of the skin are the relevant topics within this review. The usage of the term 'damage' varies depending on the type of impact event and material considered. Damage can therefore refer to:

Damage

- visible surface dent with a specific depth and width (metal and composite).
- subsurface damage of the skin, such as matrix cracks, delaminations and fiber breakage (composite).
- subsurface damage of the structure, such as skin-stiffener separation and even more extensive failure of stringers (metal and composite)

The appropriate damage types depend on the type of impact considered, as further explained in subsection 1.2.1. In addition to the resulting damage, literature generally also refers to residual strength estimations after an impact event. This review primarily focuses on the creation of damage. This is typically referred to as the damage resistance or characterization of a structure [17, 24].

1.2 The impact threat to aircraft structures

During their service, aircraft are expected to encounter damage of varying severity. A significant amount of damages is caused by impact related events [2]. Earlier research shows that impact damage account for 50-80% of damage to composite structures [1, 2]. This section elaborates on various elements of this threat to aircraft structures. First, a brief overview is given of the types of impact scenarios and affected structures in subsection 1.2.1. Subsequently, in subsection 1.2.2 several relevant certification guidelines are discussed with a specific focus on the introduction of composites in primary structures. Finally, the effect of impact on maintenance practices is discussed in subsection 1.2.3.

1.2.1 Identification of impact threats

In general, impact damage on aircraft structures can be referred to as Foreign Object Damage (FOD), which is generally defined as: *"a substance, debris, or article alien to a vehicle or system which would potentially cause damag"* [5]. Although a large subset of alien articles can be identified, they can generally be divided in the following: hail, runway debris, bird strikes, tool drops and Ground Service Equipment (GSE) [25, 26]. These events affect different parts of an aircraft and have distinctive different impact behaviour with corresponding damage. The FOD categories are characterized by their impact locations, velocities, and the material properties of both the impactor and aircraft structure. Within the scope of this literature review, these properties need to be identified for each of the FOD categories. In addition, an understanding of these events is required to evaluate appropriate modelling techniques, as described in subsection 1.4.3.

Hail

This category refers to the transverse impact of ice hail on aircraft structures. Firstly, hail impact should be categorized in two subclasses depending on the associated location and velocity of impact: 1) in-flight, and 2) on ground impact [27, 28]. In-flight hail impact occurs on forward facing surfaces (i.e. nose, wing and tail leading edge) with velocities of approximately 200 m/s. While on ground hail damage occurs solely on the horizontal surfaces (i.e top skin, fuselage) at the terminal velocity of hail that can reach up to 30 m/s [28–30]. Inclined impact during ascent or descent approach can as well damage the horizontal surfaces [30]. These impacts are typically referred to as glancing impacts. Kim *et al.* [31] have shown that the normal component actually dominates the impact event, which is relevant for modelling impact events (section 1.4). The forward facing surfaces are typically considered sufficiently damage tolerant for hail damage, due to strict bird strike requirements [30].

Conventional impact analyzes assume that an impactor is rigid, while hail deforms significantly and even disintegrates completely upon impact [31]. This relates to the significantly lower density (810 - 917 kg/m^3); young modulus (1.8 - 2.5 GPa [30] or 10 GPa [31]); and failure strength (10 MPa [30, 31]) of typical hail particles. This behaviour has been analyzed by Kim *et al.* [31] and the following observations should be considered. First, an impact by an aluminum impactor of equal size and energy impact creates significantly more damage than a hail particle. Second, only a small part of the hail particle has disintegrated at the peak force of the impact event. The disintegration of the hail particle indicates that the effective contact area increases during impact compared to a rigid impactor. The resulting increased contact area substantiates the first observation, as a larger impactor with equal energy generally produces less damage [32].

In addition to the impact velocities and material properties, the typical dimensions of hail should be considered. Field *et al.* [30] indicate that the maximum size of hail impactor is more highly correlated with the extent of damage than the number of hailstones impact per surface area. This simplifies the threat analysis of hail impact damage to individual impact events. Although hail varies in size, Neidigk [29] indicates that in most severe conditions the maximum hailstone diameter that on average reaches the ground is approximately 2.6 cm, while there is a 10% probability that it exceeds 5 cm in diameter. On the other hand, there is only 0.1% chance that an aircraft flying through a severe hail storm for approximately 150 kilometres encounters hail of 5 cm in diameter [29]. Hail in an average hailstorm has a maximum diameter of approximately 1 cm [33]. Extreme cases exist of hail size larger than 10 cm, (e.g. as occurred in Dallas 1995), but these are not considered required design standards [31]. A comprehensive overview of hail threat is given by Field *et al.* [30], including a regional meteorological overview and a discussion of the variation in ice properties.

Runway Debris

The threat of runway debris to aircraft has been accepted widely in the airline industry. Airports proactively try to minimize FOD hazards by various FOD management programs, which address inspection, detection, removal, documentation, and creating awareness [3, 5]. Research performed by Insight SRI [34] estimates that around 70,000 incidents occur annually at the world's 300 largest airports, resulting in costs up to 20 million USD for airlines [4, 35].

These incidents result in a wide variety of damage such as torn or punctured tires, dented airframes, turbine or propeller blades, and even engine failure [5]. McCreary [34] indicates that one can typically differentiate between large debris with significant safety concerns and small debris with significant costs concerns. Large debris refers to aircraft parts or large pieces of pavement, which only on rare occasions strike the aircraft. On the other hand, small debris refers to gravel, rivets, bolts, nuts and tire fragments [34]. A study of debris found on airfields by Federal Aviation Administration (FAA) [36] found that metal and rubber tire particles respectively account for approximately 60% and 18% of debris [5].

As part of a threat identification for maintenance practices within the scope of this study, the large debris incidents are exceptional and unrepresentative events, whereas small debris incidents are common and should be accounted for [34]. In addition to metal and rubber particles, gravel of the pavement should be considered [5, 36]. This type of FOD causes damage to the bottom of the fuselage skin and wings at 30° in- and outboard of the landing gear[37]. The following general characteristics limit impact cases should be considered:

Tire Rupture Kim *et al.* [38] indicate that, based on certification guidelines of FAA, a tire rupture event should be considered of tire segments equal to 1% of tire mass at take off speed.

Gravel Nguyen *et al.* [37] identify gravel threats during take-off at speeds ranging from 50–70 m/s with a typical mass of 1–5 gram (largest found 35 gram, but only 1% larger than 10 gram).

Metal No typical guidelines are known for metal runway debris, but similar velocity and masses as gravel should be considered. This refers to a survey of typical small debris found on airfields, referring to typical small nuts and rivets. [5, 34, 36]

Compared to hail impact, runway debris behaves as a non-disintegrating (i.e. rigid) impactor. However, rubber is not a pure rigid impactor, as it undergoes large deformations during impact due to its elastic material properties [38]. This should be considered during the modelling of these impact events. However, Toso and Johnson [39] point out that in experimental set-up runway debris is simulated by means of standardized hemispherical steel impactors. The impact energy and impactor diameter respectively vary between 20-140J and 10-25mm [39]. Although engine damage by debris is a critical aspect, this falls outside the scope of this study.

Bird strikes

Bird strikes are a commonly known impact issue during flight, take off or landing [4, 40, 41]. An important characteristic of bird-strikes is the continuous threat to airports compared to the weather and season dependent threat of hail [34]. The significance of this type of impact is related to the possible severity of damage. All forward facing surfaces can suffer from this type of event, and are required to prove a certain level of impact resistance [40, 41].

Estimates of the annual cost of impact related damage in the worldwide aviation industry vary, but are over 1 billion USD [40, 41]. These costs include both direct material costs, as well as delays and cancellations. McCreary [34] performed extensive research on the cost and frequency of various impact events. Bird strikes occur approximately 2.1 times per 10K

aircraft movements. Although the majority of bird strike events (92%) do not cause damage, the average cost per 10K movements is approximately 45,000 USD. This is a result of the minor (6%) and major (2%) damage incidents accounting respectively for 75,000 USD and 676,000 USD per incident. Similar bird strikes frequencies are reported by Heimbs [40] and Georgiadis *et al.* [41].

The type and cost of damage relate to both the impact location and the actual bird. The windshield has, for example, the highest frequency of impact, but the engine is the most commonly damaged part [34]. However, impact on both the engine and the windshield are not within the scope of this research. The occurrence of bird strikes is typically only recorded and not the bird type or weight, which effectively drives the severity of damage. Relevant limit cases for impact scenarios can be found in certification guidelines.EASA [42] states that leading edge or frontal surfaces should be designed to sustain a 3.64 kg (8 lb) bird at 175 m/s (approximately 55,500 J). The bird weight requirement is reduced to 1.8 kg in FAR-25 [40, 41]. However, heavier bird impacts do exist, such as goose and bald eagles [38]. Approximately 40% of bird strikes occur on the runway at velocities up to 80 m/s.

Similar to hail impact, a bird can not be considered rigid or non-disintegrating [25, 40, 41]. Upon impact, a bird exhibits fluid like behaviour and is referred to as a soft body [40]. Gel substitutes are used in experiments with similar mass density and compressibility to reproduce this behaviour [38, 41]. This increases complexity compared to hail impact further and dedicated numerical models are typically developed compared to analytical techniques [25, 40, 41].

Ground Service Equipment (GSE)

The largest impactor types considered belong to the Ground Service Equipment (GSE) category. The significance of this category is underlined by Kim *et al.* [25], as it accounts for respectively 50% and 60% of major and minor damage of commercial transport aircraft. This type of impact occurs during normal ground operation, which refers to a large variety of operations such as baggage handling, refuelling and passenger loading, as shown in Figure 1.1. The Australian Transport Safety Bureau provided an overview of all ground handling incidents (282) in Australia in the period 1998 to 2008. Within this period, one incident occurred per 50,000 aircraft movements, of which 20% caused damage [43]. In comparison, a higher frequency of once every 5,000 flight is reported by Balk [44], of which approximately 4% resulted in damage. Most of these incidents (80-90%) are caused by external actors compared to movement of the aircraft itself [43–45].

Balk [44] highlights that in several cases damage was found relating to 'unreported events', which is a significant threat to flight safety due to the potential damage. The lack of reporting most likely relates to the fact that the damage is not clearly visible from the surface. In comparison to the other FOD categories, typical damage of GSE is not found in the skin, but at the support structures (e.g frames, stringers and connection elements)[25, 26]. In addition, failure is often found far away from the contact location [6].

Extensive research on this topic has been performed at the University of California San Diego (UCSD) [6, 25, 46–50]. This type of impact event is often referred to as High Energy Wide Area Blunt Impact (HEWABI). As part of their research effort, the approach path and velocity

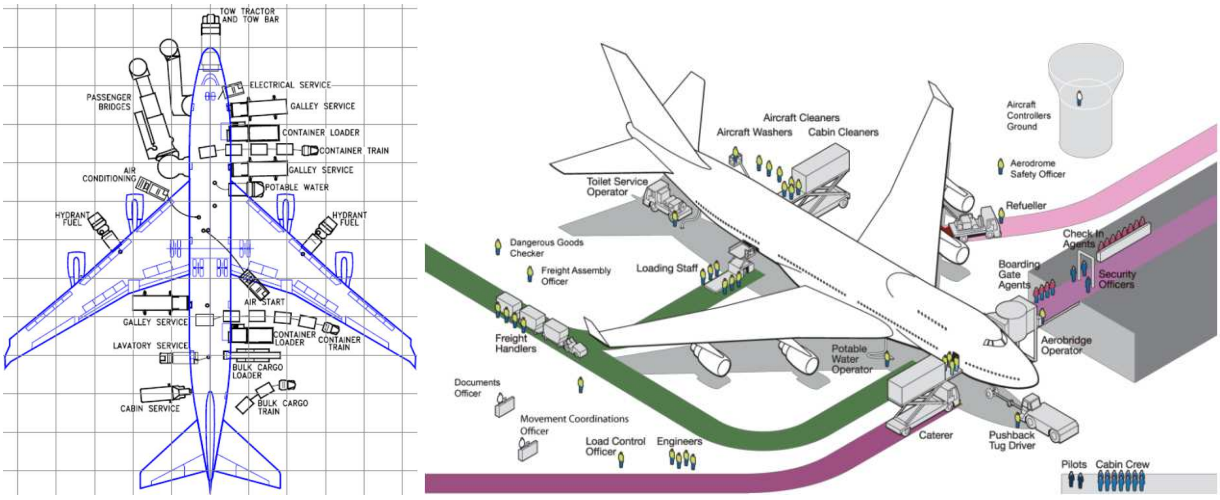

(a) Various types of GSE [44] **(b)** Concurrent ground handling activities [43]

Figure 1.1: Illustration of various sources and locations of GSE impact scenarios

of several ground handling operations has been investigated [46]. This showed that velocities of 0.5–1.0 m/s are realistic within close proximity of the aircraft (i.e 0.1–1.0 m). In addition, GSE vehicles can be considered very heavy mass object ranging from 500 to 10,000 kg. As a result, the impact energy of 1,000 J could be realistic dependent on both mass and velocity. Experiments related to this topic often use rubber bumpers to simulate GSE vehicles. However, cases have been reported of impacts with metal surfaces [26, 51, 52]. As can be seen in Figure 1.1, a typical impacted surface corresponds with the side or partly lower surface of the fuselage. The contact area is typically significantly larger compared to the other FOD categories. It often also extends over multiple reinforcements, such as stringers and frames. As indicated, damage in these substructures is a severe failure mode that should be accounted for.

Tool drops

The final category of FOD causes is tool drops. This category can be considered as a collection group for all maintenance related causes that do not fall under GSE events (i.e. dropped tools, luggage, foot traffic by personnel on non designated areas) [38, 53]. This group can typically be classified as low-velocity and large mass impact. This relates to heights of approximately 1.5 m and masses up to 1kg (or more in case of luggage and foot traffic). Davies and Olsson [12] indicate that it involves velocity in the range of 4-8 m/s and a maximum impact energy of 50 J. Similarly, Kassapoglou [53] refers to impacts by smaller equipment around 5 J (e.g metal rulers and hammers), and some larger equipment of 25J for power equipment (or 60J in extreme cases). Standardized indentation test are often based on this category, which use standardized hemispherical steel indentors of 10-25 mm in diameter [39, 54].

Overview of the effect of the various FOD

The description of the individual impact threats indicates that both the severity of damage and the type of deformation depends on the actual impact threat. A comparison of the difference in terms of impact energy, size and visibility of damage is illustrated by the blunt impact energy-damage spectrum of Kim *et al.* [25], as shown in Figure 1.2. The metal tips in the lower left corner covers both the tool drops and runway debris segments. The bird strikes are excluded in this overview.

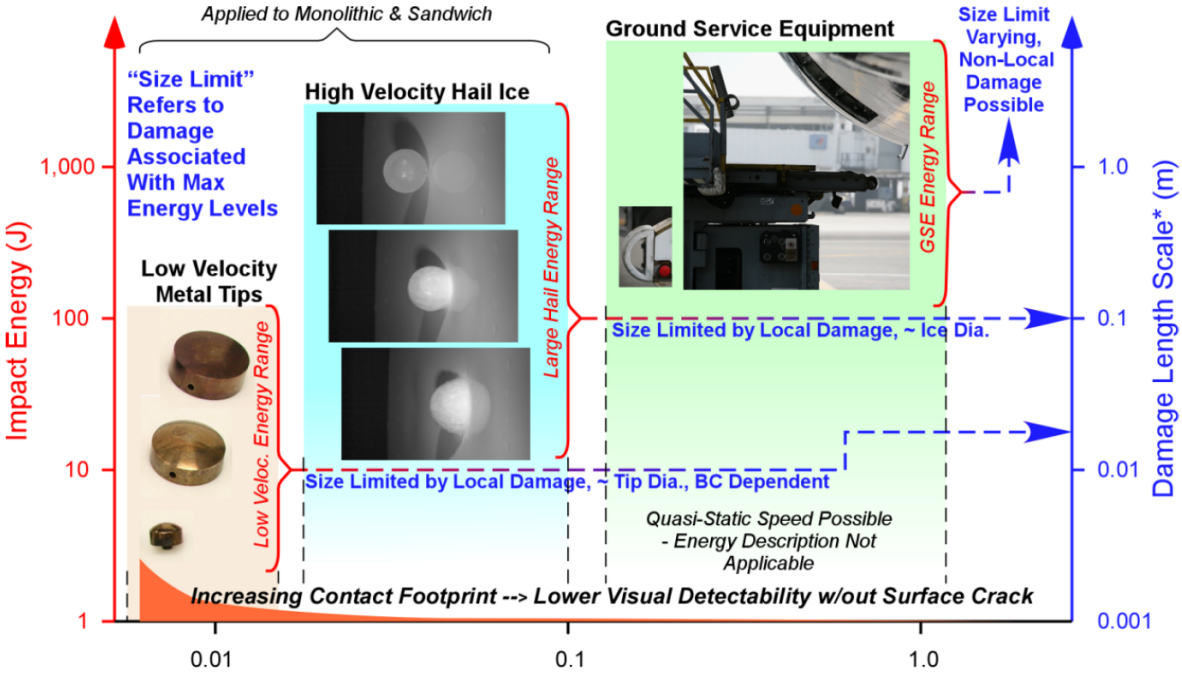

Figure 1.2: Damage spectrum as function of energy due to blunt impact (obtained from Kim *et al.* [25])

1.2.2 Certification aspects of impact

The identification of the types of impacts and corresponding risks described in subsection 1.2.1 indicates 'What' needs to be considered related to impact. Certification and maintenance aspects address 'How' the risks need to be accounted for. A broader simplification of certification can be seen as a set of requirements to ensure safe operating conditions, as described in subsection 1.2.2. Maintenance is the implementation to guarantee these requirements (subsection 1.2.3). Within the scope of this thesis, certification aspects focus on the differences between metal and composite aircraft.

Certification

The scope of certification with respect to impact damage is well summarized by Haase and Mikulik [26]:"*Aircraft certification requires demonstration of the capacity of structures with*

manufacturing flaws and structures damaged during aircraft service to carry loads as described in AMC 20-29". This reflects the key idea of Damage Tolerant designs, which includes the no-growth principle of initial flaws and damage encountered. Even though both reduce the load carrying capacity, the residual strength of the structures should remain above design load levels. Therefore, requirements are defined dependent on the extent and visibility of damage. The Acceptable Means of Compliance (AMC) 20-29 has classified damages in five categories as shown in Figure 1.3 [55].

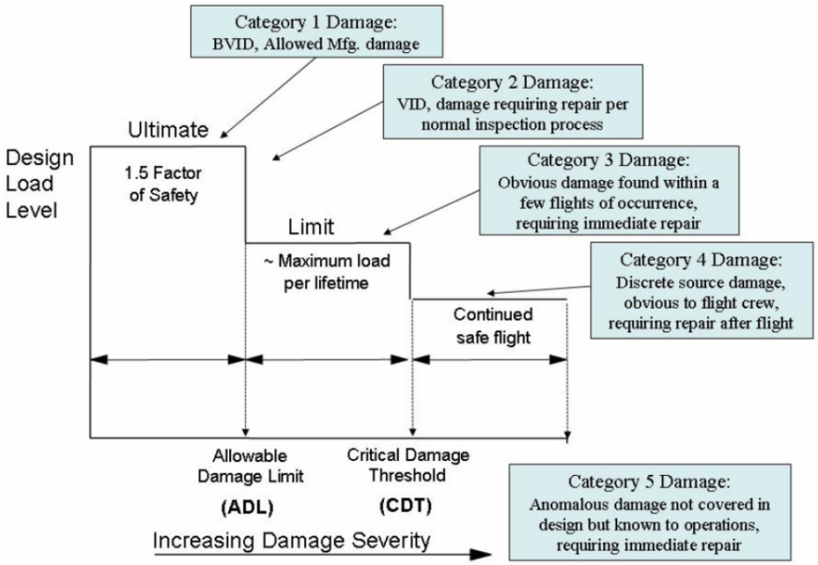

Figure 1.3: Classification of damage depending on the design load level and the damage severity [55]

This categorization can be applied to the previously defined impact threats. The exceptional cases for large debris or bird strikes, which are apparent and noticeable events, fall under the category 4 and 5 [26]. Kim and Kedward [28] provide an illustration (shown in Figure 1.4) of the transition of hail damage between category 1 and 2. While blunt impact of GSE with aircraft fuselage can have varying results [26]. Frontal impact of for example bumpers have a large contact area and damage extends over multiple reinforcements. This is a typical case of category 5 impact. On the other hand, the impact of staircase railing effects a smaller area, and is more likely to result in category 3/4 type of damages. The scope of this research focuses on the first three categories of damage. These refer to damage that rely on the inspection levels of maintenance and their visibility: Barely Visible Impact Damage (BVID), Visible Impact Damage and obvious damage [39, 55].

These categories have become more important with the introduction of composite materials in aircraft primary structures, as replacement of metals[6]. This relates to the poor out-of-plane performance and reduced visibility of damage in composite structures [9, 10]. In addition, the residual strength is significantly reduced in case of damage. This strength reduction and limited visibility are the drivers behind Damage Tolerant design requirements. This limits both the weight and optimization benefits of composites. Davies and Zhang [10] for example indicate that the allowable strain for composite materials is limited up to %0.3 strain, while undamaged structures in pristine conditions could be able to sustain %1.0 of

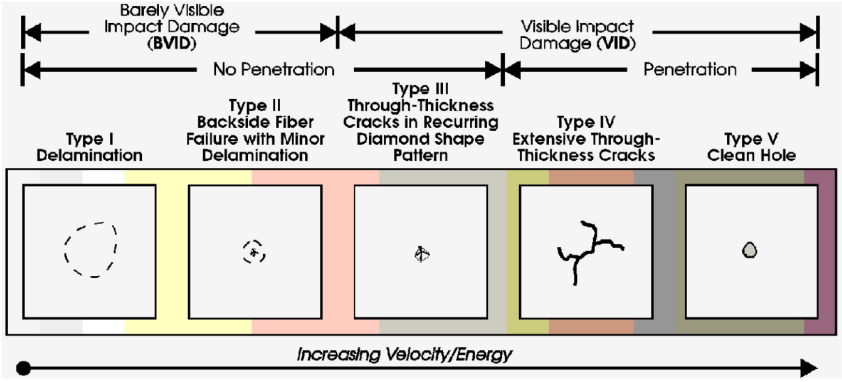

Figure 1.4: Type and visibility of damages due to an hail impact event as function of increasing impact energy [28]

strain. Similarly, Kassapoglou [56] shows that the experimentally determined pristine strength properties should be adjusted for environmental effects (~ 80%), material scatter (~ 80%), and Barely Visible Impact Damage (BVID) (60%) to obtain a design strength. This results in design value of approximately 40% of the originally measured pristine strength. This adjustments still excludes any additional safety factors relevant within the design to account for stress concentrations or Design Ultimate Load (DUL) conditions.

In addition, Haase *et al.* [51] as well as Kim and Kedward [28] expressed concerns related to the focus worst-case scenarios (e.g. threat with highest energy levels) in certification process. Both indicate that BVID caused at originally viewed less critical scenario's could be more detrimental. This is illustrated by the damage sequence for increasing energy in Figure 1.4 (i.e. a delamination could remain undetected compared to a visible penetration).

1.2.3 Maintenance aspects related to impact

Aircraft Maintenance, which is commonly referred to as Maintenance, Repair and Overhaul (MRO), is fully integrated and essential in the entire life cycle of an aircraft [57]. Maintenance includes both scheduled and unscheduled activities. The scheduled activities include routine inspections and overhaul activities to comply with regulations (e.g. the widely known 'lettered' A to D checks [57]). These maintenance schedules are typically conformed to the methodology advised by the Maintenance Steering Group 3 (MSG-3) [2]. Unscheduled maintenance is a result of component failure or impact damage [57]. Within the scope of this research, only the inspection intervals, damage detection methods, and repairs practices are briefly discussed to illustrate operational consequences due to impact damage. The concerns related to damage detection are specifically relevant for the interpretation of results of this study.

Effect of experience with respect to material type

The challenge of scheduled maintenance with respect to inspection intervals lies in finding an optimum between minimizing operating cost, maximizing fleet availability and assuring compliance with certification [2, 58]. Chen *et al.* [2] notes that MSG-3, widely used for defining

inspection intervals, has two shortcomings: its dependency on engineering experience; and the limiting rating ability for composites. Similarly, Cook *et al.* [1] express that future work should not only investigate the detectability of flaws, but also the bias of "metallic" experienced personnel in the interpretation of flaw significance. For example, Haase and Mikulik [26] indicate that personnel can wrongfully interpret an impact incident as minor and therefore assume that no significant damage is generated. This is a result of the limited visibility of (subsurface) damage in composites compared to metals [1, 26].

Although a more elaborate discussion of impact related damage is given in section 1.3, the following is relevant to reiterate in the discussion of detection and inspection limits. While surface damage in the form of dents is an indication of subsurface damage [59], it is not representative of the extent of subsurface damage [60]. Impact damage experiments reported in Cook *et al.* [1] show cases where: 1) the delamination size (subsurface damage) is over 4 times the surface flaw; and 2) approximately equal surface flaws can have significantly different delamination sizes (i.e. a factor 3 difference).

Inspection Intervals

As described above, optimum inspections intervals maximize the fleet availability, minimizing operational costs, and guarantee damage is detected within an appropriate time frame [2, 58]. The required inspection intervals are prescribed by the Original Equipment Manufacturer (OEM)[58], while maximization of fleet availability and minimization of operational costs are achieved by the individual airlines scheduling[21]. The planning of maintenance is constrained by fleet scheduling requirements, availability of resources, and the actual maintenance capabilities by airlines[61]. The maintenance capabilities of airlines refers to the permitted maintenance tasks for Maintenance, Repair and Overhaul (MRO) organizations as defined by by the OEM[62].

Damage detection and inspection limits

Damage detection in composites is a wide and extensive field of research. For a detailed overview and review of inspection methods, the reader is referred to Roach and Rice [62] and Cook [22]. In practice, maintenance facilities of aircraft limit both the available methods and their corresponding detection quality [22, 59]. Cook [22] points out that various Non Destructive Testing (NDT) methods are typically applicable for damage characterization, but not feasible for damage detection on an entire aircraft. In practice 80–90% of inspections are therefore visual inspections [22, 63]. The classification of the five aforementioned categories are likewise all based on the 'visibility' of damage (i.e.Barely Visible Impact Damage (BVID), Visible Impact Damage (VID) and Clearly Visible Impact Damage (CVID) [60]).

However, literature shows that a quantification of these "visibilities" in terms of damage dimensions is not straightforward [22, 29, 63]. Haase *et al.* [51] defines BVID as a dent visible from 1m or having a specific dent depth. Cook [22] points out that this definition or more specifically the dent depth limit differs in industry. The USAF and US Navy, for example, refer to BVID limits of 2.5 mm and 1.25 mm respectively, while Aerospatiale and Boeing define more shallow limits of 0.3 mm and 0.254 mm [22]. In fact, these depth measures are

a result of the reliability of the inspection methods (i.e. measure of certainty that a specific damage size is consistently found). This reliability is commonly presented by Probability of Detection (POD) curves, of which a probability of detection of 90% with a 95% confidence bound is set as reliable detection limit [62, 64].

These POD are highly dependent on various factors. These range from specimen properties (i.e.curvature and paint color) and operational conditions (i.e.surface accessibility and lighting) to human factors (i.e.experience and skill of personnel) [1, 22, 63]. For example, the effect of paint color and surface finish is illustrated by two experimental results from Cook *et al.* [1]. Flaws with dimensions (depth/width) of 0.19/24.5 mm and 0.25/40.45 mm were detected respectively in 100% and 67% of inspections on a gloss grey specimen, contrasted by detection rates of 38% and 0% on a matt blue specimens [1]. A more critical observation of this example is that the larger of the two flaws, in both width and depth, had a consistent lower detection rate.

Damage interpretation

Similar observations with respect to flaw dimensions and the rate of detection have caused several researchers to express their concerns for the use of POD curves [1, 22, 63, 64]. The damage dimensions considered are commonly referred to as the damage morphology. These curves are typically given for a single damage dimension (i.e.dent depth or crack length). This neglects the effect of flaw geometry on the reliability of detection [1]. Currently flaws with equal depth, but significant difference in width, are assumed to be equally likely to be detected. Moreover, these single parameter POD curves give the impression that larger flaws (or in this case deeper dents) are easier to detect. This is, however, not necessarily the case, as demonstrated by the example of Cook *et al.* [1]. The damage morphology and the interpretation of personnel are therefore considered to be important aspects within this study. Cook *et al.* [1] provides some guidelines on a dent geometry definitions. In the work of Chen *et al.* [2], the ratio of diameter/depth is proposed as alternative for POD curves. Within this discussion, the damage width is described as to be perfectly measurable. However, the increased difficulty of detection actually relates to the ambiguous end of a dent (i.e. the dent has a gradual change of slope compared to a discrete discontinuous change of slope). This applies to dents on both metal and composite materials without visible surface cracks.

Although there are no industry-wide defined inspection levels [65], the following three levels are typically present within aircraft maintenance: 1) General Visual Inspection (GVI), 2) Detailed Inspection (DET) and 3) Non Destructive Testing (NDT) [1]. The latter, a non visual inspection method, is essential in determining the appropriate repair requirements [21, 29, 59]. The main difference between GVI and DET lies in the distance to the impact surface (1–2m and 0.3–0.5m respectively) and duration of inspection (seconds compared to minutes per m^2) [33]. For the scope of this research, it can be assumed that the detection limits for dent depths of GVI and DET are respectively 1.0 and 0.3mm [2, 56, 64]. Specific limits of dent widths are typically not reported. However, Chen *et al.* [2] highlights that Structural Repair Manual (SRM) specify the limit of a dent width proportional to the dent dept. For example, in a Boeing 747 damage widths that are larger than 30 times the dent depth are allowed.

Repair of damage

Repair requirements are reported in Structural Repair Manuals (SRM) or defined in collaboration with the Original Aircraft Manufacturer (OAM) [21]. Typically there are four repair levels: 1) cosmetic; 2) temporary; 3) permanent; or 4) part replacement [66]. An appropriate repair strategy is not only dependent on the structural requirements (as given in the SRM), but also on the cost and operational constraints. This trade-off is discussed on an operational maintenance planning level by Dhanisetty *et al.* [21], while Kassapoglou *et al.* [67] presents a cost comparison on a repair design level.

Composite repair techniques are classified in either injection, doubler or scarf-based repairs [59]. Injection based repairs are only applied as a temporary solution to limit damage growth, while both doubler and scarf-based repairs can serve as permanent repair [59]. The applicability of both depends on the repair requirements. A doubler repair is typically easier to perform, but the eccentricity of the patch limits aerodynamic smoothness and causes additional bending stresses [66]. Baker *et al.* [66] provides a comprehensive overview of design guidelines for various composite repairs.

In addition, composite repairs can be adhesively bonded or mechanically fastened. Bonded repair is the preferred method in composite structures, compared to the conventional mechanical fastened repairs in metal structures [68]. This relates to the stress concentrations around the mechanical fasteners [59]. However, bonded repairs still face certification issues in primary structures, due to the inability to detect several types of flaws in the adhesive layer [69]. In fact, Katnam *et al.* [59] provides an extensive overview of scientific challenges for bonded composites repairs, while the hurdles and opportunities in the certification process are clearly described by Baker *et al.* [70].

1.3 Damage

The discussion of impact has centered around the effect of damage and the operational difference between metal and composite damages. The key issue behind this difference is the significant reduction of residual strength in composites, even though the presence of damage is not necessarily apparent. This section elaborates briefly on the differences in material properties and the corresponding damage mechanisms. The types of damages, their interaction leading to a typical sequence of damage and impact resistance of specimens are discussed separately.

1.3.1 Difference of material response causing damage

The limits of maintenance and certification indicate that damage in composites is inherently different compared to metals. Impact on metal structures either causes a dent or penetration of the structure's surface, which are both either clearly or reasonably visible to the naked eye [7]. In comparison, impact on composites, tends to result in minor indentation, but significant subsurface damage [8]. These types of damages are generally referred to as BVID. An example of this can be found in Figure 1.5 [22].

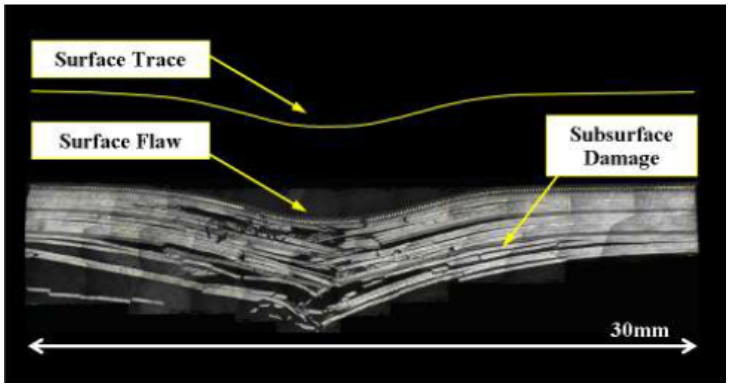

Figure 1.5: Cross section of damage in a 17ply AS4/8552 CFRP laminate impacted by a hemispherical tub of 20 mm with 30 J [22]

A simple distinction between metal and composite is their respective ductile and brittle behavior. The ductility of metals allows significant larger strains of up to 20% compared to 0.5–1.0% for most composites before failure [71]. The allowable strain consists of a large elastic region, which extends in ductile plastic deformation and eventually strain-hardens. Typical failure of metal in impact scenarios results from necking due to membrane effects at large local deformations [72, 73]. This ductility allows the surrounding material to deform accordingly, and thereby dissipate energy during impact. The brittle composites, on the other hand, need to dissipate energy differently by initiation and growth of damage [8, 12]. This behavior is illustrated by the example of damage in Figure 1.5. The minor surface damage is represented by the surface trace, while delamination and fiber breakage extend beyond the apparent dent region. In conclusion, energy is absorbed by visible surface deformation in metals, while in composites energy is dissipated by means of non-visible delamination growth and fiber breakage.

In addition to the limited visibility of composite damages, the delaminations and fiber breakage reduce the residual strength significantly [6, 9, 10, 51]. Sebaey *et al.* [74], for example, shows that the Compression After Impact (CAI) strength reduced by approximately 50%. Similarly, Kassapoglou [56] indicates that design strength properties should account for a strength reduction of 35% due to BVID. As described by Liu *et al.* [75], the determination of CAI strength typically focuses on the in-plane strength properties and prohibits buckling during testing. In comparison, the plastic deformation only has limited effect on the load bearing capacity for metals [8]. Although, the imperfection caused by a dent will facilitate buckling in both metal and composite plates.

Literature generally distinguishes two research areas within the impact damage analysis: damage characterization or resistance, and damage tolerance. These are respectively focused on the determination of the extent of damage, and estimation of residual strength given a certain amount of damage. Although damage tolerance is relevant to the determination of the required maintenance strategy and useful life of aircraft components, the scope of the current research is solely focused on damage characterization. This refers to the creation and determination of damage.

1.3.2 Expected damage types as function of structural properties

The field of damage characterization is focused on the determination of the extent of damage. Within this field, it is of importance to identify which damage types to consider and where to expect them. Within this review, a general distinction is made between surface and subsurface damage. Typical forms of surface damage are indentation and surface cracks. These are often relevant in the field of maintenance as indication of damage, and can in some extent be used as a precursor of subsurface damage. These subsurface damages affect the residual strength of a part. The field of damage characterization is therefore primarily concerned with the detection and estimation of subsurface damage types.

Impact induced damage typically consists of matrix cracks, delaminations and fiber breakage [76]. The location and extent of these failure modes depend on the impacted structure. This relates to the deformation mechanism and structural elements involved during an impact event. As a generalization, it can be assumed that there are three types of impacted structures: thick, thin and reinforced structures.

Thick composite parts, such as landing gear components, are characterized by their limited flexibility. Damage is primarily found close to the impact center [8, 60, 76]. Heida and Müller [60] argue that surface damage is more appropriately described by a pit or hole compared to a surface dent. On the other hand, bending stresses, as a result of the flexibility of thin components, cause damage in the middle and backside of the laminate. This is in addition to the damage on the top surface caused by the contact stresses [8, 60]. Reinforced structures are thin components with reinforcements, such as skin stiffened structures. Besides the failure modes of thin components, specific failure of the reinforcements should be accounted for (e.g. skin-stiffener separation) [6, 26, 46, 51]. Kim *et al.* [6] point out that impact by GSE causes limited damage to the skin, but severe damage to the substructure.

This research is primarily focused on impact to thin and reinforced structures. It should be recognized that the fuselage skin can be classified as both a thin and skin stiffened component. This depends on the type of impact event. For example, hail and runway debris primarily affect the skin (i.e a thin component) [27], whereas the reaction of the substructure is more important in the case of GSE [51, 77]. However, Kim *et al.* [6] indicates that both bird strikes and hailstones can damage internal components.

1.3.3 Sequence of damage during impact event

As described above, impact causes various types of damage in composite aircraft skins. These damages are caused by different stress components, such as bending and contact stresses. These failure modes interact and the impact response changes accordingly during an impact event. Both Abrate [78] and Wagih *et al.* [79] argue that these failures occur in a typical sequence. The impact response of thin composite laminates can therefore be described in sequential steps, in which the impact response changes correspondingly. Wagih *et al.* [79] defines five distinct stages, as shown in Figure 1.6a and described below. The occurrence of these stages in composite plates due to an impact event is confirmed throughout the literature [12, 32, 71, 80, 81].

Before the individual stages are discussed, the generic impact response shown in Figure 1.6a

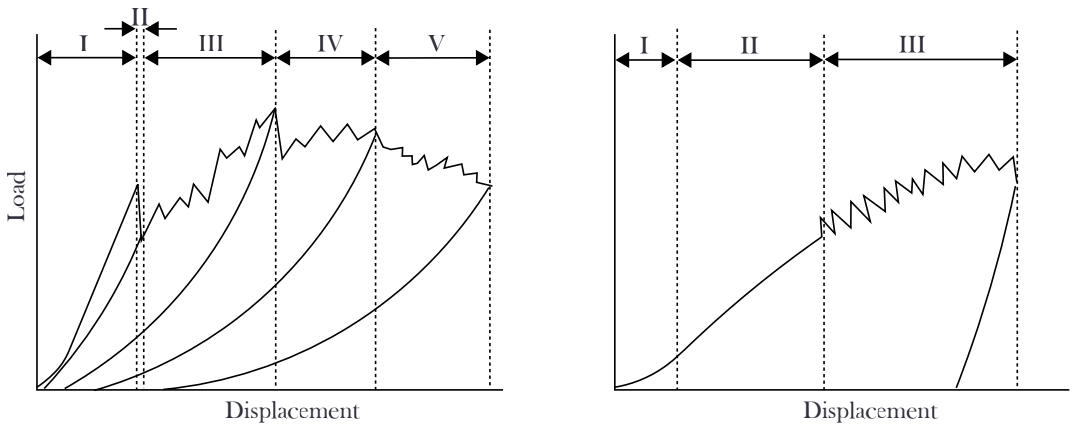

(a) composite target plate [79] **(b)** metal target plate [82]

Figure 1.6: Simplified forces histories due to impact depending on the target material

should be clarified. The response of a structure to an impact event is typically reported by its force-displacement path (i.e the force and corresponding displacement experienced during the impact event). Figure 1.6a is based on the work of Wagih *et al.* [79]. It combines several QSI experiments on plain weave ply composite laminates with increasing indentation depth, which correspond with the five distinct stages and corresponding failure modes. The independent experimental results showed only minor differences in their overlapping regions. After damage initiation larger differences are apparent, but the overall trend remains the same. The response is therefore simplified to a single line, and approximations of the unloading paths are added at the end of each stage.

Stage I: elastic response
In Stage I the load increase follows Hertzian contact laws and typical bending deformation at small displacement. This stage is referred to as the elastic response [79, 83]. No significant damage is present at this stage, although permanent indentation and matrix cracks are present close to the impact surface and center [12, 71, 79]. However, these matrix cracks have limited effect on the resulting laminate stiffness [80, 84, 85].

Stage II: Delamination onset
The second stage can be recognized by the sudden load drop during the indentation. This drop is associated with the onset of delamination and is generally referred to as Damage Threshold Load (DTL) [80]. The onset of delamination is preceded by matrix cracks within the contact area. It is found that delamination in the case of impact initiates either from shear cracks aligning with the interface of plies or due to bending-induced stresses at the interface differently orientated plies [12, 71]. It should be stressed that the load drop results from the instantaneous decrease in laminate stiffness due to the delamination [80]. Olsson [81] states that delamination causes more or less complete loss of the bending and shear stiffness around the delamination center.

Stage III: Delamination growth
Within this stage the load increases again with a lower slope compared to Stage I [79], while the delamination grows linearly with the applied load [71]. The reduced slope is the result of a decrease of stiffness due to the delamination. However, due to the loss of bending and shear stiffness, the membrane effects become apparent [81]. This partly compensates the reduced

stiffness [79]. In addition matrix cracks and fiber splitting are observed in the bottom of the laminate [79].

Stage IV&V: Fiber breakage and penetration
The second large load drop initiates the fourth stage. This load drop is a consequence of fiber breakage in either the top or bottom, which is respectively caused by compressive (and shear) stresses at the surface or bending at the bottom [12, 71, 79]. During the final stage of the impact event, the load decreases and the indentor starts to penetrate the specimen till perforation. This results in significant fiber breakage and delamination [79].

Similar to the results of composites, the impact response of metals can be represented by a generic response. Figure 1.6(b) shows the simplified force history of an aluminum 6061-T6 plate under low-velocity impact loading, based on the work of Suki and M. Jamal-Omidi [82]. It is apparent that no significant load drops occur similar to the composite scenario. However, a decrease in stiffness is visible after stage I. The transition of the II to the III states indicates the initiation of necking, which can be seen as a precursor for plate penetration.

1.3.4 Characterization of impact resistance

The indicated stages of the impact event are relevant insights to model indentation behavior, as described in subsection 3.3.1. In practice, only two stages are used to characterize the impact resistance of a specimen. These refer to the two distinct load drops in the load history (Stage II and IV), which refer respectively to initiation of delamination and fiber breakage. These two drops are commonly referred to as either Failure Threshold Energy (FTE)[8, 31, 32] or Damage Threshold Load (DTL)[10, 80, 86].

The Failure Threshold Energy (FTE)'s are useful indicators of the significance of an impact event in terms of the kinetic energy. However, these FTE's are impact scenario dependent. This refers to a classification distinction made by Olsson [87], as described in subsection 1.4.1. Typically, more energy is required to initiate delamination and fiber breakage for impactors with larger radii, as the impact pressure is distributed over a larger contact area. In addition, the given sequence of damage steps is the most common sequence for low-velocity impact, whereas fiber failure could initiate earlier in high-velocity impacts or in thin specimens. Due to the dependency of FTE on impact conditions, Schoeppner and Abrate [80] argue that a threshold load is more appropriate than a threshold energy. Similarly, Davies and Zhang [10] compares the delamination area as function of the maximum impact force and impact energy for various plate sizes. In this comparison, the maximum force appears correlate with the delamination area, while the relation with impact energy shows a large degree of scatter. Davies and Zhang even go as far to refer to this scatter as being chaotic for an increasing plate thickness. This is a consequence of the increased amount of elastically absorbed energy in flexible thick plates compared to stiffer smaller plates. Moreover, both dynamic and static experiments show approximately the same load drop[80, 84]. Therefore Schoeppner and Abrate [80], Davies and Zhang [10] and Olsson *et al.* [86] argue that Damage Threshold Load (DTL)s are a more relevant damage characteristics.

1.3.5 Surface damage

Both damage characterization and tolerance are based on subsurface damage. The indicated threshold levels (FTE/DTL) are useful benchmarks to predict the extent of damage for a known impact event. From a maintenance perspective, they are of limited to no use to gauge the extent of damage. This relates to the reliance of permanent indentation as an initial measure of impact damage, as described in subsection 1.2.3. Nonetheless, as He *et al.* [88] points out, research related to impact on composites is primarily focused on subsurface damage, whereas only a limited amount of research addresses permanent indentation. Within the scope of this research, permanent indentation is considered to be an important property in the characterization of damage, due to its use in practice. Several aspects to consider are the correlation to the extent of damage, the dent relaxation and the actual measurement of dents.

As described by the sequential damage mechanisms, both threshold levels are indicators of change in contact behavior. The second threshold level, associated with fiber breakage, initiates a significant increase in indentation and correspondingly a residual indentation after impact. This effect on the permanent dent is referred to by He *et al.* [88] as a knee point on the dent dept-impact energy curve. A schematic representation of this behavior is shown in Figure 1.7a. This trend can also be observed in experimental results of Sebaey *et al.* [89], as shown in Figure 1.7b. Similarly, Wagih *et al.* [79] points out that the shape of an indentation profile differs before and after fiber breakage. Initially, a circular profile is an appropriate approximation (given a spherical indentor), while the shape becomes more elliptical at onset of fiber breakage (i.e the major axis is approximately aligned with the damaged fibers).

In addition to the relaxation and observed dent shape, the indentation depth is directly dependent on the quality and consistency of measurements, as described in subsection 1.2.3.

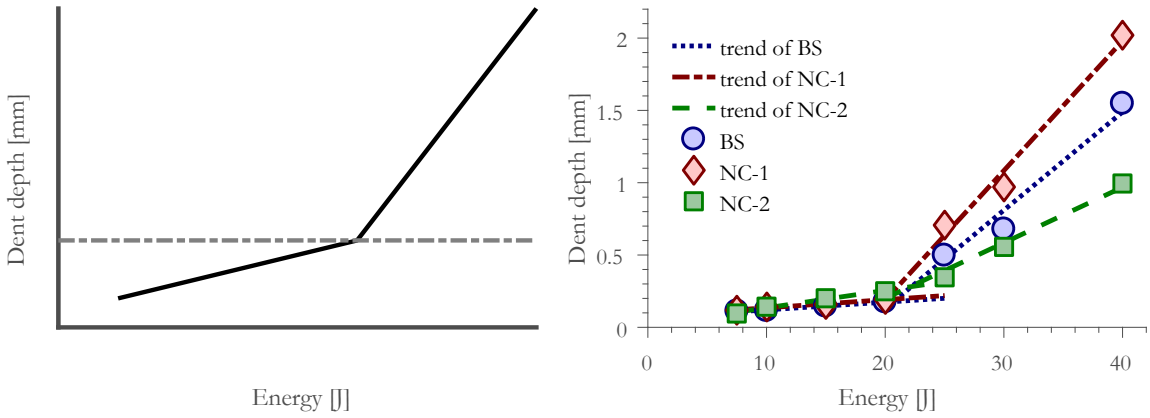

(a) Schematic trends proposed by He *et al.* [88]

(b) Knee point trend superimposed on experimental results of Sebaey *et al.* [89]

Figure 1.7: Knee point in the permanent indentation as function of impact energy [88]

1.3.6 Damage morphology

The interpretation and the detectability of surface damages is dependent on the damage morphology, as indicated in section 1.2.3. Damage morphology is referred to as the combination of the damage shape and size [1, 22, 62]. In practice, the detection of dent is of primary importance in contrast to the accurate measurements of the dent. Within this study, the perceived surface damage is used to estimate the extent of subsurface damage and to deduce the corresponding impact threat. So far, surface damages have been quantified in terms of indentation depth and width. The dent depth, as defined in ASTM D-7136 [54], is the difference between the lowest point and a reference surface. The damage width is, however, not always obvious or apparent, as illustrated by the smooth surface trace in Figure 1.5.

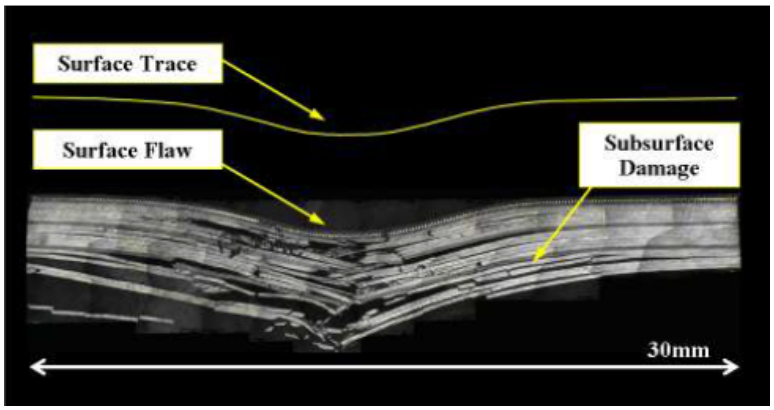

Figure 1.5: Example of sub surface damage in a 17ply AS4/8552 CFRP laminate [22] (repeated from page 15)

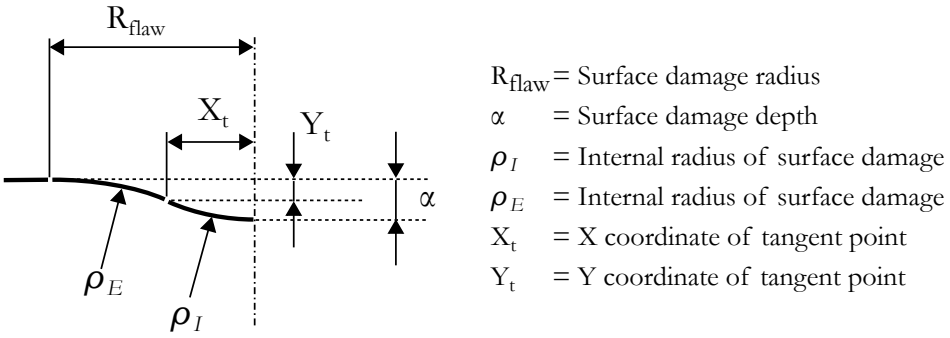

Figure 1.8: Geometric representation of a surface damage (obtained from Cook *et al.* [1])

Cook *et al.* [1] suggest to represent the damage geometry by two curved regions, as shown in Figure 1.8. Note that the additional variables ($\rho_I/\rho_E/X_t/Y_t$) are not particularly useful from a visual inspection perspective. But the perceived and reported width can range from approximately X_t to R_{flaw} depending on the inspectors visual judgment. In other words, the definition of the dent edge remains ambiguous and is based on the interpretation of the inspector. The uncertainty of the perceived damage morphology is considered in chapter 3 and chapter 5 from respectively a theoretical and experimental perspective.

1.4 Modelling of impact event

Both the threat identification and the understanding of impact damage are relevant insights in the understanding of impact events. Impact events have extensively been studied since early 1980 [15, 78]. The threats identified in subsection 1.2.1 indicated a distinctive different behavior. These differences need to be accounted for in various modelling efforts. This section elaborates on the understanding of impact events from a modelling perspective.

1.4.1 Classification of impact regimes

Within literature there is a wide variety in classification of impact events. The classifications intent to distinguish typical impact scenarios based on the loading conditions. They are typically defined by either velocity; experimental techniques; damage formation; or deformation response of the structure [8, 12, 71, 76, 90]. The most commonly used method is based on velocity, which distinguishes low, high and hyper velocity regimes, but a variety of regime limits are used within the literature [8, 71, 78]. Abrate [78] indicates that low velocity impact can be defined up to 100 m/s, while Cantwell and Morton [8] set 10 m/s as an upper limit [71]. This variation results from the dependency of the impact parameters, such as impactor stiffness and mass; plate size and stiffness; and the boundary conditions.

A descriptive difference between low and high velocity impact results in respectively an approximately quasi-static event and boundary independent local impact [71]. Olsson *et al.* [86] argues that this behaviour is dependent on the structural response to stress waves (as is shown in Figure 1.9). Therefore, Olsson [87] states that not only the impact energy or velocity is important but also the impact duration. The impact duration is mainly a result of plate and impactor inertias, which Olsson [87] argues is only dependent on their relative masses. The high/hyper velocity impact regimes correspond to Figure 1.9(a), which is also commonly classified as ballistic impact, while Figure 1.9(b) and (c) correspond to wave and boundary controlled impacts [12].

In the case of the aviation industry, the boundary and wave controlled impact occur by respectively tool drops and runway debris/hail [87, 90]. It should be pointed out that in boundary controlled impact the entire structure deforms, while wave controlled impact only effects part of the structure [90]. Therefore the velocity classification should be interpreted as follows: 1) low velocity regimes typically refer to boundary controlled impact and 2) high velocity

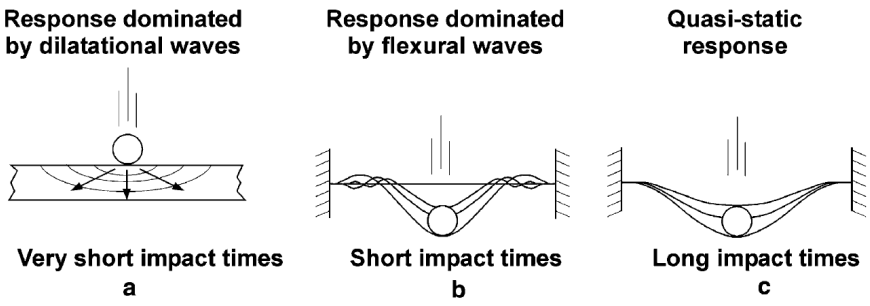

Figure 1.9: Types of impact response as function of impact time [86]

is locally dominating impact with an emphasis on wave controlled impact. This classification includes the fact that low and high velocity impact typically correspond to respectively a large or small mass impactor. Olsson [87] defines a 'mass criterion' for this classification. This classification is relevant for the selection of applicable structural model, as discussed in subsection 1.4.3.

1.4.2 Experimental techniques to perform impact test

As indicated in the previous section, impact events can be subdivided in low and high velocity impact scenarios [71]. Experimental techniques are designed to simulate or approximate the operational conditions of components or materials, and follow a similar classification. The goal of such experiments is to reproduce failure modes and loading behaviour of sub-components [8]. In addition, the low/high velocity impact occur in practice respectively with a large mass (such as tool-drops) or low mass (such as runway debris) [8, 91]. Cantwell and Morton [8] provided an overview of available experimental techniques. The Charpy Pendulum, Izod test and Hopkinson-bar technique are intended for characterization of basic material properties [8, 92]. On the other hand, hydraulic test machines, drop-weight test and gas gun impact testing are used to simulate impact events for respectively Quasi-Static Indentation (QSI), low and high velocity impacts [8]. These three types of tests are most relevant in the scope of the review. For each of these methods ASTM standards can be found, such as ASTM-D6264 [93], ASTM-D7136 [54] and ASTM-D5628 [94].

Quasi-static indentation and drop-weight test are frequently used to determine the damage resistance and the impact response of specimen [54, 93, 94], which is typically expressed as force-displacement path or force history ($F - \delta / F - t$ curves). A force history, as described section 1.3, provides relevant information regarding deformation and damage creation mechanisms. For example, the Damage Threshold Load (DTL) or Initiation of Fiber Breakage (IFB) are typically associated with an apparent load drop. Discontinuities in the force-displacement curves can therefore serve as an indication of the initiation of damage [12].

1.4.3 Structural modelling of impact

As described in subsection 1.2.1, a variety of impact threats are applicable on an aircraft structure. The threats are characterized by several factors, such as the velocity, size and deformation behaviour of the impactor. As such, the response of the structure differs correspondingly. Within literature a variety of modelling methods have been used to model these impact responses. Dependent on the intended type of impact event, researchers have emphasized on different aspects of the structural response [10, 11, 95–97]. These models are generally classified in 1) infinite plates; 2) energy balance 3) spring-mass models; and 4) complete models [11]. However, as both energy balance and infinite plate solutions are considered limit cases of the spring mass models [95], only the complete and spring-mass models are described separately. In addition, the local contact behaviour and some differences between metals and composites are briefly discussed.

Complete models

Complete models attempt to accurately describe the dynamic behaviour and reproduce the complete stress strain state of the system. Based on the applicable assumptions, these approaches use classical plate or (higher order) shear deformation theories [78]. In addition a three dimensional analysis of the stress strain state is reproduced. These methods are computational intensive and are typically tailored to specific geometries and boundary conditions. For example, the proposed efficient approach of Esrail and Kassapoglou [97] requires between 5-10 min to obtain a complete damage state of a 24-ply laminate. Within the scope of this research, such complete models are assumed to be too computational intensive.

Limit cases of the Spring mass models

Both energy balance and infinite plate models are effectively limit cases of spring mass models. Yigit and Christoforou [95] refer to these simplifications as asymptotic solutions of lumped-parameter models. A quasi static approximation of spring mass models reduces the problem to an energy balance [12, 15, 98], which is typically applicable for heavy mass and/or low velocity impacts. On the other hand, infinite plate solutions are independent of the structure's boundary conditions and caused by small masses. These types of events are commonly referred to as (flexural) wave dominated impact events. An additional limit case can be identified, which is the half space solution. The structure is assumed to be sufficiently stiff that no structural response is present during an impact event (i.e. no displacement of the structure, but purely a local indentation).

The aforementioned classification of impacts addresses a similar distinction and the proposed mass criterion by Olsson [87] can be used to select an applicable region. Alternatively, Christoforou and Yigit [99] propose a characterization of impact events based on the relative mobility

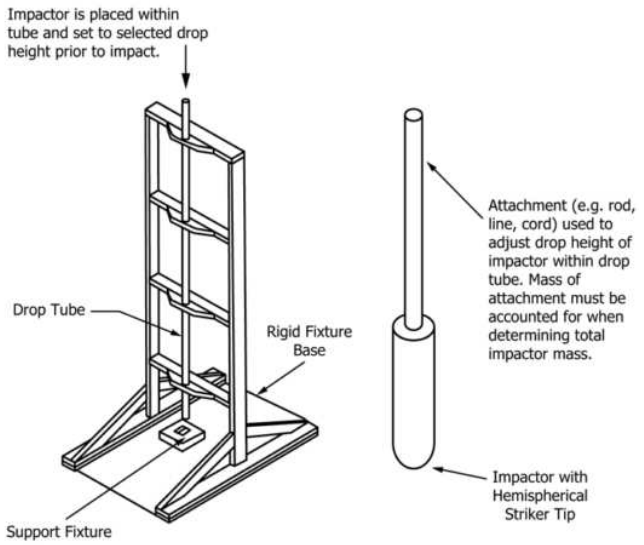

Figure 1.10: Schematic representation of drop-weight impact experiments [54]

and relative stiffness of the structure and impactor. Both parameters are related to, but not uniquely dependent on, their relative mass. This requires additional information of the structure besides the relative mass. However, Yigit and Christoforou [95] indicate that it is impractical to determine these parameters for complex structures.

Spring mass models

Spring-mass models approximate the dynamic behaviour of the system by defining equivalent springs or dampers for characteristic behavioural elements of the structure [78]. Due to the use of both dampers and springs, these models are also referred to as lumped-parameter models [95]. These models characterize an impact event in terms of the variation of force and displacement over time, whereas a complete three dimensional stress strain state is not reproduced [12, 15, 78, 100].

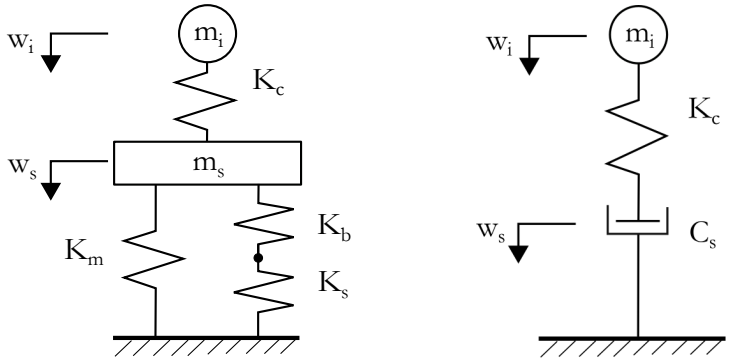

(a) complete boundary dependent **(b)** boundary independent

Figure 1.11: Simplification of structural response of impact in two lumped parameter systems [11, 12, 15, 87, 100]

Within literature variations of spring mass representations of an impact event can be found. The most generic representations are shown in Figure 1.11. These two options, (i) complete boundary dependent and (ii) boundary independent, correspond to the aforementioned classifications. Various stiffness contributions of the structure are accounted for in Figure 1.11a, whereas Figure 1.11b simplifies the boundary independent response by means of a damper. Olsson [87] refers to the damping contribution with the concept of mobility, which is defined as velocity per unit force applied on a component. The mobility of the structure, or typically a plate, is dependent on both the mass per unit area and the plate stiffness. The indicated stiffness contributions are given in terms of an equivalent spring stiffness (K_i are commonly determined by an approximate solution derived from plate theory and Classical Laminate Plate Theory [95, 101]. The literature agrees on the relevance of bending, membrane and shearing effects during an impact event. [11, 12, 79]. However, the relevance of each factor is dependent on the size and deflection of the structure, as well as on the presence of damage. It is generally assumed that both models have a local and a global contribution to the impact response.

Local contact behaviour - indentation laws

Even though the global response determines the dynamic behaviour of the impact, the local contact behaviour has significant effect on the force history and damage creation[11]. A wide variety of local models exists, which are either based on experiments or theory. Theoretical models intended for monolithic laminates are generally modifications of the Hertzian contact law ($F = k\alpha^{3/2}$) [11, 12]. The Hertzian contact law is valid for relatively small indentations, which generally leaves no permanent damage or dent. The modified Hertzian contact laws intend to account for this inelastic behaviour and estimate permanent surface damage. Several methods are available such as Cairns [83] elasto-plastic model, Christoforou *et al.* [102] linearized contact laws, and Tan and Sun [103] statical indentation law. These methods in some sort account for a distributed load between impactor and substrate, see Figure 1.12. For example, standard Hertzian contact assumes a pressure distribution given by

$$p_{(r)} = p_0 \sqrt{1 - \frac{r^2}{R_c^2}}, \tag{1.1}$$

At the same time, the approximation of Cairns [83] is proportional to the surface indentation (i.e dent depth as function of radial distance $\delta_{(r)}$). These assumed pressure distributions are directly related to the resulting stress distribution around the impact center.

The work of Tan and Sun [103] has been especially relevant for determination of a permanent indentation. In repeated experiments Tan and Sun [103] showed that a permanent indentation (α_0) remains after exceeding a critical indentation (α_{cr}), and that it can be approximated by Equation 1.2.

$$\frac{\alpha_0}{\alpha_{me}} = l - \left(\frac{\alpha_{cr}}{\alpha_{me}}\right)^{\frac{1}{q}} \tag{1.2}$$

The permanent estimate is based on the load path during unloading, which is dependent on both the force (F_{me}) and indentation (α_m) at the start of unloading.

$$\frac{F}{F_{me}} = \left(\frac{\alpha - \alpha_0}{\alpha_{me} - \alpha_0}\right)^q \tag{1.3}$$

However, both relations are based on a curve fit of the exponent q with experimental data, which varies from 1.5 - 2.5. Tan and Sun [103] indicate that this variation could be caused by local plastic deformation, material properties and (un)loading rates. The variation of q based on experimental data limits its practical use and does not explicitly account for damage in

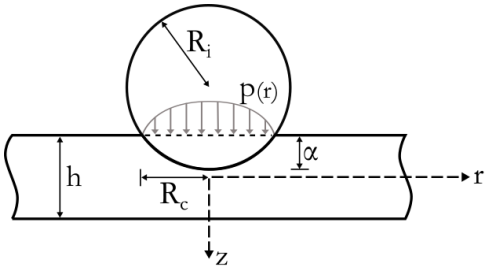

Figure 1.12: Overview of indentation and corresponding pressure distribution

the unloading behaviour. While damage initiation causes a change of stiffness as described in section 1.3. On the other hand, the lower limit of q corresponds with the exponent of the Hertzian contact law. It can therefore be assumed that q depends on the extend of damage and the use of q = 2.5 is a conservative approximation.

Impact behaviour of metal structures

As indicated above, metal behaves differently compared to composites. The ductile behaviour allows larger deformations and includes the surrounding material in an impact event [7, 104]. This contrast illustrates the local behaviour of composites. The modelling techniques proposed for composite contact suggest instantaneous stiffness reductions in both the local and global properties [80, 81]. During impacts on metal structures, damage initiation effectively extends the local impact to a larger area [18]. It should be noted that most common literature of metallic impact refers to the ballistic or necking limit of metals [72, 73]. The modelling methods agree that the critical damage case for metal is defined by perforation and sufficiently large deformations [82]. Modelleling techniques for metal impacts focus on the redistribution of stresses and load due to plasticity compared to instantaneous stiffness reductions in composites. Several material models are considered in literature to account for this redistribution of stresses. These models consider the strain hardening properties of metals, such as power-laws and Johnson-Cook material model [7, 14, 72]. The modelling methods for quasi static indentation and large deformation are most often based on membrane dominating stresses [14, 72].

1.4.4 Finite Element Methods

Literature provides extensive overviews of finite element techniques relevant for impact of metal and composite structures. Finite Element Model (FEM) analysis of metal impact scenarios focus on plasticity of material models. A larger variation in types of FEM results are shown for composite structures. The differences relate to the level of detail to which damage is predicted. Several methods consider stiffness degradation factors defined either by continuum damage mechanics [52] or Hashin Failure criteria [96]. Others use cohesive elements between plies to determine delamination sizes[96].

1.4.5 The influence of component properties on the impact response

Within this review, several distinctive different impact behaviours have been indicated. The discussion aircraft impact threats (subsection 1.2.1), showed that the response of an impact events is dependent on impact locations, velocities, and the material properties. The description of damage types and sequences (section 1.3) indicated that damage is dependent on several structural properties. This section intends to summarize the some important trends in terms of model parameters. This discussion is limited to the effect of impactor, laminate and structural properties. Throughout this review, several differences between composite and metal structures have been highlighted. These differences are not explicitly repeated here.

Impactor properties

The impactor properties have a significant effect on the impact response. Several of these trends have been discussed in subsection 1.2.1, such as the rigidity and size of an impactor. The following list summarizes some of these trends:

Mass Both the mass criterion of Olsson [87] and characterization of Yigit and Christoforou [95] indicated that mass of projectile is a driver of structural response. As a result, the impact has either a boundary or wave controlled response.

Rigidity The rigidity of the impactor determines the extent of deformation of the impactor. The structural models discussed often assume a rigid indentor, whereas results of for example hail and rubber impactors have shown that this is inaccurate. Kim *et al.* [31] showed that the deformation of an hail impactor effectively increases its contact area, and thereby the assumed impactor radius. The effect of increased radius is described by both the size and bluntness effect.

Bluntness The bluntness of an impactor is a measure of both shape and size. The shape of the impactor is a main driver behind the pressure distribution between impactor and structure [49, 50]. Key elements in the pressure distributions are the gradient of pressure. A hemispherical impactor smoothly distributed the pressure, whereas both a flat and sharp-tips results in stress concentrations [31, 105]. A sharp-tip results in high stress concentration at the center of contact, which facilitates penetration and results in failure at lower energy levels [50]. A flat indentor behaves similar to an hemispherical punch, but the pressure is directly distributed over the entire impactor surface. However, the stess concentration at the edges facilitate fiber breakage [105].

Size The effect of impactor size has been discussed by several researchers. A larger impactor distributed the load over a larger contact area, which results in typically lower amount of surface damage [31, 32]. Delamination and fiber breakage in a different extent depend on the size of an impactor. The DTL is independent of impactor size [80, 86], but fiber breakage is facilitated by smaller impactors [32, 50]

Laminate properties

The effect of laminate properties has been extensively discussed by Cantwell and Morton [8] and Lopes *et al.* [19]. Cantwell and Morton [8] includes constituent properties of the fiber and matrix in his evaluation, whereas Lopes *et al.* [19] is interested in the effects of design choices, such as stacking sequence and ply clustering for approximately equal bending rigidity. Within this study, the material properties of fiber and matrix are assumed to be fixed. However, insights in the orientations of plies are considered to be relevant. The following parameters are discussed, assuming that the bending rigidity of the laminate remains approximately constant.

Ply clustering Both González *et al.* [85] and Sebaey *et al.* [106] have shown that ply clustering does not affect the initial response of a laminate to impact. However, propagation of damage is affected by the clustering of plies. Schoeppner and Abrate [80] argues that the number of delamination interfaces is dependent on the ply interfaces with different angles. Similarly, Morita *et al.* [20] argues that delamination is a consequence of bending stiffness mismatch between plies. Clustering of plies leads to increased stiffness mismatch, but fewer interfaces. This combination causes fewer, but larger delaminations than a similar liminate without ply clustering.

Ply angle of set As indicated in the ply clustering discussion, the angle of set between plies is a main driver for delaminations. This behavior is confirmed by various researchers [12, 19, 79, 80, 98]. Olsson [98] estimates that the number of delamination interfaces is dependent on the number of ply interfaces with 90^o and 45^o difference.

Stacking sequence Despite the fact that both aforementioned effects can be considered a subset of the stacking sequence discussion, additional relevant remarks can be made. Improved impact resistance is typically observed for sequences with $+/-45^o$ at the surface [8, 56, 107]. In addition, unidirectional laminates perform poorly, as they are susceptible to fiber splitting. The aforementioned affects of ply orientation is a result of the mismatch of bending stiffness between two plies [8, 56, 80, 107].

Structural properties

The effect of structural properties on damage creation is briefly discussed in section 1.3. In addition, the discussion of structural modelling techniques in subsection 1.4.3 showed several important characteristics.

Flexibility The flexibility of a structure relates to the deformation mechanism and structural elements involved during an impact event [8, 60, 76]. Thin laminates are often considered flexible, and their bending and membrane stiffness influence the progressive damage behavior as a result of delaminations and fiber breakages. In comparison, thick components have limited flexibility and are dominated by contact stresses. In addition, the effects of shear stiffness should be accounted for in deformations of thicker structures [15].

Boundary Conditions This is an alternative view of a similar concept of flexibility. The boundary conditions should be properly accounted for to determine the structure's deformation behavior [15]. In addition, the effect of skin-stiffened structures should be considered (i.e does a stringer act as a simply supported/ clamped boundary, or moveable component) [56].

Curvature Curvature adds stiffness to the structure [108]. In addition, the local contact behavior changes correspondingly. This relates to the assumed pressure distribution of the impactor. A curved surface results in a smaller contact area, and typically a smaller equivalent impactor should be assumed [102].

Chapter 2

Methodology

The literature review has indicated that a significant portion of damage to aircraft structures is caused by impact (i.e. between 50 to 80% [1, 2]). The damage characteristics differs for impacts on composite and metal structures. Impact damage on metal structures is characterized by a dent or penetration of the structure's surface [7], which are both clearly or reasonably visible by the naked eye. In comparison, impact on composites structures results in mainly minor residual indentation, while delaminations and fiber breakage could be present below the surface [8]. Such types of subsurface damages can decrease the residual strength of the structure [2, 6, 8–10]. A summary of the key differences between metal and composite structures is illustrated by the top half of Figure 2.1.

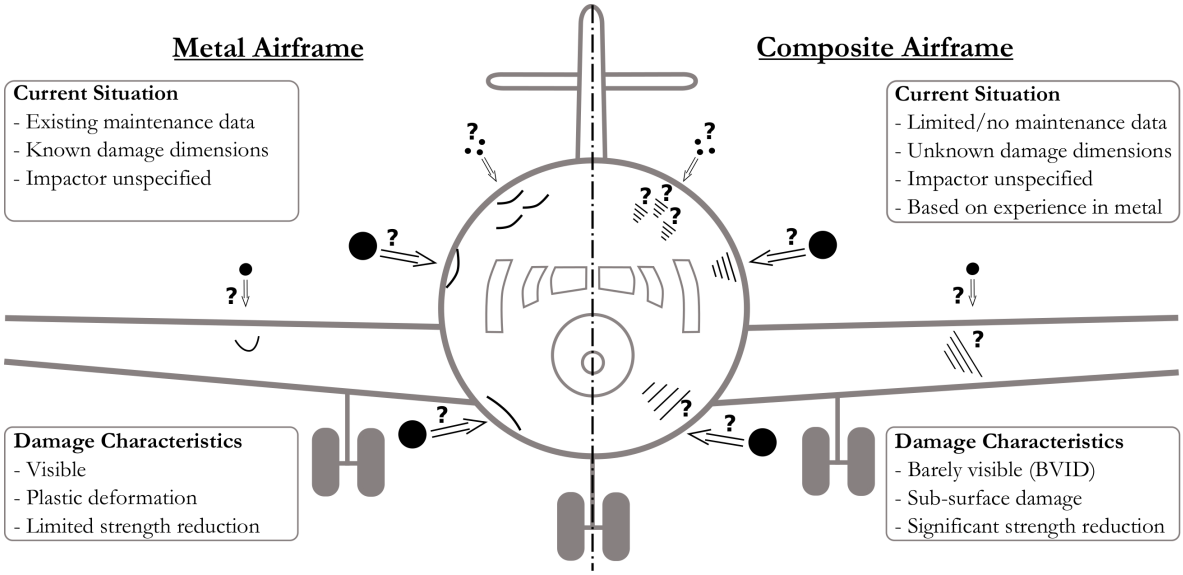

Figure 2.1: Overview of effect of impact damage on a metal and composite airframe

Conservative certification guidelines in composite structures limits the severity of damages that are difficult to detect. Such guidelines account for example for possible reduction in strength by requiring that composite structures with BVID should not fail under DUL. However, Maintenance, Repair and Overhaul (MRO) organizations are still responsible to guarantee that the aircraft is in an airworthy state, which includes detecting difficult Dhanisetty *et al.* [21] highlights that appropriate maintenance planning and decision making is constrained by the lack of appropriate (historical) data and experience, which leads to an inefficient decisions making process. This results in an increase of the required aircraft down-time and an increase in the associated operating costs [61, 109].

Due to the limited experience of the B787 and A350 in operations, a complete understanding of impact damage to be expected over a long operation lifetime is lacking. Maintenance data of existing fleet provides information of typical impact damages sustained on in-service (metal) aircraft, but provides limited feedback for the next-generation (composite) aircraft. This is illustrated by the lower half of Figure 2.1. This study aims at providing the required additional information to bridge this gap. The goal can therefore be summarized as:

To predict impact damage on next-generation (composite) aircraft based on maintenance data of in-service (metal) aircraft

This goal is based on the hypothesis that an impact threat can be deduced from a given structural damage, and vice-versa damage on structures can be predicted given an impact threat. This study evaluates the basis of these hypothesis in order to achieve the defined goal. The research presented in this work, therefore essentially addresses the following two research questions:

(I) *To what extent can impact damage be predicted given a specific impact threat to an aircraft primary structure?*

(II) *To what extent can an impact threat be deduced from a given damage description on an aircraft primary structure?*

These two steps are respectively referred to as the inductive and deductive problem (i.e. (i) determine/induce the damage and (ii) estimate/deduce the impact threat). To the extent of the author's knowledge, methods found in literature solely focus on the inductive problem [11–14], while the deductive problem is not explicitly addressed.

To address the research questions, an analytical model is developed to Model Impact Damage on Aircraft Structures (MIDAS). The first step is to address the inductive problem. The deductive solution is a reverse engineered approach of the inductive step. This allows to deduce the impact threat characteristics from a given permanent damage. The resulting model can serve as a bridge between the known in-service damages on (metal) aircraft and the unknown expected damages on the next-generation (composite) aircraft. This procedure and the key application of this thesis is illustrated in Figure 2.2

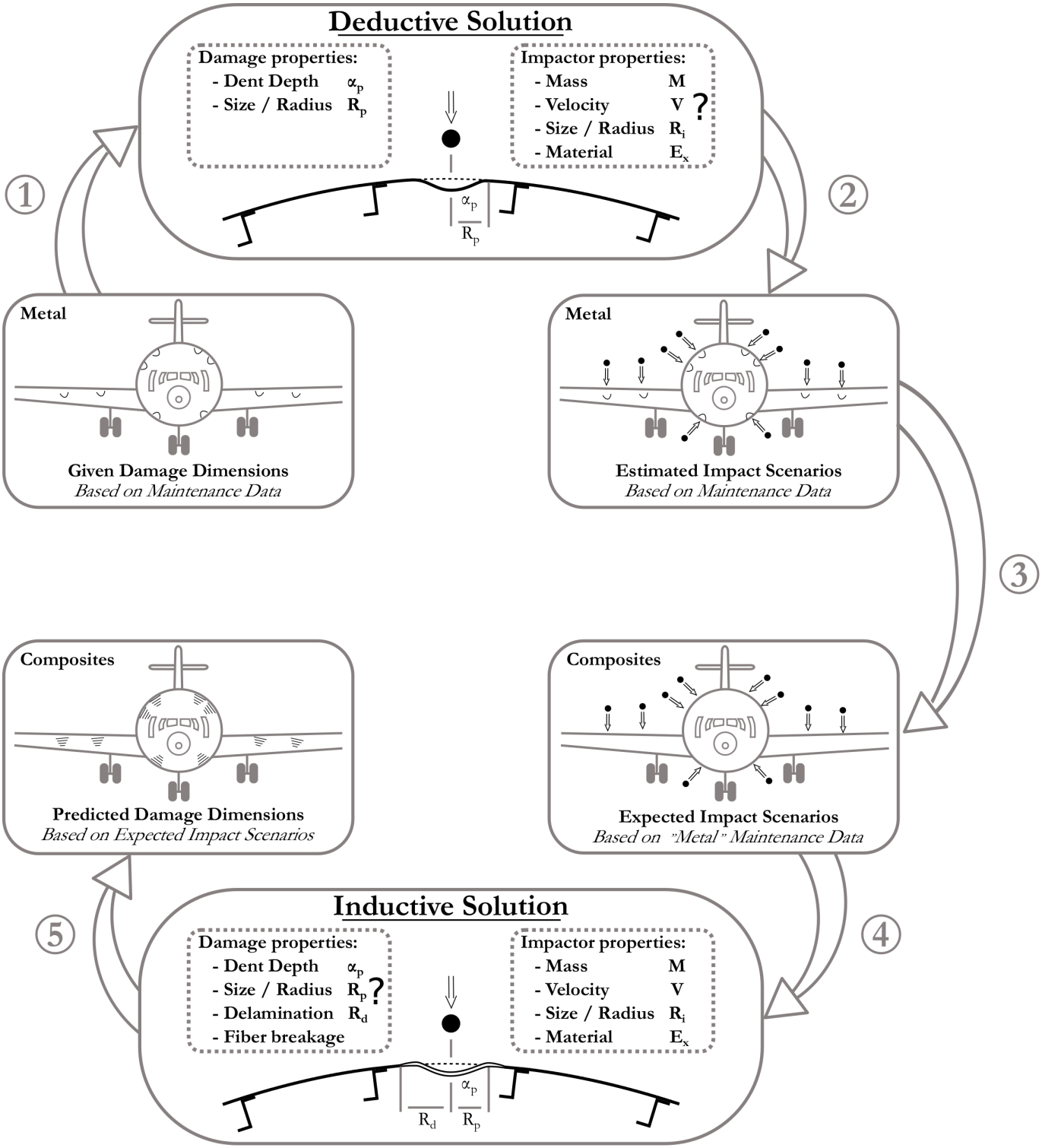

Figure 2.2: Integration of inductive and deductive procedure to predict impact damage on aircraft structures

Chapter 3

Analytical approach of impact

This chapter describes the theoretical approach to Model Impact Damage on Aircraft Structures (MIDAS). Within this chapter, two solution procedures are discussed. The first approach is based on local contact laws and is intended for both composite and metal structures. The second approach is developed as an alternative for metal structures. This relates to the differences in material behaviour, as described in chapter 1. Both approaches are respectively referred to as MIDAS-C and MIDAS-M. An overview of applicable impact scenarios and the generic solution procedure is described in section 3.1.

3.1 Overview of MIDAS

Before the various theoretical contributions are described, this section provides a brief overview of both the impact events and the solution procedure.

3.1.1 Simplification of impact event

This section briefly discusses the general model simplifications. The simplifications address the characteristic components of an impact event (i.e. both the *Target* and *Impact Threat*), and the type of impact event considered. The assumptions related to these components of an impact event are:

A-1 An impact threat is characterized by spherical impactor with a radius (R_i) and impact energy (U)

A-2 The target structure is simplified to flat plate that is either clamped or simply supported.

The literature review highlighted that a wide variety of impact threats are applicable to aircraft structures, but in the context of this thesis these threats are simplified to a spherical impactor

with a radius R_i, impact energy U (**A-1**). In addition, the corresponding material is defined by the Young's modulus and Poisson ratio. The target structure, on the other hand, is an aircraft's fuselage or a wing skin. Both can be considered curved skin-stiffened structures. Within this chapter, the target is simplified to rectangular or flat plate that is either clamped or simply supported (**A-2**). Depending on the impact scenario circular or rectangular plates are more appropriate. Circular boundary conditions are, for example, often used in metal impact experiments[7], while rectangular plates are an appropriate approximation for the stringer and frame pitch in aircraft skin structures.

The assumptions related to type of impact event considered are:

A-3 Impact events are boundary dependent and properly approximated as a quasi static event.

A-4 Impact events occur on the target's center and are perpendicular to its surface.

The effect of mass and impact velocity with respect to the type of impact response is therefore neglected (see subsection 1.4.1). The effect and the validity of these simplifications are investigated and further discussed in chapter 7.

3.1.2 Solution procedure in MIDAS

Even though two separate models are developed MIDAS-C and MIDAS-M, they are both based on a generic solution procedure. This sections briefly outlines this procedure and defines the structural contributions in both models. The key difference between both submodels is highlighted in the next section.

Stepwise solution of impact event

In subsection 1.3.3 two generic impact responses have been described for both metal and composite structures (see Figure 1.6 [p.17]). These descriptions focused on the sequence of damage, and the corresponding change in impact response, but did not address the effect on the residual damage after impact. The residual damage in terms of indentation width (R_p) and depth (α_p) are key parameters within the development of MIDAS. The solution procedure in MIDAS therefore consists of two consecutive phases:

Loading Phase in which the kinetic impact energy is converted in structural deformation and creation of damage.

Unloading Phase in which the residual damage is obtained from the end of loading conditions.

The aforementioned damage stages, described in subsection 1.3.3, need to be accounted for in both the loading and unloading steps.

Structural contributions in impact event

An impact event of a structure is typically characterized by its force, energy, and deformation history. The impact response is dependent on the interaction of two types of deformations: the (local) indentation behaviour, and the (global) structural out of plane deflection. The interaction between the local and global impact response is typically described by a Lumped Parametric Model (LPM), as shown in Figure 1.11a. The lower half of the LPM describes the global structural response, whereas the top refers to the local indentation. Both deformation contributions are effectively superimposed on each other. This results in the energy equilibrium and force equivalence given by Equation 3.1 and 3.2.

$$U = E_m + E_{bs} + E_c \tag{3.1}$$

$$F_c = F_m + F_{bs} \tag{3.2}$$

The terms F and E refer to respectively force and energy, while their subscripts c, m and bs indicate the respective contact, membrane, and combined bending & shear contributions.

The global structural deformation (w_s), indicated by the lower half of the LPM, is applicable to both alternatives of MIDAS, but there are differences between the local indentation behaviour. The global behaviour is therefore described in section 3.2, and the indentation behaviour of respective models in section 3.3 and 3.4. These sections initially describe the pristine deformation characteristics (i.e. without damage), and consecutively cover both the damage initiation and corresponding change in behaviour.

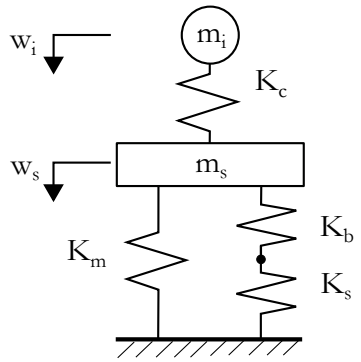

Figure 1.11a: Simplification of structural response of boundary dependent impact in a two lumped parameter system [11, 15] (repeated from page 24)

3.1.3 Difference between MIDAS-C and MIDAS-M

The structural contributions, as indicated by the LPM, are applicable to both models, but the assumed modes of deformation differ. Within the MIDAS-C approach, the local indentation is super imposed on the global deformation and the corresponding indentation follows the shape of the impactor. Within MIDAS-M, on the other hand, an additional "transition" region is added between the local and global deformation modes. The comparison of both modes is illustrated by Figure 3.1. The assumed deformation used in MIDAS-C is conventionally used by for example Shivakumar *et al.* [15] and Abrate [11]. The alternative shape of

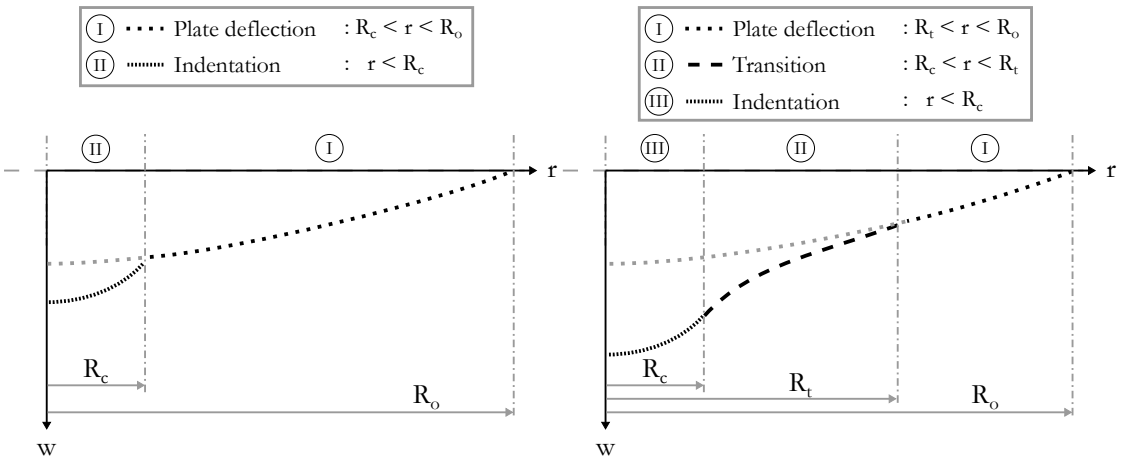

(a) MIDAS-C: the local indentation is superimposed on the global deflection

(b) MIDAS-M: includes a transition region between the local and global deformations

Figure 3.1: Differences in assumed deformation shapes in MIDAS

MIDAS-M originates from penetration limit approximations of Simonsen and Lauridsen [13] and Lee *et al.* [14]. The region outside the contact area (i.e. $r \geq R_c$) appears to dominate the deformation of metal targets upon impact. The difference in assumed shapes is further explained in subsection 3.4.1, as well as in chapter 4 in the verification of MIDAS.

3.2 Structural deflection by out-of-plane loading

The deformation resistance of the structure consists of contact, membrane, and combined shear and bending contributions (indicated by the subscripts c, m and bs). The distinction between m and bs in the lower half of the LPM relates to the bending dominating behaviour at small deflections ($w_s < t$), compared to membrane behaviour at large deflections ($w_s > t$). The shear stiffness is typically neglected for thin plates, which are the primary targets in this research. This relates to the shear stiffness (K_s) being significantly larger than the bending stiffness (K_b). The combined shear bending contribution (bs) therefore simplifies to only a bending contribution (b). The resulting dominating behaviour can be seen in Equation 3.3 and 3.4 describing the force- and energy-deflection of the structure [15, 81].

$$F_b + F_m = K_b w_s + K_m {w_s}^3, \tag{3.3}$$

$$E_b + E_m = \int_0^{w_s} F_b + F_m \, dw_s = \frac{1}{2} K_b {w_s}^2 + \frac{1}{4} K_m {w_s}^4. \tag{3.4}$$

The definitions of the respective stiffness terms are dependent on various structural properties, such as geometry and support structures. Within this research, the target structure is assumed to be a flat rectangular plate, which is either clamped or simply supported on all sides (indicated by subscripts CC and SS). The definitions of K_b and K_m, as given by Shivakumar *et al.* [15] for circular plates, are summarized in Table 3.1. The membrane stiffness terms have been used throughout literature to be applicable for square plates [11, 78, 81, 110].

Alternatively, the bending stiffness of simply supported flat square plates can be obtained from plate deflection solutions based on Navier's solution approach using Equation 3.5 and 3.6 [56, 81].

$$K_{b,SS}^{PT} = \frac{F_c}{w_c} = \frac{F_c}{w_{s,SS\,(x=x_0,y=y_0)}} \qquad \text{where } x_0 = \tfrac{a}{2} \text{ and } y_0 = \tfrac{b}{2} \tag{3.5}$$

$$w_{s,SS\,(x,y)} = \frac{4F_c}{ab} \sum_m \sum_n \frac{\sin\left(\frac{m\pi x_0}{a}\right)\sin\left(\frac{n\pi y_0}{b}\right)\sin\left(\frac{m\pi x}{a}\right)\sin\left(\frac{n\pi y}{a}\right)}{D_{11}\left(\frac{m\pi}{a}\right)^4 + 2\left(D_{12}+2D_{66}\right)\frac{m^2n^2\pi^4}{a^2b^2} + D_{22}\left(\frac{n\pi}{b}\right)^4} \tag{3.6}$$

with a, b, F_c being respectively the plate width, length and applied force. The D_{ij} terms refer to the ABD matrix terms from classical laminate plate theory [56]. A similar expression, using the bending rigidity ($D{=}Et^3[12(1{-}\nu^2)]^{-1}$), can be used for isotropic plates. The circular plate ($K_{b,SS}^{CP}$) and the plate theory ($K_{b,SS}^{PT}$) stiffness approximation, which are defined by respectively Table 3.1 and Equation 3.5, are compared in Appendix D.2.2. This comparison shows differences of 10% and larger. A similar trend is expected for clamped supports. The bending stiffness for clamped square plates ($K_{b,CC}$) is therefore adjusted using Equation 3.7. The global deflection shape of a clamped plate is approximated by Equation 3.8, using the resulting clamped bending stiffness and an assumed trigonometric deflection shape [111].

$$K_{b,CC} = K_{b,CC}^{CP}\left(\frac{K_{b,SS}^{PT}}{K_{b,SS}^{CP}}\right) \tag{3.7}$$

$$w_{s,CC\,(x,y)} = \frac{F\;K_{b,CC}}{4}\left(1-\cos\frac{2\pi x}{a}\right)\left(1-\cos\frac{2\pi y}{b}\right) \tag{3.8}$$

The plate properties and the corresponding out-of-plane loading behaviour is integrated in a plate object defined in MATLAB . The structure of the code and the steps to determine plate properties (e.g. the in-plane stiffness and the ABD matrix) are reported in Appendix D.2.

Table 3.1: Definition of bending and membrane stiffness of a centrally loaded circular flat plate[†][15]

Boundary Conditions (BC)	Bending Stiffness $\left(K_b^{CP}\right)$	Membrane stiffness[‡] $\left(K_m^{CP}\right)$
Clamped (CC)	$\frac{4\pi E_r t^3}{3(1-\nu_r^2)R_0^2}$	$\frac{\pi E_r t}{648R_0^2}$
Simply Supported (SS)	$\frac{4\pi E_r t^3}{3(3+\nu_r)(1-\nu_r)R_0^2}$	$\frac{\pi E_r t}{R_0^2(3+\nu_r)^4}\left[\frac{191}{648}(1+\nu_r)^4 + \frac{41}{27}(1+\nu_r)^3 + \frac{32}{9}(1+\nu_r)^2 + \frac{40}{9}(1+\nu_r) + \frac{8}{3}\right]$

[†] E_r and ν_r are averaged homogenized in-plane properties[81], which are given by:

$$\chi_k^* = \tfrac{1}{2\pi}\int_0^{2\pi}\chi_k(\theta)d\theta \qquad \text{where} \qquad \chi_k^* = G_{rz}^*, E_r^*, \nu_{r\theta}^*$$

[‡] Based on circular plates with radius R_0, but applicable to rectangular plates by using an inscribed circle

3.3 Development of MIDAS-C

Model Impact Damage on Composite Aircraft Structures (MIDAS-C) is developed to determine the impact response of composite structures. The goal is to describe both the force and energy in terms of deformation and corresponding damage behaviour. The method continues on the LPM, the assumed shape and structural deflection as is described in section 3.1.2 and 3.2. In subsection 1.3.3, a typical impact response of composite specimens is described, which highlighted the consequence/effect of various damage types. Effectively, the loading phase of an event consists of three stages:

- **I** Elasto-plastic
- **II** Delamination initiation and growth
- **III** Fiber breakage up to penetration

Similarly, the consecutive unloading phase is affected by each of these stages. Within MIDAS-C, it is assumed that both damaged stages II and III modify the base behaviour in stage I. This section therefore separates these stages during loading, and subsequently elaborates on the unloading phase.

3.3.1 Local indentation behaviour

In addition to the global structural deflection, the structure is locally deformed during impact. The relation between indentation (α) and applied load (F_c) is modelled using contact laws. Contact laws are often seen as a material characteristic, which are time independent and modelled on half plane using a rigid indentor. A wide variety of local models exists, which are either based on experiments or theory [11, 83, 102, 103]. These models are typically modifications of the Hertzian contact law ($F_c = k\alpha^{3/2}$) [11, 12], which is only valid in the elastic region at relatively small indentations. The contact model developed in this study is based on the elasto-plastic contact law of Cairns [83].

An elasto-plastic contact law

Within the Cairns [83] approach, the through-the-thickness constitutive material behaviour is assumed to be elastic-perfectly plastic. As result, a distinction is made between an elastic and elasto-plastic response during indentation. In the elastic region, the material within the contact region acts as a transverse spring, while a constant plastic pressure is assumed in the plastic region. This plastic region refers to a damaged region, which may include matrix plasticity, damaged fibres and matrix cracks, but is for simplicity referred to as plastic. The elastic contact pressure is proportional to the deflection profile as given in Equation 3.9 and 3.10.

$$\delta_{\alpha(r)} = \alpha - R_i \left[1 - \sqrt{1 \left(\frac{r}{R_i} \right)^2} \right] \tag{3.9}$$

$$p_{(r)} = K_e \, \delta_{\alpha(r)} \tag{3.10}$$

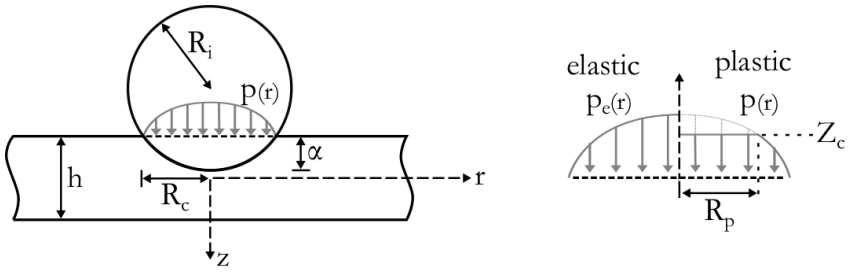

Figure 3.2: Overview of indentation and the assumed pressure distribution in elastic or plastic conditions

in which α, R_i and r refer to the identation depth, impactor radius and distance to impact center as illustrated by Figure 3.2. However, once the indentation is larger then the elastic limit α_{e-0}, the elastic contact pressure distribution exceeds the compressive contact strength Z_c. This results in a plastic region of R_p with a constant plastic pressure equal to Z_c, as shown in Figure 3.2 [83]. The resulting contact force and energy are given as function of indentation depth in Equation 3.11 and 3.12.

$$F_c = \begin{cases} 2\pi K_e \int_0^{R_c} p_{(r)}\, r\, dr, & \text{if } \alpha < \alpha_{e-0} \\ \pi R_p^2 Z_c + 2\pi K_e \int_{R_p}^{R_c} p_{(r)}\, r\, dr, & \text{if } \alpha \geq \alpha_{e-0} \end{cases} \quad \text{with} \quad \alpha_{e-0} = \frac{Z_c}{K_e}, \quad K_e = \frac{E_t^*}{t} \tag{3.11}$$

$$E_c = \int_0^{\alpha} F_c\, d\alpha. \tag{3.12}$$

Assumed material contact properties

The contact behaviour depends on several contact specific material properties, such as compressive contact strength Z_c and the effective transverse modulus of elasticity E_t^* [79, 83]. The definition of both varies in literature depending on type of material. For example, Simonsen and Lauridsen [13] states that the compressive contact strength Z_c of metals is assumed equal to the flow stress ($Z_c = 1/2[\sigma_y + \sigma_u]$), whereas Yigit and Christoforou [112] indicates that twice the shear strength is appropriate for composites ($Z_c = 2S$). The definition of effective transverse modulus E_t^* mainly depends on the relative rigidity of the impactor. The E_z of the target is only considered by Cairns [83], while Abrate [11], Olsson [81], Christoforou *et al.* [102] include the impactor stiffness E_1 and Poisson ratio ν_1 using Equation 3.13. The E_z for composites is assumed to be equal to the E_y of a unidirectional lamina.

$$\frac{1}{E_t^*} = \frac{1-\nu_1^2}{E_1} + \frac{1}{E_z}. \tag{3.13}$$

3.3.2 Damage initiation and constitutive behaviour

This section describes the effect of various damage contributions to the impact response. Damage in composite specimens due to impact consist of matrix cracks, delaminations and fiber breakage, as described in subsection 1.3.3. Both delaminations and fiber breakage are assumed to influence the specimens out-of-plane stiffness [12, 71, 79], while matrix cracks have limited or no effect on the resulting laminate stiffness [80, 84, 85]. Moreover, matrix cracks are difficult to detect without the specific NDT, and therefore not considered within the scope of this work. The initiation of delamination and fiber breakage are respectively considered the first and second characteristic event in an impact response. The initiation of damage (i.e. a failure criterion) and the subsequent loading behaviour (i.e. the progressive damage) of both characteristics is described in the following subsections.

Onset and growth of delamination

As described in subsection 1.3.4, a Delamination Threshold Load (DTL) is typically used to characterize an impact event. The apparent load drop in the force history indicates the initiation of damage, and the resulting change in loading slope indicates the importance of modelling the initiation and progressive loading behaviour of delaminations. The dynamic nature of an impact event results in multiple oscillations (i.e. effectively repetitive load drops). The change in loading slope is therefore equally important to determine the load drop associated with the DTL in a dynamic impact event. Appendix A.2.4 describes a bi-linear regression fit optimization procedure to determine the DTL in force-histories from impact experiments.

Schoeppner and Abrate [80] point out that the initiation of delamination significantly reduces both the local and global bending stiffness, while a membrane stiffening effect is seen upon further loading. Based on these observations, Olsson [113] proposes a modelling approach that modifies the bending contribution of the LPM from Equation 3.3 to 3.14. A delamination typically initiates at a single interface, but subsequently continues on multiple interfaces [81]. The initiation and residual load criteria, respectively F_{d1} and F_{dn}, are therefore based on the DTL of a single and multiple circular center delaminations.

$$F = \begin{cases} K_b w_s + K_m w_s^3, & \text{if} \quad K_b w_s < F_{d1} \\ F_{dn} + K_m w_s^3, & \text{if} \quad K_b w_s \geq F_{d1} \end{cases} \tag{3.14}$$

Davies and Robinson [114] initially developed a DTL based on a fracture mechanics approach for beams with a single center delaminations due to a point load. This criterion is modified by Suemasu and Majima [115]; and Olsson *et al.* [86] to account for multiple circular delaminating interfaces. The strain energy release rate (G) during dynamic fracture due to a concentrated load [114] is given by

$$G = \frac{d\,(U - T)}{dA}, \quad \text{where} \quad \begin{aligned} U &= \tfrac{1}{2} F \Delta w \\ A &= n\pi a^2 \end{aligned} \tag{3.15}$$

in which U and T respectively refer to the strain energy and the kinetic energy of a fracture of area A [86]. The kinetic energy is neglected in the quasi-static approximation (i.e. T = 0). The strain energy effectively refers to the additional work done/deflection (Δw) due to the

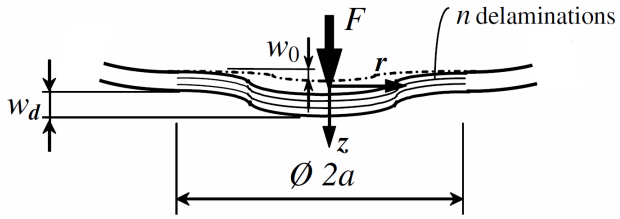

Figure 3.3: Effect of delaminations on the local deformation in a large plate to determine the strain energy release rate (obtained from Olsson *et al.* [86])

change in bending stiffness caused by the delamitation, as is illustrated in Figure 3.3. The additional work is obtained from small deflection theory, assuming that the fractured region can be approximated by a circular clamped plate (i.e the slope and the relative displacement at end of fracture are zero) [86, 115]. The center displacement of clamped circular plate is given by

$$w_0 = \frac{Fa^2}{16\pi D}, \tag{3.16}$$

in which a and D represent the fracture length and plate bending stiffness [116]. The bending stiffness of a laminate with n delaminations (D_n) [86, 115] dependents on the pristine laminate's effective bending stiffness (D^*) [87]. The DTL for single and multiple interfaces in Equation 3.19 follows from Equation 3.15 to 3.18.

$$D_n = \frac{D^*}{(n+1)^2} \tag{3.17}$$

$$D^* \approx \sqrt{\frac{D_{11}D_{22}(\eta+1)}{2}} \qquad \text{with} \quad \eta = \frac{D_{12}+2D_{66}}{\sqrt{D_{11}D_{22}}} \tag{3.18}$$

$$F_{dn} = \pi\sqrt{\frac{32D^*G_{IIc}}{n+2}} \qquad \text{with} \quad F_{d1} = F_{dn\,(n=1)} \tag{3.19}$$

As a delamination typically initiates at a single interface [81], the estimate of F_{d1} and the modified LPM relation can be used to predict the DTL of an impact event. The residual bending load depends on the number of delaminating interfaces. The modified fracture mechanics approach of Davies and Robinson [114] is based on equivalent circular delaminations, while actual delaminations are typically peanut shaped [78, 117]. However, as highlighted by Sebaey and Mahdi [118], the projection of the multiple peanut shaped delaminations of varying orientation appear elliptical (or circular for quasi-isotropic laminates). Olsson [81] therefore proposes an estimate of n^* equivalent circular delaminations circumscribing the actual delaminations, given in Equation 3.20 and illustrated by Figure 3.4.

$$n^* = \bar{A}\left[\bar{A}_{45^o}\, n_{\Delta 45^o} + n_{\Delta 90^o}\right] \tag{3.20}$$

The estimate for n^* is based on the work of Levin [119] and Liu [120] and depends on the number of interfaces ($n_{\Delta\theta}$) with a specific ply mismatch angle (i.e. $\Delta\theta = 45^o$ or$\Delta\theta = 90^o$). Levin [119] demonstrates using fractography that the ratio of peanut shape between a $0^o/90^o$ layer and circumscribing circle is approximately 0.30 ($\bar{A} \approx 0.30$). While Liu [120] continues that such an area ratio is proportional to ply mismatch angle. This is a consequence of the

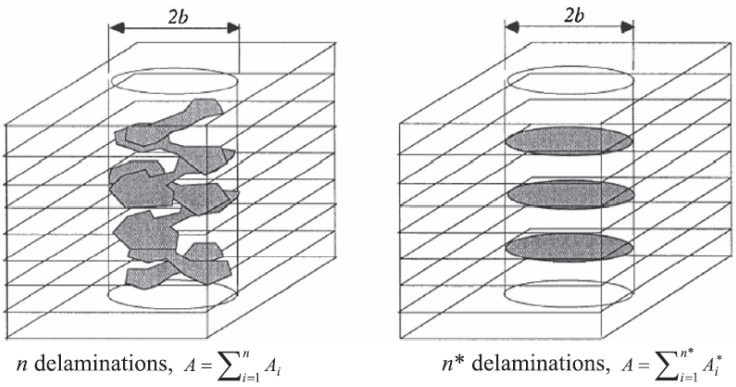

Figure 3.4: Simplification of actual number of delaminations n to an effective number n^* of circular delaminations (from Olsson [81])

bending stiffness mismatch between plies, which is quantified by Liu [120] in terms of a bending mismatch coefficient given in Equation 3.21.

$$\bar{A}_{|\theta_t - \theta_b|} = \frac{|D_{11(\theta_t)} - D_{11(\theta_b)}|}{D_{11(0^o)} - D_{11(90^o)}} \tag{3.21}$$

The $D_{11(\theta)}$ terms refer to the isolated laminae's D matrix terms orientated in the laminate's longitudinal axis[1]. Even though this coefficient provides a simple estimate for the effect of ply mismatch angles, it is not sufficient to predict delamination damage in multi-ply specimens [20, 121]. The coefficient, based on experimental results of $[0_4/\theta_4]$ laminates, considers angle differences with respect to longitudinal axis, but does not capture the mismatch between interfaces of for example $[-45^o/45^o]$. Similarly, as highlighted by Morita *et al.* [20], the effect of bending stiffness due to the offset from the neutral axis is not captured.

Both Fuoss *et al.* [121] and Morita *et al.* [20] propose alternative bending mismatch coefficients. However, these are dimensionalised, and can therefore not be used as a scaling factor in Equation 3.20. Morita's coefficient β, given in Equation 3.22, is therefore non-dimensionalised using Liu's concept of a maximum reference[120]. The coefficient β is dependent on the interfaces distance to the laminates top surface z_i, the in-plane stiffness mismatch[2] $\Delta Q_{11\,(\theta)}$ and the entire laminates bending stiffness D_{11}. Moreover, β is not only dependent on the laminate's longitudinal axis, but follows from the radial average over each interface.

$$\beta_i = \frac{1}{2\pi} \int_0^{2\pi} \frac{\Delta Q_{11(\theta)} z_i}{D_{11(\theta)}} d\theta \tag{3.22}$$

The reference $\beta_{i,max}$ uses the the largest in-plane difference (i.e $\Delta\theta = 90^o$). This modifies the n^* estimate given in Equation 3.20 to that from Equation 3.24, in which the combination of Liu's scaling factors and the number of interfaces is replaced by the summation of the

[1]The isolated $D_{11(\theta)}$ terms are given by $D_{11(\theta)} = \frac{1}{3} t_{ply}^3 \left[Q_{11} \cos^4\theta + 2\,(Q_{12} + 2Q_{66}) \cos^2\theta \sin^2\theta + Q_{22} \sin^4\theta \right]$, which is independent of the remaining laminae [120]. This effectively simplifies the coefficient to the difference of laminae's in-plane directional stiffness instead of bending stiffness.

[2]the 11 direction is aligned with global coordinate system (i.e. in the direction of a 0^o ply). The radial average rotates $\Delta Q_{11\,(\theta)}$ from 0 to 2π, and thereby comparing the mismatch between two plies in all directions.

individual interface β_i's (i.e. $\sum_{\Delta\theta} \bar{A}_\theta n_{\Delta\theta} = \sum_{i=1}^{n} \frac{\beta_i}{\beta_{max}}$).

$$\beta_{i,max} = \frac{1}{2\pi} \int_0^{2\pi} \frac{|Q_{11(0^o+\theta)} - Q_{11(90^o+\theta)}| z_i}{D_{11(\theta)}} d\theta \tag{3.23}$$

$$n^* = \bar{A} \sum_{i=1}^{n} \frac{\beta_i}{\beta_{i,max}} \tag{3.24}$$

The modified LPM relation given in Equation 3.14 accounts for the global structural response upon delamination. Similarly, as indicated by Schoeppner and Abrate [80], the local indentation stiffness decreases. This decrease is not explicitly addressed in literature, but by enforcing the force equivalence (Equation 3.2) and a continuous increase of indentation. The contact force due to indentation is scaled proportional to the load drop following the DTL.

$$F_c = \begin{cases} F_c^{ep} & : \text{Equation 3.11} \quad \text{if} \quad K_b w < F_{d1} \\ F_c^{DTL} & : \text{Equation 3.26} \quad \text{if} \quad K_b w \geq F_{d1} \end{cases} \tag{3.25}$$

$$F_c^{DTL} = f_{DTL} F_c^{ep} \qquad \text{with} \quad f_{DTL} = \frac{F_{dn} + K_m w_{DTL}^3}{F_{d1} + K_m w_{DTL}^3} \tag{3.26}$$

Fiber breakage

Fiber breakage is typically the second characteristic event in an impact response. It is effectively a precursor of plate penetration, which is associated with the reduction of load carrying capacity and the significant increase of indentation (as indicated by the knee-point of He *et al.* [88]). Determination of the residual indentation therefore requires accounting for both the initiation of fiber breakage as well as the corresponding progressive loading behaviour.

In comparison to the bending associated DTL criterion, the Initiation of Fiber Breakage (IFB) is purely focused on the membrane loading contribution. This is based on the typical sequence of failure that IFB follows after DTL [76, 79]. Olsson and Block [17] proposes a IFB criterion in which the plate is assumed to wrap around the impactor, due to the loss of bending stiffness after delamination. This results in a pure membrane stress state around the contact edge (i.e. no bending stresses, but uniform tension). Vertical equilibrium at the edge is given by Equation 3.27, in which the uniform membrane stress σ_0 is dependent on the membrane strains ε_0, the radially averaged Young's modulus E_r and Poisson's ratio ν_r. The relation between membrane strains and deformation angle is given by the Almansi strain tensor ($\varepsilon_0 = \frac{1}{2}\sin^2\psi$), as described in subsection 3.4.1. The vertical equilibrium (3.27a) simplifies to the membrane failure criterion (3.27c) [17].

$$F_{IFB} = 2\pi t\, R_c\, \sigma_0 \sin\psi_c \tag{3.27a}$$

$$= 2\pi t\, R_i \sin\psi_c\, \varepsilon_0 \frac{E_r}{1-\nu_r} \sin\psi_c \tag{3.27b}$$

$$= 4\pi t\, R_i\, \varepsilon_0^2 \frac{E_r}{1-\nu_r} \tag{3.27c}$$

In contrast to the progressive damage behaviour after delamination, literature typically does not address the change in behaviour after IFB in terms of modelling methods. However, several important observations related to this change in behaviour can be gathered from literature:

(A) Olsson [81] indicates that any fiber rupture leads to rapid growth of fiber damage, loss of membrane stiffness and eventually penetration.

(B) Abrate [76] and Wagih *et al.* [79] state that the contact force decreases, while impactor displacement increases.

(C) He *et al.* [88] highlight that IFB results in a significant increase of permanent indentation as function of impact energy.

In correspondence with observation (A), the axi-symmetrical uniform tension stress assumption in the failure criterion effectively implies that all plies should fail simultaneously and instantaneously. This is a conservative approximation[3], and can be used to predict damage in the Inductive Problem. However, a significant portion of the solution space in Deductive Problem is excluded (i.e. impact energies exceeding E_{IFB}). Observations (B) and (C) indicate that there is a progressive failure trend, and an applicable lower bound estimate needs to be developed. Three alternative lower bound estimations are proposed by converting the indicated observations into assumptions. Two alternatives are based on the hypothesis that localized failure of (A) implies a pure local penetration without any additional deflection. The third alternative, on the other hand, allows additional deflection, but assumes fiber failure leads to loss of the residual bending load (F_{dn}). The three alternatives are illustrated in Figure 3.5. Based on the localized failure, it is assumed that impact only continues locally.

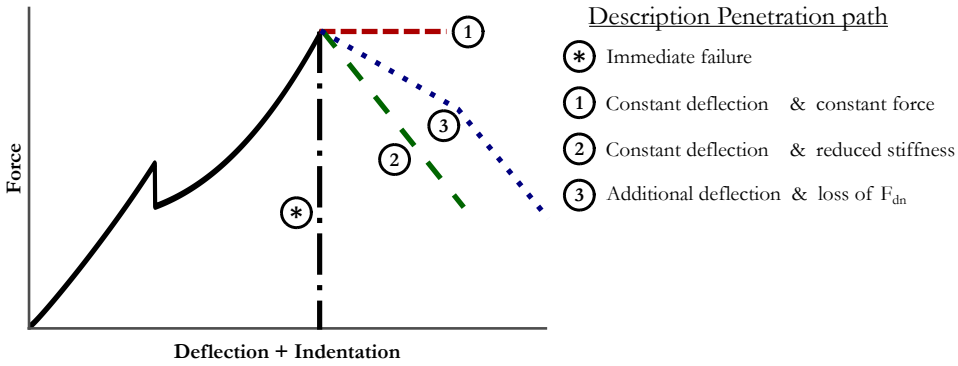

Figure 3.5: Illustration of the three alternative penetration paths

This implies that global deflection is kept constant, while only the indentation increases. As indicated by observation (B), the reduced load carrying capacity needs to be quantified. This is based on the progressive loading behaviour after delamination, in which the bending portion of the global plate deflection relation was modified (i.e $K_b w = F_{dn}$). In this case, the membrane portion is dependent on the fibers. As an initial lower bound estimate, the load is kept constant to F_{IFB}, and the maximum indentation of an impact event is determined by

$$\begin{aligned} U &= E_{IFB} + F_{IFB}(\alpha_{me} - \alpha_{IFB}) \\ \alpha_{me} &= \frac{U - E_{IFB}}{F_{IFB}} + \alpha_{IFB}. \end{aligned} \tag{3.28}$$

[3]The definition of 'conservative' is ambiguous with respect to the Inductive and Deductive Problem. A conservative approximation in the Inductive solution is implicitly an un-conservative in the Deductive solution. (i.e. an overestimation of permanent dent implies an underestimation of impact energy/threat)

As a second alternative, the load carrying capacity is reduced by introducing an effective membrane stiffness. This changes the global plate deflection relation to Equation 3.29, in which the effective membrane stiffness K_m^* varies with indentation.

$$F = F_{dn} + K_m^* w_{IFB}^3, \tag{3.29}$$

The undamaged definition of K_m, which is given in Table 3.1, depends on the thickness, radially averaged Young's modulus E_r and Poisson's ratio ν_r. These properties depend on the laminae material properties and given layup sequence of the target. Based on the hypothesis that K_m^* varies with indentation, it is assumed that a number of top plies (n_t) becomes ineffective during the final loading stage of impact. The K_m^* is determined using the definition of K_m, but excluding the ineffective top plies. The number of ineffective plies is obtained from

$$n_t = \frac{\alpha}{t_{ply}}. \tag{3.30}$$

The resulting maximum indentation follows from the required energy equivalence similar to Equation 3.28, and is given by

$$U = E_{IFB} + \int_{\alpha_{IFB}}^{\alpha_{me}} F da \tag{3.31}$$

Both proposed alternatives lead to rapid penetration, due to the assumption of pure localized failure. The third alternative therefore allows additional structural deflection during the penetration. This approach continues on the reduced effective membrane stiffness, but assumes that fiber failure leads to loss of the residual bending load (F_{dn}). The IFB criterion given by Equation 3.27 is based on the fact that all plies remain effective. However, similar to both the F_{dn} approximation using multiple delaminating interfaces and the reduction of effective membrane stiffness due to ineffective plies, the IFB criterion can be applied to a reduced number of effective plies ($F_{IFB,nt}$). The penetration path consists of a gradual loss of the residual bending load (F_{dn}) till the residual force can be carried by the remaining effective plies. This requires the determination of minimum number of ineffective plies n_t for which the inequality 3.32 holds. The corresponding maximum plate deflection ($w_{IFB,nt}$) is given by Equation 3.33.

$$F_{IFB,nt} < F_{IFB} - F_{dn} \tag{3.32}$$

$$w_{IFB,nt} = \sqrt[3]{\frac{F_{IFB} - F_{dn}}{K^*_{m(n_t)}}} \tag{3.33}$$

In this third alternative, some additional structural deflection is allowed till $w_{IFB,nt}$, after which rapid penetration occurs similar to the second alternative. The relation of force, displacement and indentation is assumed linear between F_{IFB} and $F_{IFB,nt}$. The three alternatives are compared in Appendix B.2 with respect to the experimental data reported in Chapter 5. The third approach is deemed most appropriate based on that comparison.

3.3.3 Determination of unloading behaviour and residual dent

The residual deformation of impact specimens consists of global deflection and local indentation, as shown in chapter 5. The unloading behaviour with respect to the local behaviour has

been addressed throughout literature. Tan and Sun [103] investigated the residual indentation depths and corresponding unloading path, and He *et al.* [88] addressed the effect of fiber breakage on the permanent dent by means of a knee point diagram (i.e. change in slope in residual dent depth as function of energy). Both topics have been discussed in section 1.4.3 and 1.3.5. Tan and Sun's unloading law is based on impact experiments of composite specimens with rigid foundation. In these experiments Tan and Sun showed that a permanent indentation (α_0) remains after exceeding a critical indentation (α_{cr}). The relation

$$\frac{\alpha_0}{\alpha_{me}} = l - \left(\frac{\alpha_{cr}}{\alpha_{me}}\right)^{\frac{1}{q}} \tag{3.34}$$

is based on the load path during unloading,

$$\frac{F}{F_{me}} = \left(\frac{\alpha - \alpha_0}{\alpha_{me} - \alpha_0}\right)^q, \tag{3.35}$$

which is dependent on both the force (F_{me}) and indentation (α_{me}) at the end of loading phase. The unloading coefficient q is based on experimental data, but $q = 2.5$ is a conservative approximation (see section 1.4.3).

The global unloading behaviour (i.e. residual deflection), on the other hand, is not explicitly addressed in literature and is of limited interest within this thesis. This relates to the fact that only the residual dent is reported in service, whereas the residual deflection is typically not observed. However, in order to compare the entire impact response in the validation experiments, an approximation of the residual deflection path is required. In contrast to the unloading relation for the indentation, it is assumed that the residual deflection is proportional to the extend of delamination and fiber breakage. The progressive damage stages, described in subsection 3.3.2, modified respectively the bending and membrane stiffness terms. The same terms are adjusted in the unloading phase. The final effective K_m^* is assumed equal to the unloading stiffness K_m^u. The unloading bending stiffness K_b^u is given by

$$\begin{aligned} K_b^u &= K_b \frac{w_{_{DTL}}}{w_{me}} + K_b^{^{DTL}} \left(1 - \frac{w_{_{DTL}}}{w_{me}}\right) \quad \text{with} \quad K_b^{^{DTL}} = K_b \frac{w_{_{DTL}}}{w_{me}} \\ K_b^u &= K_b \frac{w_{_{DTL}}}{w_{me}} \left(2 - \frac{w_{_{DTL}}}{w_{me}}\right), \end{aligned} \tag{3.36}$$

which effectively averages the stiffness contributions before and after delamination. The resulting unloading relation for deflection is given by

$$F = F_{me} - \left(K_b^u w_u + K_m^u w_u^3\right) \quad \text{with} \quad w_u = w_{me} - w. \tag{3.37}$$

The residual deflection is obtained by setting Equation 3.37 equal to zero.

3.3.4 Summary of MIDAS-C

The described steps are required to solve for an impact event on a composite target, which is referred to as the inductive solution procedure of MIDAS-C. These steps are integrated in a code developed in the MATLAB programming environment, which are summarized in the flowchart shown in Figure 3.6. A simplified version of the resulting impact response is shown at the bottom of Figure 3.6. MIDAS-C requires a target plate and an impact threat as input. These inputs are defined by their respective object classes as further described in Appendix D.2.

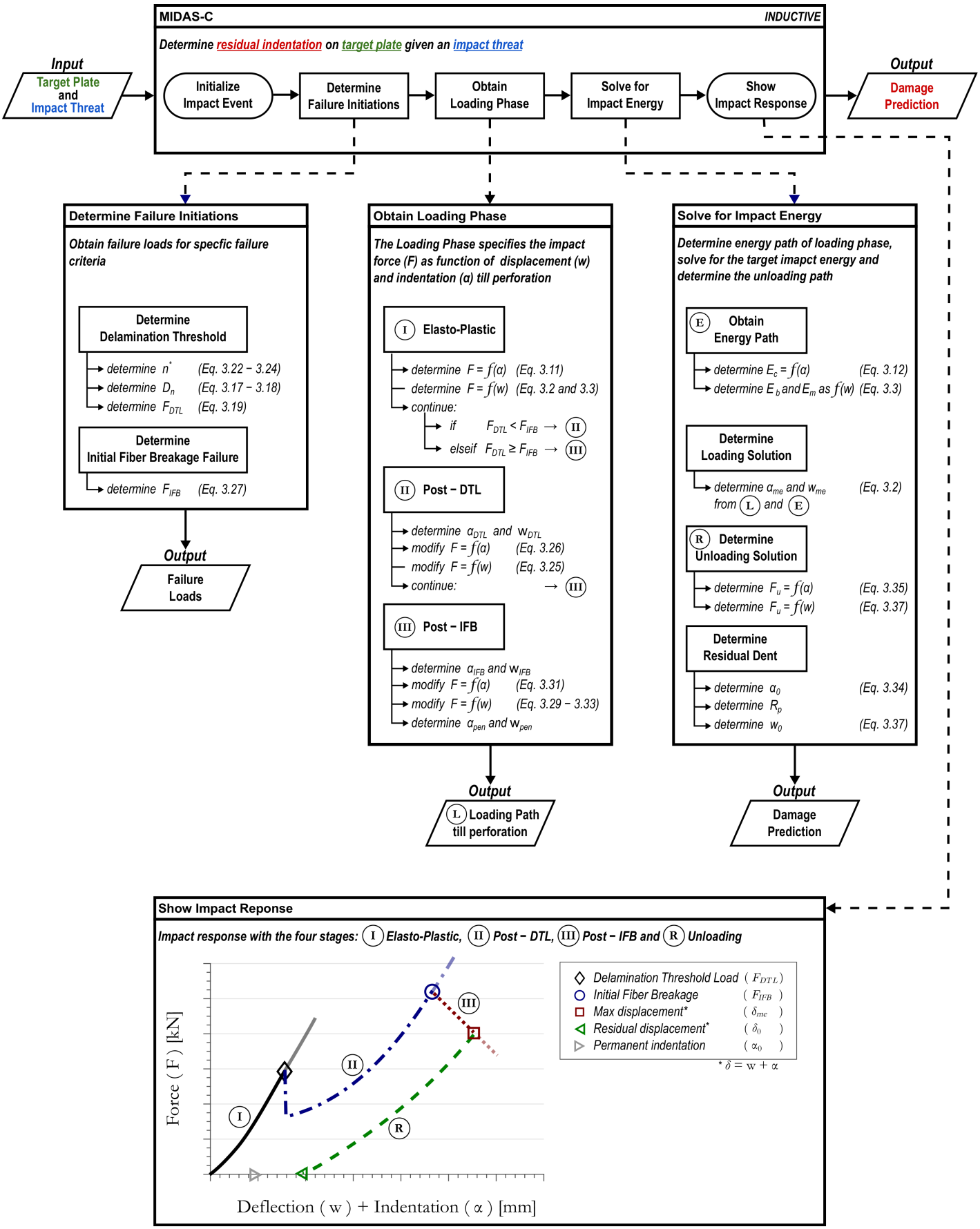

Figure 3.6: Flowchart of inductive procedure of MIDAS-C

3.4 Development of MIDAS-M

Within literature, contact or impact on metallic structures is generally approached by two different methods: either based on contact laws or focused on penetration limits. The region of applicability distinguishes these two generic approaches. On the one hand, contact laws are based on deformations within the contact area (i.e. $r < R_c$), whereas penetration limits focus on the region outside the contact area (i.e. $r \geq R_c$). The local contact laws are often modifications of the elastic theory of Hertz. These modifications are intended to capture the changes in stiffness due to plasticity. Big-Alabo *et al.* [122] for example propose a four-step (elastic, bi-elasto-plastic and fully plastic) model. However, such contact laws are developed by assuming that the target is an elastic half space or has a rigid foundation. The global deformation of flexible targets is typically superimposed, but the indentation deformation behaviour outside the contact area is thereby neglected. Experiments as reported by both Fagerholt *et al.* [18] and Mohotti *et al.* [7], however, indicate that deformation behaviour of steel and aluminum targets upon impact is dominated by the region outside the contact area. This is also shown by their reported residual deformation radii, which are larger than the indentor radii. Penetration limit approaches focus on this outer region, and are intended for flexible or deformable targets. This work aims to develop an analytical model to include deformation outside the contact area. This is achieved by combining the penetration limit methods of Simonsen and Lauridsen [13] and Lee *et al.* [14] and the conventional interaction of local and global deformations using a LPM [11, 15], as shown in Figure 1.11a.

3.4.1 Local impact behaviour

Penetration of metal plates typically occurs at impactor displacements (δ) significantly larger than the plate thickness (t)[14]. Both Lee *et al.* [14] and Mohotti *et al.* [7] have shown that at these large deflections membrane strains dominate around the contact region. Both Simonsen and Lauridsen [13] and Lee *et al.* [14] developed an axi-symmetric theoretical model based on a clamped circular plate (R_0) indented in the center with a spherical impactor (R_i), as shown in Figure 3.7. The plate wraps around the punch and exhibits a pure tensile (membrane) stress (σ_{rr}) outside the contact area. This defines the vertical equilibrium as

$$\begin{aligned} F_c = \quad & 2\pi r\ t\sigma_{rr}\ \sin\psi_{(r)} && \text{with} && \sigma_{rr(r)} = C_0\varepsilon_{rr}^n \\ & && && \varepsilon_{rr} = \tfrac{1}{2}\sin^2\psi \\ & && && t_0 = t\cos\psi_{(r)} \\ = \quad & 2\pi r\ C_0 t_0\ \left[\tfrac{1}{2}\sin^2\psi_{(r)}\right]^n \cos\psi_{(r)}\ \sin\psi_{(r)}, \quad r \in (R_c, R_0) \end{aligned} \tag{3.38}$$

in which ψ represents the deflection angle of the plate as function of distance (r) to the impact center. Yielding of the material is accounted by a power hardening law, which depends on the strength coefficient (C_0) and work hardening exponent (n). The Almansi strain tensor is used to approximate the radial strain (ε_{rr}). This approximation, which differs from both Lee *et al.* [14] (logarithmic strain) and Simonsen and Lauridsen [13] (Green strain), is based on finite element simulations of Liu *et al.* [72]. The contact force as a function of indentation (α) is obtained from the force equilibrium by substitution of the known contact radius (R_c) and contact angle ($\psi_c = \psi_{(r=R_c)}$). This reference point allows solving for the deflection angle of the remainder of the plate by Equation 3.39. In addition, for the indicated clamped circular

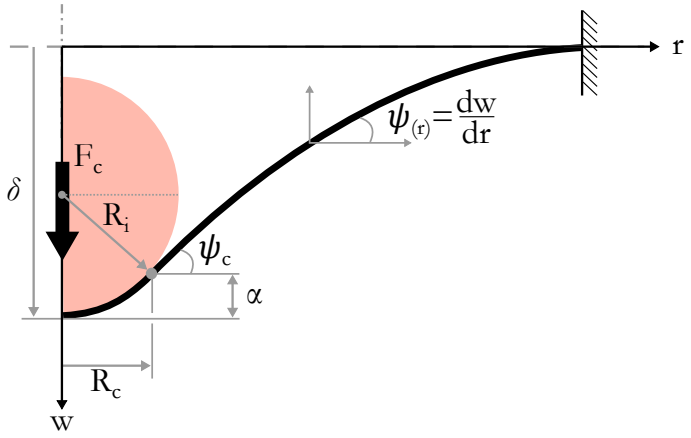

Figure 3.7: Definition of loading state of plate during quasi-static indentation (modified from Lee *et al.* [14])

plate, the corresponding displacement is determined by Equation 3.40 [13]. The penetration limit ($\psi_{c,f}$), as defined by Liu *et al.* [72], follows from the peak of the force displacement curve (i.e $\frac{\partial F_c}{\partial \psi_c} = 0$).

$$\frac{r}{R_i} = \frac{\left[\frac{1}{2}\sin^2\psi_c\right]^n \cos\psi_c \ \sin^2\psi_c}{\left[\frac{1}{2}\sin^2\psi_{(r)}\right]^n \cos\psi_{(r)} \ \sin\psi_{(r)}} \qquad \text{with} \quad \cos\psi_c = 1 - \frac{\alpha}{R_i} \tag{3.39}$$

$$\delta = \alpha + \int_{R_c}^{R_0} \sin\psi_{(r)}(r,\alpha)dr \tag{3.40}$$

$$\cos\psi_{c,f} = \sqrt{\frac{1}{3+2n}} \tag{3.41}$$

The procedure just described approximates the deformation state of the entire plate close to penetration, assuming pure membrane stains and clamped boundary conditions. MIDAS, however, should approximate the entire impact event, which includes bending strains further away from penetration state. In addition, the deformation shape is highly dependent on the geometry and support conditions of the structure. It is assumed that the described behaviour in close vicinity of the point of contact can be assumed valid independent of boundary conditions, whereas the dependency on boundary conditions further away from the point of contact needs to be defined.

3.4.2 Transition of plate deflection to indentation

The assumed deformation shape within MIDAS consists of three regions, as is discussed in section 3.1.2 and illustrated by Figure 3.8. The local deformation due to indentation follows from the geometric shape of the impactor (given by Equation 3.42a), and the global deflection (without indentation) is given by Equation 3.42c. The transition region between the local and global response defines the resulting deformation shape (w_e) of the entire plate.

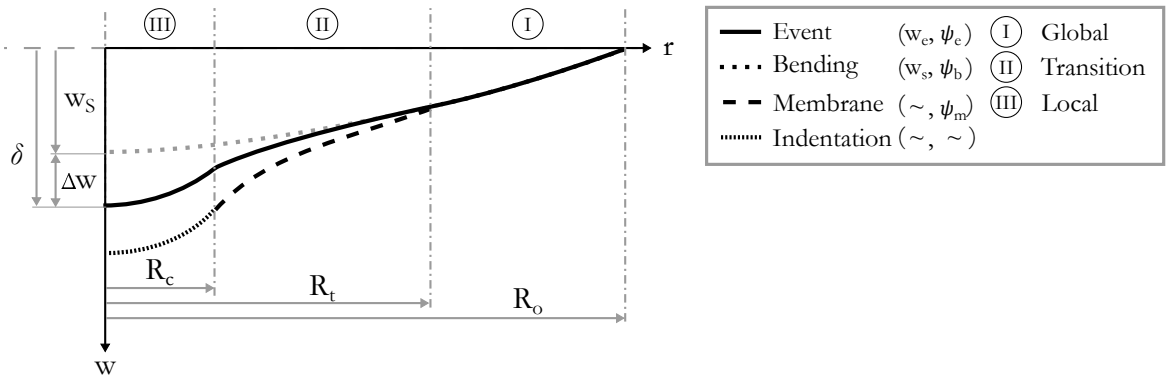

Figure 3.8: The event's plate deflection based on weighted average of bending and membrane limit case solutions

The deformation within the transition region is defined by the integration of the event's deflection angle (i.e $\psi_e = \frac{\partial w_e}{\partial r}$) as given in Equation 3.42b.

$$w_{e\,(r)} = \begin{cases} \text{I} \quad w_{s\,(r)} & \text{for } R_t < r < R_0 \quad (3.42a) \\ \text{II} \quad w_{s\,(r=R_t)} + \int_{R_t}^{r} \sin\psi_{e(r)}\, dr & \text{for } R_c < r < R_t \quad (3.42b) \\ \text{III} \quad w_{e\,(r=R_c)} + R_i - \sqrt{R_i^2 - r^2} & \text{for } r < R_0 \quad (3.42c) \end{cases}$$

The deflection angle within the transition region is yet to be defined. The contact and global deflection approximations, described in section 3.2 and 3.4.1, are essentially limit case solutions for the transition region. This is illustrated by respectively the ▪▪▪ and · · · lines in Figure 3.8. These cases refer to either a complete membrane or bending state of loading, while a combination of both is present during an impact event. The resulting plate deformation, illustrated with ▬, is effectively a weighted average of these limit cases. The respective weights are the relative bending (F_b) and membrane (F_m) force contributions given by the interaction in the LPM.

$$\psi_{e(r)} = \psi_{b(r)}\,\frac{F_b}{F_c} + \psi_{m(r)}\frac{F_m}{F_c} \quad (3.43)$$

in which $\psi_{m(r)}$ and $\psi_{b(r)}$ are the deflection angles of both limit cases. These angles follow from the penetration limit approach in Equation 3.39 and the derivatives of the global plates deflection (i.e $\frac{\partial w_s}{\partial r}$ where w_s is given by either Equation 3.6 or 3.8). The transition point (R_t) is defined as the intersection of the deflection angle of both limit cases (i.e $\psi_{m(r)} = \psi_{b(r)}$).

The resulting deflection allows to solve for the contact energy, which can be seen as additional work of the contact force over the relative displacement (Δw) between plates bending deflection (w_s) and the impactor displacement(δ):

$$E_c = \int_0^{\Delta w} F_c\, d\,\Delta w \qquad \text{with} \quad \Delta w = \delta - w_{s\,(r=0)}. \quad (3.44)$$

The definitions of the plates local and global impact response allows to solve the loading phase of the impact event, using Equation 3.1.

3.4.3 Unloading and permanent dent creation

The description of local, global and transition behaviour has focused on the loading phase of an impact event. Within that phase, the kinetic impact energy is converted in both elastic and plastic deformation of the structure. The goal of the unloading phase is to obtain the residual dent by quantifying both the elastic and plastic deformation contributions. These contributions follow from the strain distribution of the plate, which is defined as

$$\varepsilon_{(r)} = \varepsilon_{m\,(r)} + \varepsilon_{b\,(r)} \tag{3.45a}$$

$$\varepsilon_{m\,(r)} = \frac{1}{2}\sin\left(\frac{dw}{dr}\right)^2 \tag{3.45b}$$

$$\varepsilon_{b\,(r)} = -z\frac{d^2w}{d^2r}. \tag{3.45c}$$

where ε_b,ε_m and z respectively refer to the bending, membrane strains and distance to the neutral axis. The plastic portion of the strains cause the residual dent, while elastic strains are assumed to restore to the original geometry. The plastic radius (R_p) is obtained by solving Equation 3.45a for the yield strain (ε_y). The resulting residual deflection (w_p) is given by

$$w_{p\,(r)} = \begin{cases} w_{e\,(r)} - (R_p - r)\tan\left(\psi_{e\,(r)}\right) & \text{for } R_c < r < R_p \quad (3.46a) \\ w_{p\,(R_c)} + R^* - \sqrt{R^{*2} - r^2} & \text{for } r < R_c \quad (3.46b) \end{cases}$$

in which the relaxed impactor radius (R^*) is defined by Equation 3.47. This relaxed radius is a consequence of the relaxation of the dent, while the permanent dent radius remains constant.

$$R^* = \frac{R_c}{\sin\psi_{p(R_p)}}. \tag{3.47}$$

3.4.4 Summary of MIDAS-M

The described steps are required to solve for an impact event on a composite target, which is referred to as the inductive solution procedure of MIDAS-M. These steps are integrated in a code developed in the MATLAB programming environment, which are summarized in the flowchart shown in Figure 3.9. The final step `ShowImpactResponse` provides a graphical representation of the results, which are illustrated by the simplified version of the resulting impact response and corresponding deflection profiles at the bottom of Figure 3.9. MIDAS-M requires a target plate and an impact threat as input. These inputs are defined by their respective object classes as further described in Appendix D.2.

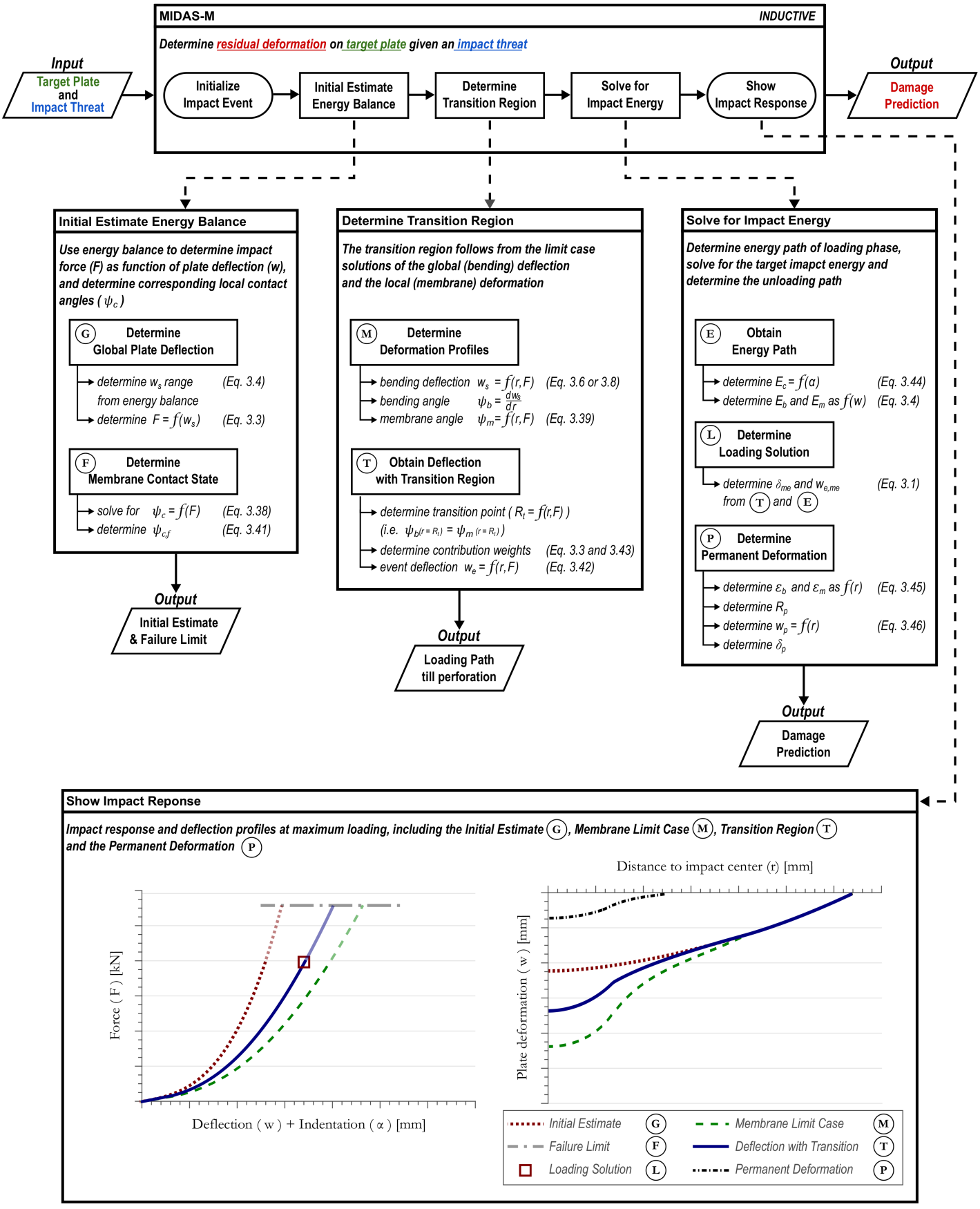

Figure 3.9: Flowchart of inductive procedure of MIDAS-M

3.5 Overview of the deductive approach of MIDAS

The inductive procedures of respectively MIDAS-C and -M are summarized in subsection 3.3.4 and 3.4.4. These allow to predict impact damages for both composite and metal structures given a specific impact threat. The goal of this thesis requires a deductive solution (i.e. to determine an impact threat given the damage dimensions). The deductive procedure implements the inductive solutions within a MATLAB code to estimate the impact threats. This is summarized in the flowchart shown in Figure 3.10. An example of threat map is shown in the last step of the model.

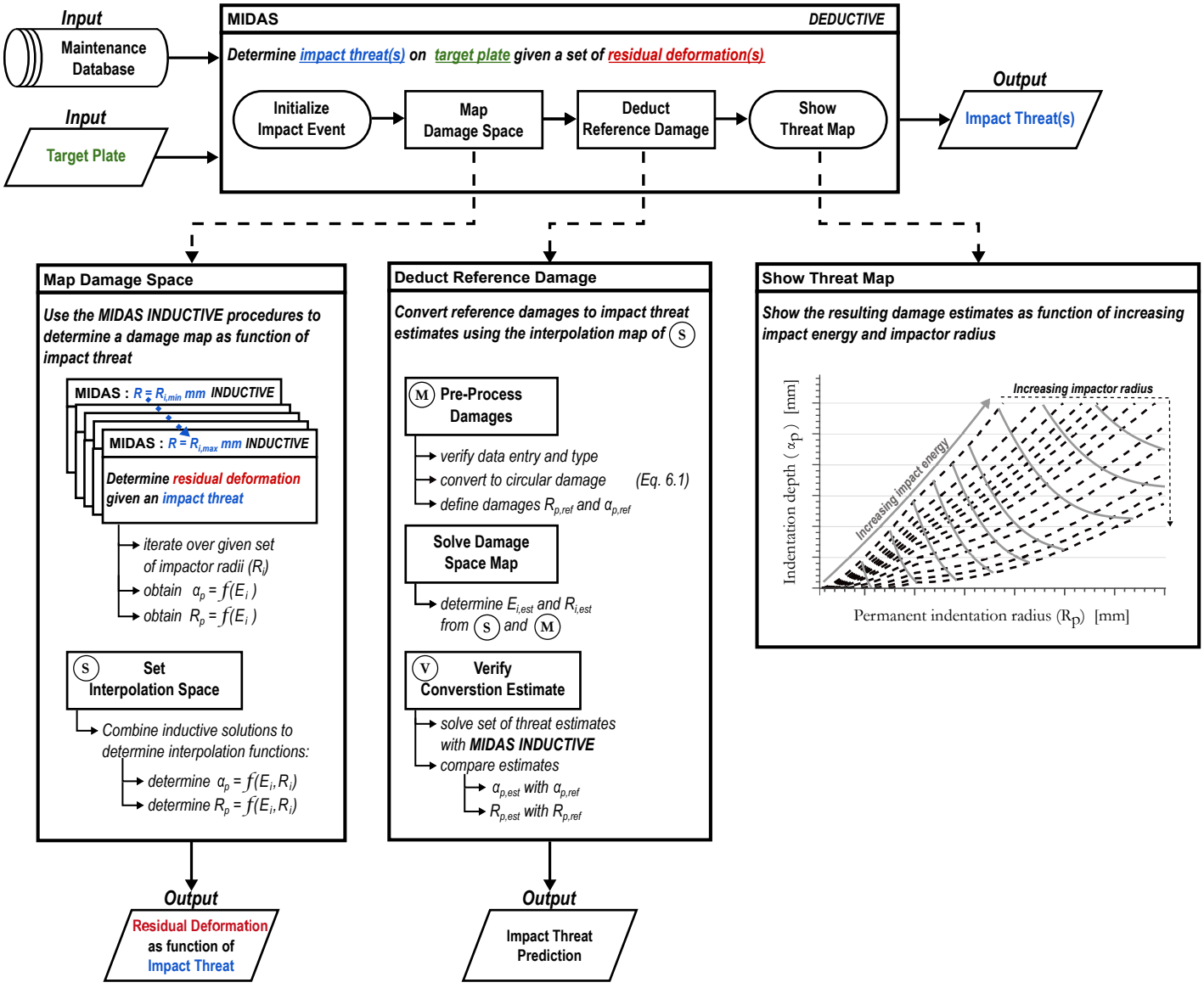

Figure 3.10: Flowchart of deductive procedure of MIDAS

Chapter 4

Verification

The goal of this chapter is to verify the analytical models described in chapter 3. A FEM is developed to evaluate the impact on both metal and composite structures. The verification of both versions of MIDAS is discussed separately. Section 4.2 addresses both the validity of the FEM model and the verification of MIDAS-M for impact on metal targets. Similarly, the comparison of experimental results, FEM and MIDAS-C for impact on composite targets is described in section 4.3. The experimental data used to validate the numerical models is obtained from literature.

4.1 Development of numerical impact problem

The FEM is intended to simulate impact scenarios similar to the cases assumed for the analytical model. In addition, the FEM model is compared with results from literature (both experimental and numerical results). As the numerical model is required to reproduce a wide range of impact scenario's, the model is created in the Abaqus Scripting environment. Since the dimensions and geometry are scenario dependent, the description of the numerical model is divided in a general model and a geometry dependent description.

4.1.1 General model

The model is developed using the commercially available finite element program Abaqus . The general model consists of two parts: the impactor and the impacted structure (respectively referred to as punch and target). The punch is modelled as a *Discrete Rigid Surface* using 3D bi-linear rigid 4-nodes quadrilateral elements (R3D4). The impactor mass and impact velocity are assigned to a reference point at the punch's center of mass, which is rigidly constrained to its surface. The reference point is only allowed to move perpendicular to the target surface. The target is modelled as a *Deformable Solid*, using 8-node linear brick elements with reduced

integration(C3D8R). *Enhanced Hourglassing control* is applied to minimize uncontrolled element distortions, which could occur due to zero strains at the single integration point of C3D8R elements [123]. The contact behaviour is modelled using ABAQUS' GENERAL CONTACT algorithm including both tangential and normal contact behaviour. A penalty friction formulation is applied to the tangential behaviour using a friction coefficient (μ) of 0.15, while hard contact is enforced in the normal direction. This allows separation after contact but restricts penetration of the surface nodes [123]. The effect of the friction coefficient is evaluated in Appendix E.1, which shows that the differences between friction coefficients ranging from 0.05 to 2.00 are respectively within 1% and 10% for the max displacement and the peak force estimations. The dynamic nature of the impact event is modelled using ABAQUS DYNAMIC/EXPLICIT step. The explicit direct integration procedure applies an automatic time incrementation scheme using a global estimator to determine stable time increments [123]. Dependent on the target's material constituents, different constitutive material models are defined in the ABAQUS/EXPLICIT solver to account for damage.

Stress-strain behaviour of metal constituents

As described in section 1.3, metals are expected to plastically deform and eventually perforate during an impact event.The intended goal of the numerical model is to compare deformation characteristics of low-velocity impact events, in which perforation typically does not occur (i.e. the target data provided by a major European carrier consist of dents and not holes). The constitutive behaviour of metal should therefore capture the deformation characteristics in terms of stresses and strains, while failure or damage characteristics are not considered (i.e. a damage criterion and/or element deletion is not applied). The strain-hardening during impact should be captured by the constitutive model. This is typically modelled using either perfect plastic, bi-linear (elasto-plastic) or non-linear (Johnson-Cook) constitutive models[7]. The Johnson Cook model is typically preferred in literature, due to its ability to capture the non-linear stress strain behaviour, including strain rate, temperature effects and stress triaxiality[124]. However, the Johnson-Cook model, as given by

$$\sigma = \left(A + B\epsilon^{n}\right)\left(1 + C\ln\frac{\dot{\epsilon}}{\dot{\epsilon}_0}\right)\left(1 - T^{m}\right), \tag{4.1}$$

requires five experimentally obtained material constants (A,B,C,n and m). In addition, a reference strain rate $\dot{\epsilon}_0$ and homologous temperature T have to be defined. As alternative, a bi-linear stress-strain relation is implemented to model the constitutive behaviour. This consists of the true stress and strain relation using the frequently reported yield (σ_y), ultimate (σ_u) strength and fractures strain (ε_f) of the material. The validity of both constitutive behaviours is compared in subsection 4.2.1.

Stress-strain behaviour for composite constituents

In comparison to the isotropic and strain-hardening behaviour of metals, composite laminates are assumed to be orthotropic and experience constituent dependent failure modes. The damage evolution behaviour is therefore modelled by the reducing element stiffness terms

dependent on both the constituent and load dependent failure modes. This is incorporated using a user-defined 3D damage model (VUMAT), based on Hashin's failure criterion[125]. The orthotropic stress strain relation is defined as,

$$\begin{pmatrix} \sigma_{11} \\ \sigma_{22} \\ \sigma_{33} \\ \sigma_{12} \\ \sigma_{23} \\ \sigma_{13} \end{pmatrix} = \begin{bmatrix} C_{11} & C_{12} & C_{13} & 0 & 0 & 0 \\ C_{12} & C_{22} & C_{23} & 0 & 0 & 0 \\ C_{13} & C_{23} & C_{33} & 0 & 0 & 0 \\ 0 & 0 & 0 & 2G_{12} & 0 & 0 \\ 0 & 0 & 0 & 0 & 2G_{23} & 0 \\ 0 & 0 & 0 & 0 & 0 & 2G_{31} \end{bmatrix} \begin{pmatrix} \varepsilon_{11} \\ \varepsilon_{22} \\ \varepsilon_{33} \\ \varepsilon_{12} \\ \varepsilon_{23} \\ \varepsilon_{31} \end{pmatrix}, \tag{4.2}$$

in which the directional stiffness terms (C_{ij} and G_{ij}) are dependent on the undamaged elastic constants (C^0_{ij} and G^0_{ij}) and the constituent failure states (d_f and d_m). These damaged and undamaged constants are respectively given by Equation 4.3 and 4.4. The failure variables can range from 0 to 1, which corresponds respectively to no reduction or a complete reduction of stiffness.

$$C_{11} = (1 - d_f)C^0_{11} \tag{4.3a}$$

$$C_{ij} = (1 - d_f)(1 - d_m)C^0_{ij} \qquad \text{with} \quad i,j = 1,2,3 \quad \& \quad i + j \neq 2 \tag{4.3b}$$

$$G_{ij} = (1 - d_f)(1 - 0.9d_{mt})(1 - 0.5d_{mc})G^0_{ij} \qquad ij = 12,23,13 \tag{4.3c}$$

$$C^0_{ii} = E_{ii}\frac{1 - \nu_{ik}\nu_{ki}}{\Gamma} \qquad \text{with} \quad i,j,k = 1,2,3 \quad \& \quad i \neq k \neq j \tag{4.4a}$$

$$C^0_{ij} = E_{ii}\frac{\nu_{ji} - \nu_{ki}\nu_{jk}}{\Gamma} \qquad \Gamma = (1 - \nu_{12}\nu_{21} - \nu_{23}\nu_{32} - \nu_{31}\nu_{13} - 2\nu_{21}\nu_{32}\nu_{13}) \tag{4.4b}$$

The element based failure state variables d_f and d_m refer to respectively the failure state of the matrix and fiber constituent. These failures variables are a combination of the load dependent failure states d_{mc}, d_{mt}, d_{fc} and d_{ft}, as given in Equation 4.5. The subscripts c and t refer to compression or tension load case, while m and f refer to the matrix or fiber constituent. The initiation of the respective failure modes is determined using Hashin's failure criterion, as given in Equation 4.6.

$$d_f = 1 - (1 - d_{ft})(1 - d_{f,c}) \tag{4.5a}$$

$$d_m = 1 - (1 - d_{mt})(1 - d_{m,c}) \tag{4.5b}$$

The damage evolution behaviour is described on a per element basis by the stress-strain relation of Equation 4.2 in combination with Equation 4.3, 4.4 and 4.5. A gradual reduction of failure state variables would allow a progressive damage analysis. Within this analysis, a simplified conservative approach is considered that neglects this progressive damage behaviour and instantaneously degrades the elements' corresponding stiffness matrix terms upon initiation of damage. The failure variables are set to 0.95 (instead of 1), which corresponds to a stiffness reduction of 95%. The stiffness is not reduced by 100%, as this would lead to computational singularities (i.e. a zero stiffness element is effectively a free moving body, but still restrained by surrounding elements). The individual failure states (d_{mc}, d_{mt}, d_{fc} and d_{ft}) are obtained from Hashin's constituent and mode dependent failure criterion given in Equation 4.6.

Tensile fiber failure $\sigma_{11} \geq 0$:

$$\left(\frac{\sigma_{11}}{X_T}\right)^2 + \frac{\sigma_{12}^2 + \sigma_{13}^2}{S_L^2} = \begin{cases} \geq 1 & \text{failure} \quad d_{ft} = 0.95 \\ < 1 & \text{no failure} \quad d_{ft} = 0 \end{cases} \tag{4.6a}$$

Compressive fiber failure $\sigma_{11} < 0$:

$$\left(\frac{\sigma_{11}}{X_C}\right)^2 = \begin{cases} \geq 1 & \text{failure} \quad d_{fc} = 0.95 \\ < 1 & \text{no failure} \quad d_{fc} = 0 \end{cases} \tag{4.6b}$$

Tensile matrix failure $\sigma_{22} + \sigma_{33} \geq 0$:

$$\left(\frac{\sigma_{22} + \sigma_{33}}{Y_t}\right)^2 + \frac{{\sigma_{23}}^2 - \sigma_{22}\sigma_{33}}{S_T^2} + \frac{{\sigma_{12}}^2 - {\sigma_{13}}^2}{S_L^2} = \begin{cases} \geq 1 & \text{failure} \quad d_{mt} = 0.95 \\ < 1 & \text{no failure} \quad d_{mt} = 0 \end{cases} \tag{4.6c}$$

Compressive matrix failure $\sigma_{22} + \sigma_{33} < 0$:

$$\begin{aligned} \frac{\sigma_{22} + \sigma_{33}}{Y_c}\left[\left(\frac{Y_c}{2S_T}\right)^2 - 1\right] + \left(\frac{\sigma_{22} + \sigma_{33}}{2S_T}\right)^2 \\ + \frac{{\sigma_{23}}^2 - \sigma_{22}\sigma_{33}}{S_T^2} + \frac{{\sigma_{12}}^2 - {\sigma_{13}}^2}{S_L^2} = \begin{cases} \geq 1 & \text{failure} \quad d_{mc} = 0.95 \\ < 1 & \text{no failure} \quad d_{mc} = 0 \end{cases} \end{aligned} \tag{4.6d}$$

where X, Y and S are to the lamina's longitudinal, transverse and in-plane shear strength quantities, and the subscripts t, c, L and T refer to the tensile, compression, longitudinal and transverse direction.

4.1.2 Dimensional and geometry dependent model characteristics

The reference results and defined analytical model concern centrally impacted rectangular or circular flat plates that are either clamped or simply supported. This allows to simulate only a quarter of the model enforcing symmetry conditions on the inner boundaries. A schematic illustration of both a circular and rectangular plate as modelled in Abaqus is shown in Figure 4.1.

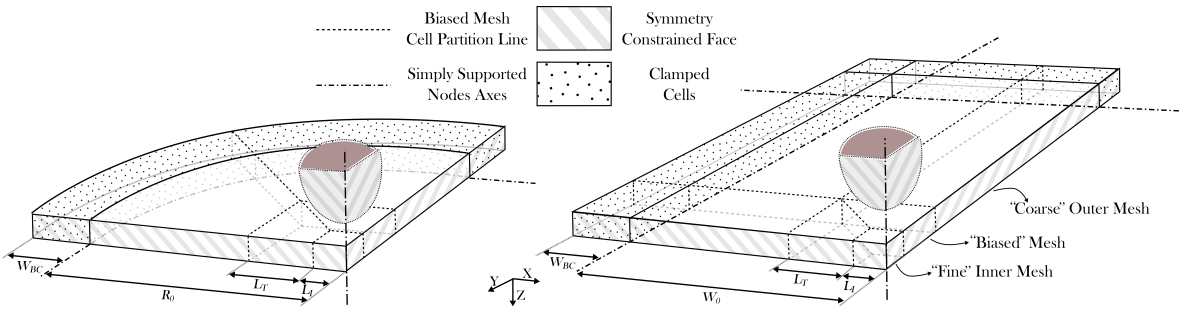

Figure 4.1: Schematic impact scenario in FEM, including boundary conditions and meshing partitions

Boundary conditions

The plates consist of a free and a boundary region, which are respectively indicated by the clear and dotted areas. This follows from convention in experiments, in which the target plate is typically placed on or clamped to a rigid substructure with a central gap. The boundary region of the target is used to enforce boundary conditions. Three types of constraints are used in the FEM models, dependent on the boundary conditions:

Symmetry Both the punch and target have a symmetry constraint on the shaded faces on the XZ- and YZ-plane. This implies that the out of plane displacements and rotations are constrained on the respective faces.

Clamped If the target is clamped to the substructure, the displacement and rotational degrees of freedom of the nodes in the (dotted) boundary region are set to zero.

Pinned In a simply supported scenario, the inner bottom edge of the boundary region is pinned (i.e only the displacement degrees of freedoms are fixed). This edge corresponds to the gap of the substructure.

Meshing Strategy

The FEM intends to reproduce the indentation and deformation behaviour of the target upon impact. A sufficiently fine mesh is required within the contact region to properly capture the indentation process. The global deflection can be captured with a coarser mesh. To that extent, two types of meshing strategies are considered: an uniform and biased mesh. The distinction between both strategies relate to the generic trend that computation time increases for a larger number of elements.

Both the uniform mesh and the refined region L_I of the biased mesh have a mesh size of χ_I. The mesh size linearly increases over a distance L_T to χ_O. The transition length L_T scales proportional to the bias ratio (i.e. $f_{bias} = \chi_O/\chi_I = L_T/L_I$). The through-thickness mesh size χ_t differs for metals and composites. In the composite case, each ply is modelled individually with corresponding material orientation and properties (i.e. χ_t is equal to t_{ply}). For the metal case, χ_t values of 0.5 or 1.0 mm are typically used in literature [7, 82]. The through-thickness mesh size has a significant effect on the computation time. The necessary time marching scheme requires a stable time increment. This increment effectively scales with the smallest element dimensions (i.e. a smaller element size implies a smaller time increment and thereby a longer computation time).

4.2 Verification of MIDAS-M

The verification of MIDAS-M considers the metal variant of MIDAS, as summarized in subsection 3.4.4. This requires a validated numerical model for impact on metal targets. The FEM model is therefore first compared with experimental results in subsection 4.2.1. This comparison is used to determine the appropriate model settings of the FEM. subsection 4.2.2 addresses the resulting verification of MIDAS-M.

4.2.1 Comparison of metal FEM with literature

The validity of the metal variant of the FEM is determined based on experimental results found in literature. Fagerholt *et al.* [18] reported a study dedicated to the out-of-plane deformation measurements of AA5083-H116 plates subject to impact at three different velocities (i.e 7.31, 7.92 and 10.69 m/s). In comparison to the assumed spherical impactor in MIDAS, Fagerholt *et al.* [18] used a 30 mm diameter steel hardened blunt-nose projectile of 19.0 kg. The target plate consisted of 5 mm thick square plate with sides of 600 mm, which was mounted between two steel rings with inner diameter of 500mm. The relevant material properties of AA5083-H116 are summarized in Table 4.1.

Table 4.1: Material properties of AA5083-H116[18, 124]

Elasto-Plastic (EP)			**Johnson-Cook (JC)**				
σ_y	σ_u	ε_f	A	B	n	$\dot{\varepsilon}_0$	C
MPa	MPa	%	MPa	MPa	-	s^{-1}	-
261	360	13.1	206.2	424	0.362	1	0.01

In addition to the validation of the FEM, the appropriate model settings for the verification of MIDAS need to be determined. The reference case of 7.31 m/s is used to perform a mesh convergence, and to evaluate both the Johnson-Cook (JC) and elasto-plastic (EP) material models. The convergence of the FEM is based on the relative error of the maximum displacement ε_δ and force ε_F, which is defined as

$$\varepsilon_\delta = \left| \frac{\delta_\chi - \delta_{\chi=0.5\text{mm}}}{\delta_{\chi=0.5\text{mm}}} \right| 100\% \qquad \text{and} \qquad \varepsilon_F = \left| \frac{F_\chi - F_{\chi=0.5\text{mm}}}{F_{\chi=0.5\text{mm}}} \right| 100\%. \tag{4.7}$$

The left hand side of Figure 4.2a shows that both relative errors become within 1% for element size of 1.0mm or smaller, while the computation time (CT) on the right hand side rapidly increases. An alternative measure of convergence is the maximum artificial strain energy (AE), which should be minimized for an acceptable solution (i.e large values indicate significant distortion control in terms of hourglassing [123]). Figure 4.2b confirms that acceptable convergence is achieved with an element size 1.0 mm (i.e. $AE \leq 0.35\%$). The FEM models for two different impact scenarios are shown in Figure 4.3. These correspond to meshes for either a clamped circular and a simply supported square plate using in respectively the comparison with experimental results and the verification of MIDAS in the next section.

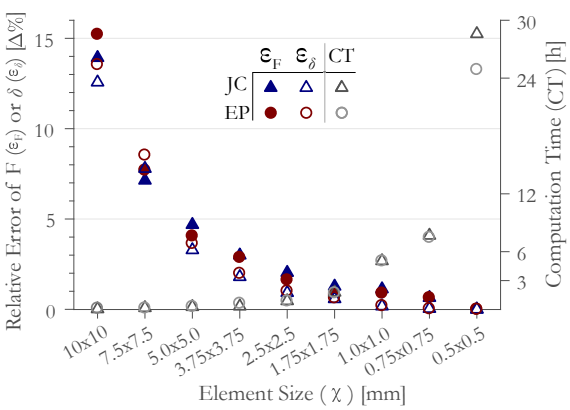

(a) (LHS) Relative error of displacement/force and (RHS) Computation time versus element size

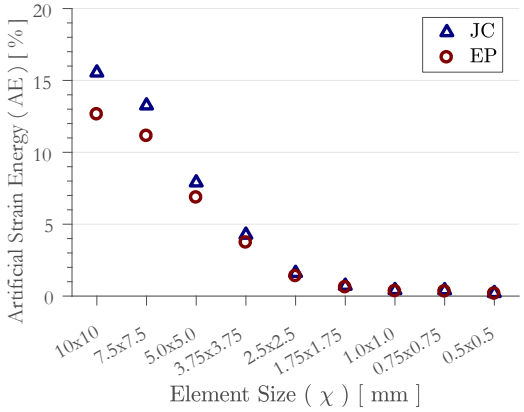

(b) Artificial strain energy versus element size

Figure 4.2: Mesh convergence of FEM model with respect to Fagerholt's impact scenario with a velocity of 7.31 m/s

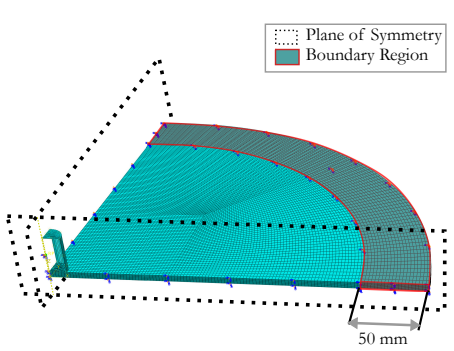

(a) Clamped circular plate with R_0 = $250mm$ and t = $5mm$ impacted by cylindrical impactor of R_i = $15mm$

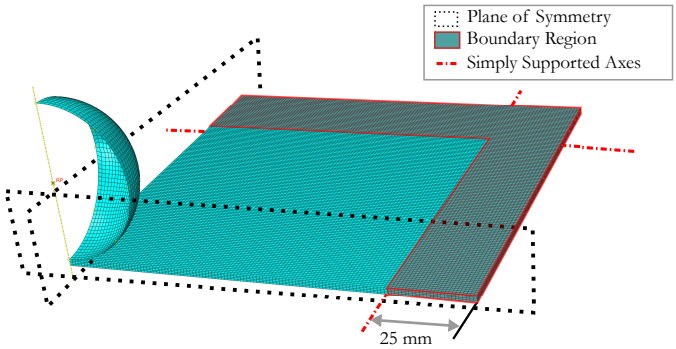

(b) Simply supported square plate with R_0 = $100mm$ and t = $5mm$ impacted by spherical impactor of R_i = $25mm$

Figure 4.3: Representation of FE model indicating the respective boundary regions and using χ_t = $0.5mm$ and χ_n = $1.0mm$

The experimental plate was perforated at the at the highest impact velocity, whereas damage characteristics and corresponding element deletion settings have not been included in the FEM. The impact response is properly reproduced up to initiation of penetration (i.e up to 2.6ms), as is shown in Figure 4.5c. The impact responses of all three cases are evaluated in terms of the force history and the out-of-plane deflection profile, as shown respectively in Figure 4.4 and 4.5. The numerically predicted out-of-plane deflection profiles are in good agreement with the reported experimental results of Fagerholt *et al.*. Moreover, no significant differences are apparent between the deflection profiles of both material models. Comparison of the force histories in Figure 4.5 shows that the duration of impact is properly predicted, but the impact force is consistently overestimated.

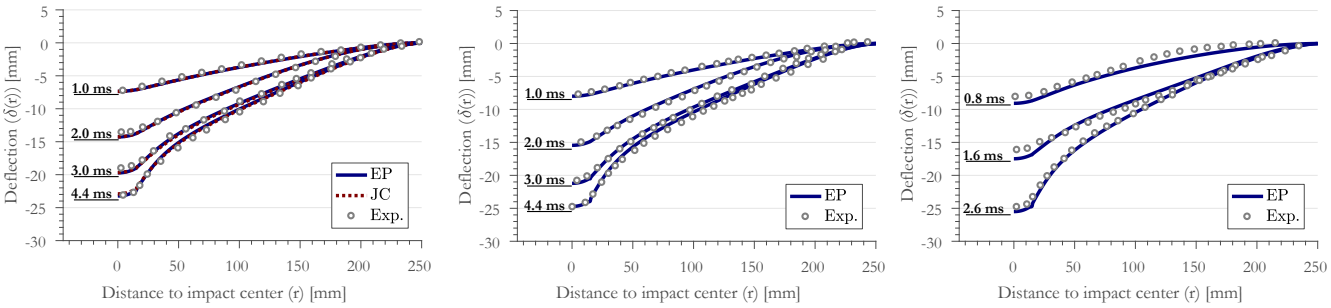

(a) V_i = 7.31m/s **(b)** V_i = 7.92m/s **(c)** V_i = 10.69m/s

Figure 4.4: Comparison of deformation profiles between the FEM and Fagerholt's experimental results at three different impact velocities[18]

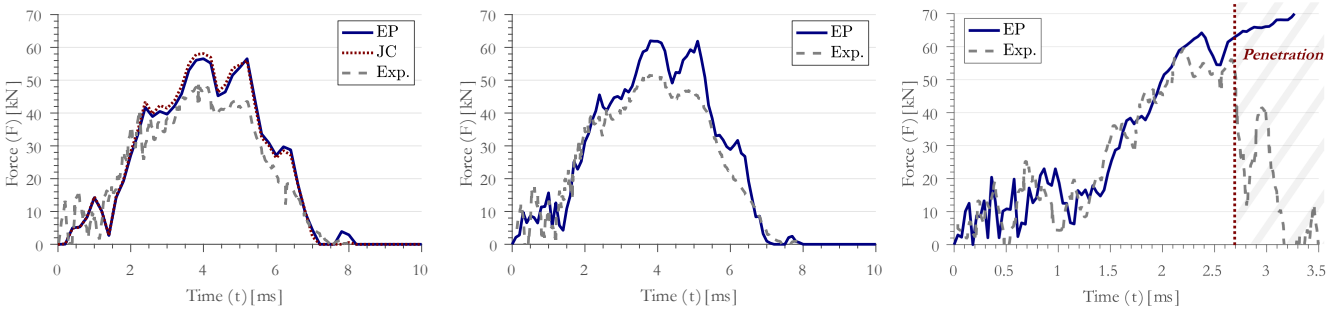

(a) V_i = 7.31m/s **(b)** V_i = 7.92m/s **(c)** V_i = 10.69m/s

Figure 4.5: Comparison of load history between the FEM and Fagerholt's experimental results at three different impact velocities [18]

Minor differences are observed between the force response estimates of both material models, as shown in Figure 4.5a. These differences are, however, not significant in comparison to offset with the experimental force history. Both constitutive material models are therefore assumed to be equally appropriate. The bi-linear stress strain relation is used in the remainder of this work due to its simplicity compared to the Johnson-Cook model (i.e it requires less material constants).

4.2.2 Comparison of MIDAS-M with the metal FEM

The validated FEM model is compared with predictions of MIDAS-M. The comparison is performed over a range of scenarios to determine a range of confidence in which MIDAS-M can be used. The range of scenarios considered is based on dimensions of wide-body aircraft. The verification of MIDAS-M is performed in two steps. The initial verification step considers the loading phase of the impact event, and the second step evaluates the permanent deformation estimates.

Reference cases for verification

MIDAS-M is developed to analyze impact events on aircraft structures (i.e. aircraft fuselage or wing skins). The described model simplifies aircraft structures to a flat plate with a size equal to the stringer ($a_{stringer}$) and frame pitch (b_{frame}). An overview of fuselage designs of wide-body aircraft is given by CODAMEIN (Composite Damage Metrics and Inspection)[26]. According to the CODAMEIN report, metal aircraft, such as B777, use aluminum Al2524 as the primary material for skin, frame, and stringers. The range of fuselage dimensions and relevant material properties of aluminum Al2524 are summarized in respectively Table 4.2 and 4.3.

Table 4.2: Material properties of Al2524 [126, 127]

Elasto-Plastic (EP)		
σ_y MPa	σ_u MPa	ε_f %
275.8	413.7	21

Table 4.3: Range of wide-body aircraft fuselage dimensions [26]

Aircraft Dimensions		
$a_{stringer}$ mm	b_{frame} mm	t_{skin} mm
230	530	1.0-2.6

The inscribed circle[1] of the plate governs the membrane behaviour of the plate. To that extent, the verification of MIDAS is based on square plates using the stringer pitch estimates. This work focuses on Boeing 777 aircraft fleet, which has relatively large stringer pitch compared to the indicated range. The verification uses a plate size of 200 and 300 mm, which are the boundaries of practical scenarios. In addition, the indicated thickness range is relatively small. A thickness range of 1-4mm is considered and impactor radii of 10, 25 and 75 mm are used.

Result comparison

The inductive solution procedure consists of loading and unloading step. The end of loading is achieved when the specimen fully absorbs the kinetic impact energy (i.e. impactor velocity is zero). The maximum force and displacement characterize this moment. The comparison of the predicted and simulated maximum force and displacement can, therefore, be seen as an indicator of the validity of the energy conversion. Various combinations of plate and impactor dimensions are compared. These scenarios are all evaluated at four reference energy levels (5, 10, 25 and 50 J). Figure 4.6a shows a comparison of three different impactor radii (10, 25 and 75mm) on two different plates sizes (200 and 300 mm) using a constant thickness of 2mm. Using constant plate size and impactor radius (i.e. respectively 200 mm and 25 mm) Figure 4.6b compares the effect of thickness. In both figures, the predicted loading path of MIDAS-M is shown with either ▪ ▪ ▪ or · · · lines, and the crosses indicated the individual case predictions at the four reference energy levels (5, 10, 25 and 50 J). The results from the FEM simulations are indicated at the same energy levels with various marker types depending on the comparison scenario.

[1] The inscribed circle refers to circle centered at the point of impact that reaches up to the nearest boundary. The results in a circle with a diameter equal to the smallest side of a rectangular plate in case of an impact on the plates center

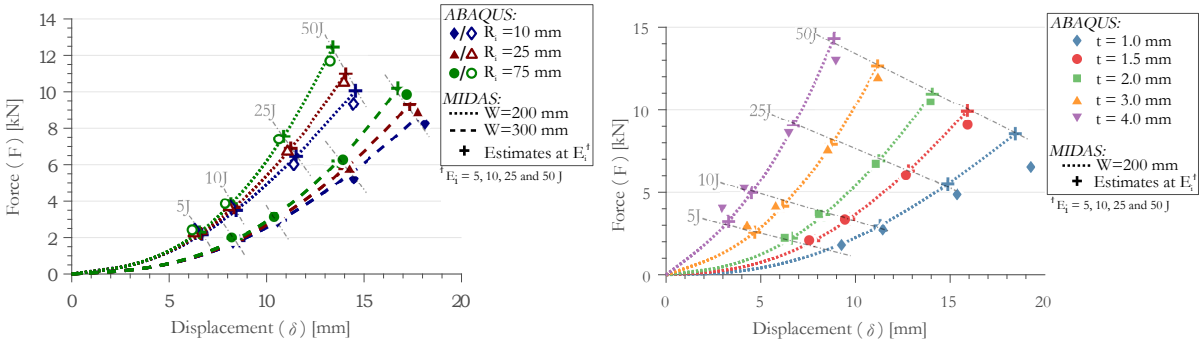

(a) Variation of impactor and plate size **(b)** Variation of plate thickness

Figure 4.6: Comparison of MIDAS-M with FEM simulations

The trends shown in both Figure 4.6a and 4.6b indicate that predicted loading paths of MIDAS-M are in good agreement with the FEM simulations. The effect of changing the impactor radius, plate width or thickness is properly captured by MIDAS-M. Even though the differences increase at higher impact energies, the error remains within 10% except for plates with a thickness of 1mm. The error of predicted force increases between impact energies of 25 and 50 J for these 1mm plates. Investigation of the FEM results shows that this discrepancy results from excessive element distortion in the boundary region. MIDAS-M does not include this distortion, and further work is required to investigate the behaviour of thin flexible targets.

In addition to the force-displacement paths, the (residual) deformation shape and contact radius are relevant characteristics to compare the FEM and analytical model. The maximum and permanent deformations of several scenarios are compared in Figure 4.7, 4.8 and 4.9. Figure 4.7 and 4.8 show results of four energy levels for 2mm thick and 200mm wide plates with impactor radii of respectively 10 and 75 mm, while Figure 4.9 compares the deformation shapes of different thicknesses with an impactor radius of 25mm and impact energy 50J. The contact radii estimates of both the FEM and MIDAS-M are approximately the same, while the validity of the deformation shape approximation varies. Effectively, it can be said that the validity of the deformation shape varies with plate thickness.Figure 4.9 shows the deformation shape is not properly reproduced for thicker plates (t = 3-4 mm) compared to the estimates of thin plates (t= 1.5-2 mm). Similarly, the error in plastic radius estimates is significant for the thicker plates. The estimates for plates of 1.5-2mm are in good agreement with FEM. The plastic range is underestimated at lower impact energies, but the differences become smaller at 25 and 50J. Similarly, comparison of the permanent dent estimates show differences of approximately 20% around 25-50J, while the error is larger at 5-10J.

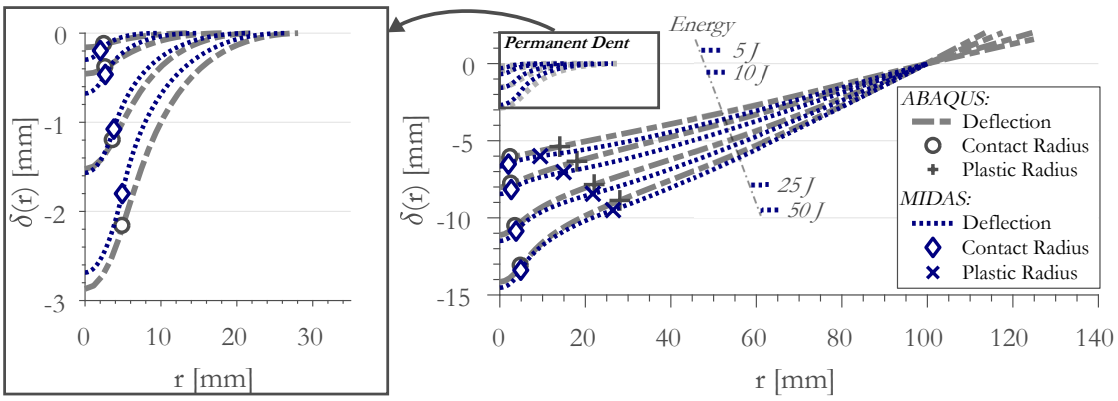

Figure 4.7: Maximum and permanent deformation of MIDAS-M and FEM for 200mm wide and 2 mm thick plate impacted with an impact radius of 10 mm at four impact energies (5/10/25/50 J)

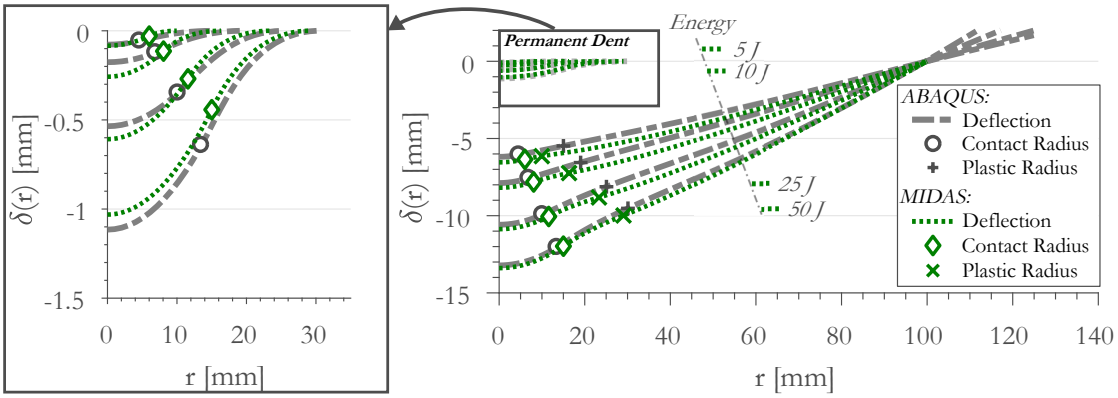

Figure 4.8: Maximum and permanent deformation of MIDAS-M and FEM for 200mm wide and 2 mm thick plate impacted with an impact radius of 75 mm at four impact energies (5/10/25/50 J)

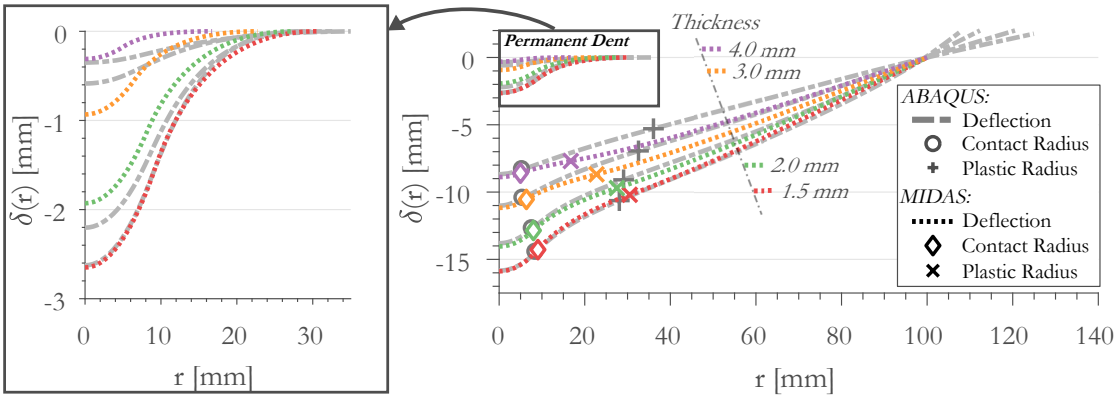

Figure 4.9: Maximum and permanent deformation of MIDAS-M and FEM for 200mm wide plate and varying thickness (1.5/2/3/4 mm) impacted at 50 J with an impact radius of 25 mm at an impact energy of 50J

4.3 Verification of MIDAS-C

Similar to the verification of MIDAS-M, the verification of MIDAS-C requires a validated FEM to model impact on composite targets. An experimental reference case is therefore defined in subsection 4.3.1. The comparison of the experimental results and the predictions of both the FEM and MIDAS-C is addressed in subsection 4.3.2.

4.3.1 Definition of composite reference case from literature

The validity of the composite variant of the FEM is determined based on experimental results found in literature. Lopes investigated the impact response of conventional and non-conventional layups[2]using low-velocity impact tests at impact energies ranging from 5 up to 50 J. A hemispherical tub with a diameter of 16 mm is dropped from different heights, as summarized in Table 4.4. This work only considers the Lopes' conventional laminate with a layup sequence of $[\pm 45/90/0/45/0_4/-45/0_2]_s$. The nominal ply properties of Hexply AS4/8552 are summarized in Table 4.5. The impact experiments follow the procedure as defined by ASTM standard D7136 [54] using specimens of 150x100 mm, which are centered over the support structure with a gap of 125x75mm and pinned using four rubber tip clamps at the corners.

Table 4.4: Impact energies, mass, velocities and drop weight heights.

Property		**Experiment Settings**							
Impact energy	J	5	10	15	20	25	30	40	50
Drop height	m	0.54	0.77	1.15	0.84	1.04	1.25	1.67	1.22
Impactor mass	kg	0.95	1.33	1.33	2.44	2.44	2.44	2.44	4.19

Table 4.5: Material properties of AS4/8552 carbon epoxy of Hexcel

UD Ply Properties						**UD Ply Strength**				
E_{11} GPa	E_{22} GPa	G_{12} GPa	ν_{12} -	ν_{23} -	t mm	X_t MPa	Y_c MPa	Y_t MPa	Y_c MPa	S_{12} MPa
135	9.6	5.3	0.32	0.487	0.1825	2207	1531	80.7	199.8	114.5

4.3.2 Comparison of composite FEM and MIDAS-C with literature results

The validation of the composite FEM first considers the 5J impact scenario followed by two higher impact energies. The 5J comparison provides a benchmark of the pristine contact behaviour (i.e. pristine implies without the effect of delamination and fiber breakage). The comparison impact response comparison is based on the loading phase of the impacts event. This gives an indication of the model(s) ability to reproduce an impact event.

[2]conventional layups are based on industry practices using 0^o, $\pm 45^o$ and 90^o plies in respectively 60%, 30% or 10% of the layup plies. The non-conventional layups use plies of various orientations.

The user-defined 3D damage model (VUMAT) based on Hashin's failure criterion[125] can be run with or without a deletion flag. This deletion flag has been implemented in the VUMAT to remove any failed elements. The directional stiffness of individual elements is degraded during the simulation based on fiber and matrix failure criterion, as described in subsection 4.1.1 (see p.56-57). The deletion of individual elements follows directly after fiber failure.

The impact case of 5J is compared to the FEM simulations in Figure 4.10 using (a) only the stiffness degradation and (b) element deletion with stiffness degradation. The FEM results of three different mesh sizes are shown (i.e. 0.5, 1.0 and 2.0 mm). The range of mesh sizes is based on the ability to follow the impactor shape and the required computation time. The computation time significantly increases for a decreasing mesh size (i.e. from 3 to 24 hours for a mesh sizes of respectively 2.0 and 0.5 mm). The coarsest mesh corresponds to only eight elements in the impactor diameter.

The comparison in Figure 4.10b shows that a decrease in element size results in a larger deviation from the experimental data. This trend corresponds to a larger number of deleted elements. The coarsest mesh (2.0 mm) shows the best agreement with experimental data. This effectively relates to the fact that only a small number of elements have been deleted. The deletion of elements is therefore considered detrimental for the simulation of such a low velocity impact event. The FEM simulations without element deletion show smaller differences with respect to the experimental data.

In addition to the estimations from the FEM, the impact response prediction of MIDAS-C is shown in Figure 4.10. Even though the dynamic nature of the impact experiment is not captured by the analytical model, the predictions of MIDAS-C appear to be at least equally valid as the FEM simulations. The differences between the FEM results and the predictions of MIDAS-C are more apparent for impact energies in the post-DTL region, as shown in Figure 4.11.

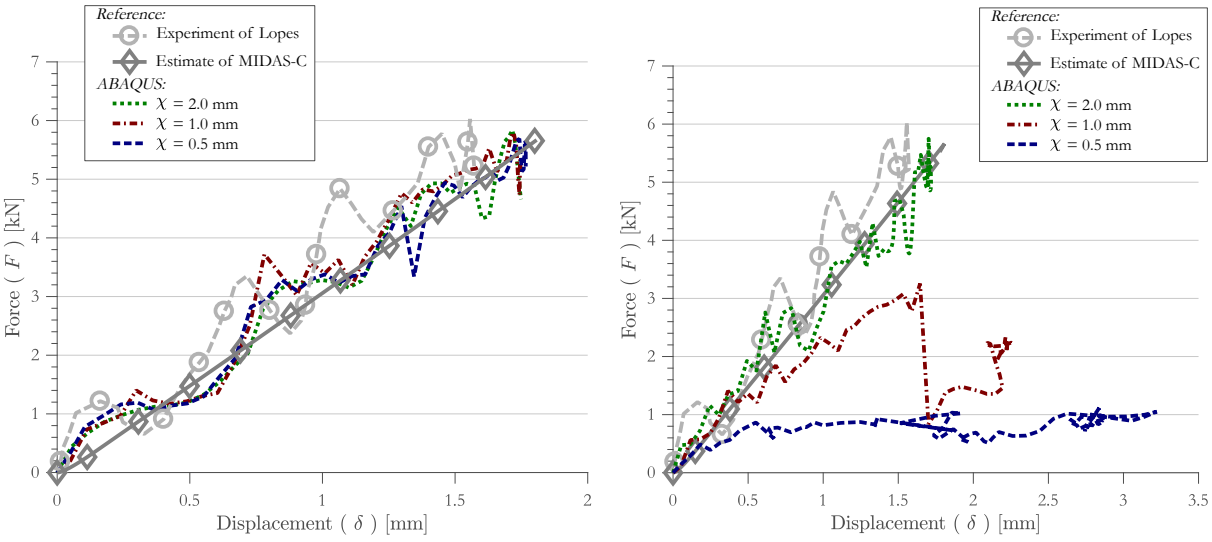

(a) Only element stiffness degradation **(b)** Element deletion and stiffness degradation

Figure 4.10: Comparison of FEM, MIDAS-C and experimental data of Lopes' for a 5J impact event

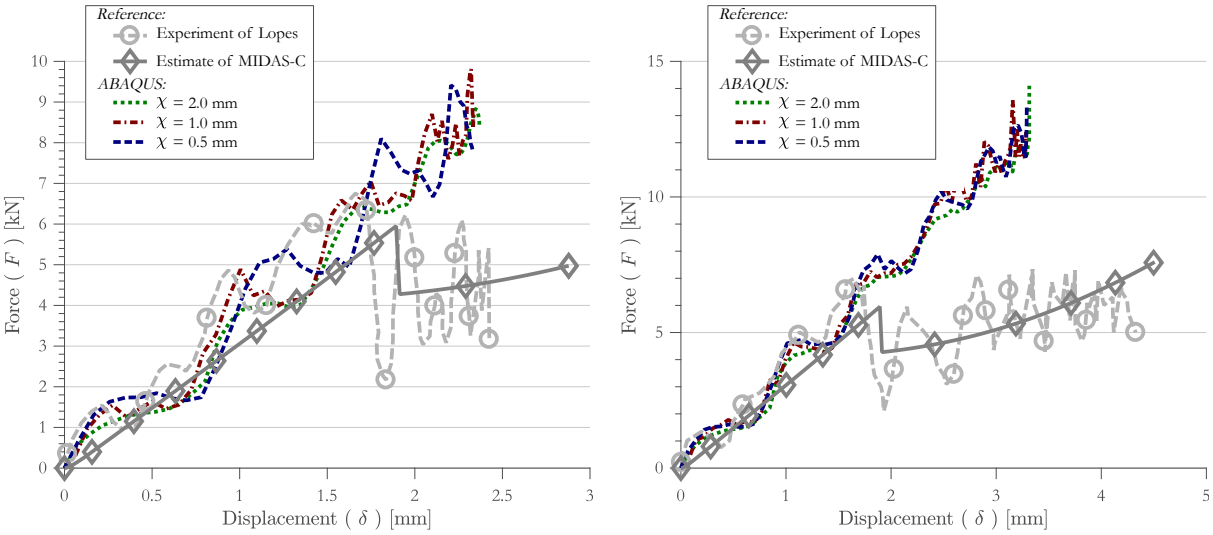

(a) Impact energy of 10J **(b)** Impact energy of 20J

Figure 4.11: Comparison of FEM, MIDAS-C and experimental data for post-DTL impact energies

The impact response after the DTL changes, which is shown by the increased oscillation amplitude and reduction of the loading slope. The pristine contact behaviour (up to DTL) of the experimental data is properly reproduced by the FEM, but the post-DTL behaviour is not captured. The initiation of delamination relates to the separation of plies, which is not explicitly modelled in the FEM. The predictions of MIDAS-C, on the other hand, are able to reproduce this change in behaviour.

The inability of the numerical model to simulate the post-DTL response limits the verification scope, while the residual deformation before and after DTL are equally important within this research. The verification of MIDAS-C is thus considered inconclusive. The initial comparison between MIDAS-C and experimental data is promising, and the next chapter therefore continues with a validation of MIDAS-C. This validation is based on low-velocity impact experiments of three different laminates.

Chapter 5

Validation

This chapter refers to the validation of the composite model described in section 3.3. The need of this validation steps is based on the inconclusive verification of the composite model. The goal of this validation is to compare MIDAS-C with experimental results. The experimental set up is described in subsection 1.4.2, followed by a description of the data acquisition. The comparison with the MIDAS-C is discussed in section 5.3

5.1 Set up of impact experiment: drop-weight test

The impact experiments, performed and set up by F.Esrail, follow the procedure as defined by ASTM standard D7136 [54], which is typically used to measure the damage resistance of a composite based on an impact event. A schematic overview of this experimental set up is shown in Figure 5.1. The specimens of 150x100mm are centered over the support structure with a gap of 125x75mm and pinned using four rubber tip clamps at the corners. A fixed impactor mass of 5.53 kg is dropped from a variable height corresponding to the required impact energy ($h = \frac{E_i}{g\, m_i}$).

The goal of this impact test series is to investigate the effect of stacking sequence on the damage resistance of carbon/epoxy laminates. The damage resistance is quantified by the type and amount of damage sustained for a given impact energy. To this extent, three different layups are impacted at four different impact energies. Each impact scenario is repeated four times. The different layups QI/OR/F are selected to represent a specific type of a laminate. For each layup, two plates are manufactured from AS4/8552 carbon epoxy of Hexcel. Consecutively, each plate is cut into eight specimens of 150x100mm. A summary of the impact experiments is shown in Table 5.1. Within this study, the experimental data is used to validate MIDAS-C.

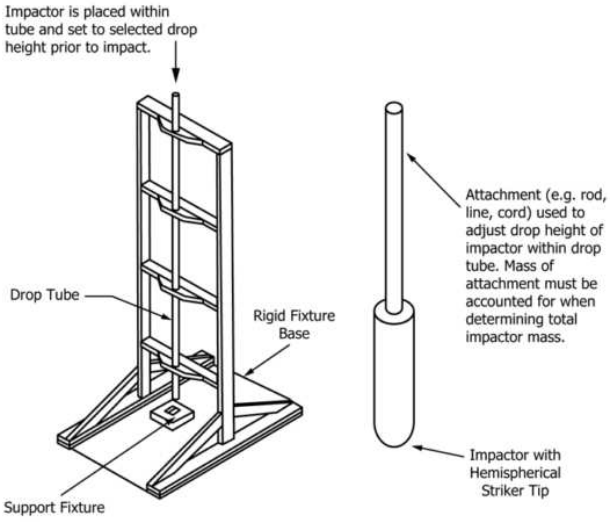

(a) Typical schematic representation of drop-weight impactor test[54]

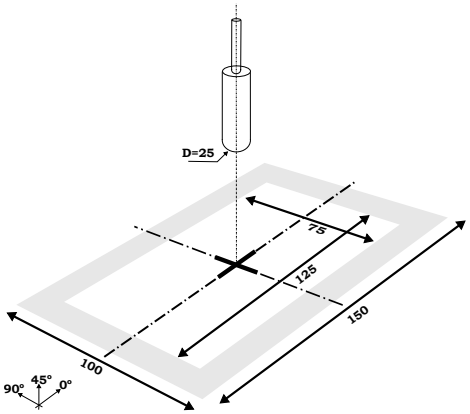

(b) Schematic illustration of test set up (in mm) [19]

Figure 5.1: Overview of drop-weight impact test set-up

Table 5.1: Impact energies, mass, velocities and drop weight heights.

Specimen Types		**Impact energy**				
ID	Layup		[J]	18.50	27.75	37.00	46.25
QI	$[45/0/-45/90]_{3s}$	Drop height	[m]	0.34	0.51	0.68	0.85
OR	$[45/0_2/-45/0_2/45/0/-45/0_2/90]_s$	Impact velocity	[m/s]	2.59	3.17	3.66	4.09
F	$[(15/-15)_5/45/-45]_s$	Impactor mass	[kg]	5.53	5.53	5.53	5.53

Table 5.2: Material properties of AS4/8552 carbon epoxy of Hexcel

UD Ply Properties					**UD Ply Strength**				
E_{11} GPa	E_{22} GPa	G_{12} GPa	ν_{12} -	t mm	X_t MPa	Y_c MPa	Y_t MPa	Y_c MPa	S_{12} MPa
131	9.2	4.8	0.3	0.1825	2068	1531	64	268	92

5.2 Data acquisition of impact series

The acquisition of data in the impact series consisted of two phases. The impact response in terms of the load history (F-t) was recorded during the impact test, while the permanent indentation was measured manually after impact. The post processing of the force response and corresponding results are discussed first, followed by a brief summary of the permanent indentation measurements.

5.2.1 Post-processing of recorded impact response

The impact drop weight is equipped with a load-cell that measures the impactor contact force history during impact. The recorded force response contains noise, and has therefore been filtered using a Savitzky-Golay filter, see Appendix A.1. An example of the recorded load history is shown in Figure 5.2a.

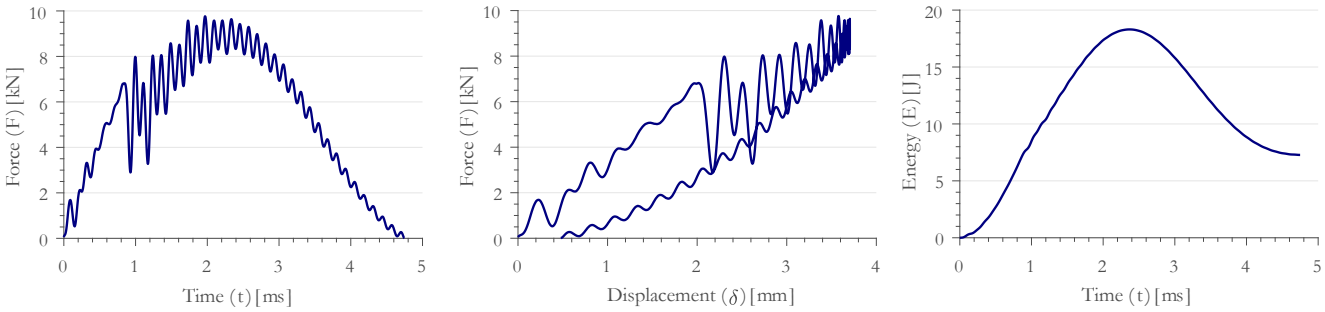

(a) Force-time **(b)** Force-displacement **(c)** Absorbed energy - Time

Figure 5.2: Impact response of QI1-1 impacted by spherical steel indentor at 18.3J

The analytical model is based on force and energy relations as function of structural deformation. Both displacement and energy absorption of the impact event are therefore required for comparison. The impactor displacement δ, velocity v, acceleration a and absorbed energy E_i are extracted from recorded force history using Equation 5.1[54],

$$\delta(t) = \delta_i + v_i\, t + \frac{g\, t^2}{2} - \int_0^t \left(\int_0^t \frac{F(t)}{m} dt \right) dt \tag{5.1a}$$

$$v(t) = v_i + g\, t - \int_0^t \frac{F(t)}{m} dt \tag{5.1b}$$

$$a(t) = g - \frac{F(t)}{m} \tag{5.1c}$$

$$E_a(t) = \frac{1}{2} m \left[v_i^2 - v(t)^2 \right] + m\, g\, \delta(t), \tag{5.1d}$$

in which $\delta_i = 0$ and $v_i = \sqrt{\frac{2E_i}{m_i}}$ refer to the impactor displacement and velocity at impact (i.e t = 0). The resulting force displacement and energy absorption over time of the given impact response are shown in Figure 5.2b and 5.2c.

5.2.2 Characteristics of impact responses

With the described post-processing steps, the impact responses of the different layup sequences can be investigated. The change in impact response as a result of increasing impact energies is shown in Figure 5.3. The impact responses of all experiments can be found Appendix A.4.

A more appropriate comparison is required based on specific impact characteristics, such as the Damage Threshold Load (DTL), peak load, max displacement and residual displacement.

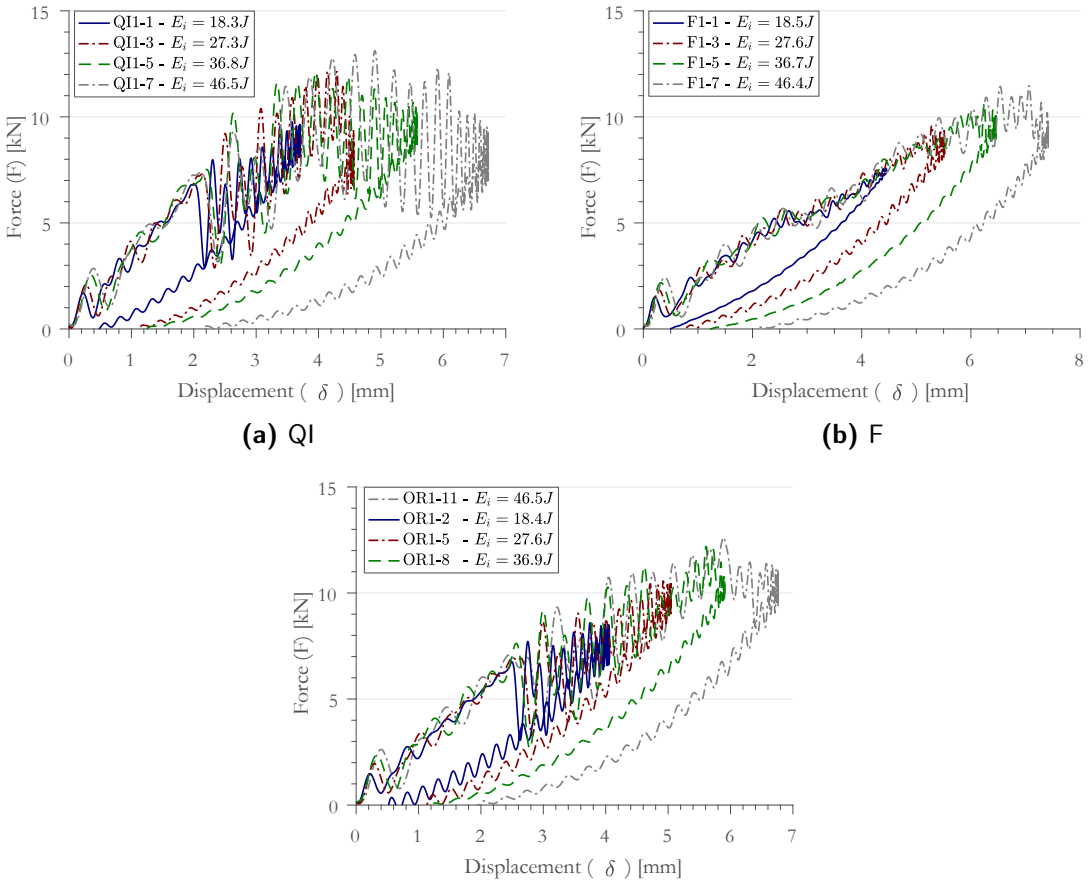

(a) QI **(b)** F

(c) OR

Figure 5.3: Variation of impact response with increasing impact energy

These characteristics are illustrated in Figure 5.4 for the different layup sequences at an impact energy of 27 J. The determination of each characteristic is described in Appendix A.2.4

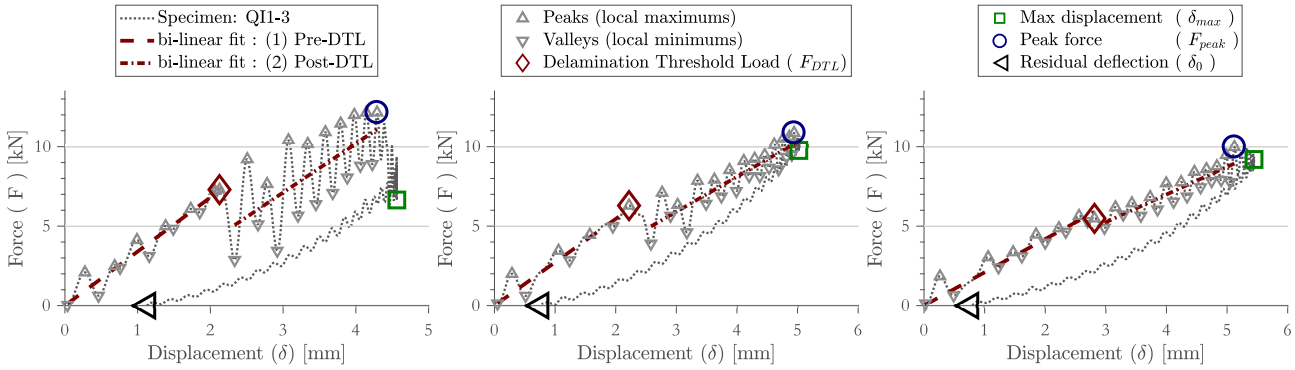

(a) QI1-3 **(b)** OR2-4 **(c)** F1-4

Figure 5.4: Impact response characteristics of QI, OR and F layups at 27.1J

Based on the definition for quasi-static indentation experiments, the DTL is obtained from the first distinct drop in the load history. The dynamic nature of impact experiments results in multiple oscillations, and a distinct load drop is therefore not explicitly apparent. Another characteristic of a DTL relates to the change in bending stiffness. This effectively changes the loading slope after DTL. This change in slope is implemented in the determination of DTL by means of a bi-linear regression fit optimization, which is described in Appendix A.2.4. In both Figure 5.3 and 5.4, a distinct load drop is apparent for both OR and QI specimens. Such a distinct drop is not clearly visible for laminate F, while the change in the impact response is (even though limited) apparent.

These differences with respect to the DTL can be attributed to the number of mismatching interfaces in the respective layups. As discussed in both subsection 1.3.3 and subsection 3.3.2, the magnitude of the load drop typically scales with the number of delaminated interfaces. These interfaces are often a consequence of bending stiffness mismatch between plies. Layup type F mainly consists of ±15 plies, which have limited difference in bending stiffness (i.e. angle difference of only 30 degrees). On the other hand, both QI and OR contain multiple interfaces with angle differences of 45 of 90 degrees.

Figure 5.5 shows the force and displacement at peak force and DTL of the impact series. The peak force has an increasing trend, while the DTLs of the respective layups are approximately constant. Moreover, layup type F has four distinct peak load regions corresponding to the four different impact energies. These four regions are, however, not as self-evident for both QI and OR layups. The lack of these distinct regions can be seen as an additional damage indicator. As is discussed in section 1.3, the initiation of fiber breakage is expected to change the impact response. The deformation increases afterIFB, while the load decreases. This occurs at an impact energy of 27.75 J for QI layups compared to impact energies of respectively 37.00 and 46.25 J for layup types OR and F,as shown in Figure 5.4a.

In addition to the lack of distinct peak load regions, Figure 5.5 illustrates that each individual case has a certain amount of scatter (i.e. the repeated experiments of any given combination of layup and impact energy do not result in identical characteristics). This scatter is illustrated on a case by case result comparison in Appendix A.4. The comparison with MIDAS-C considers

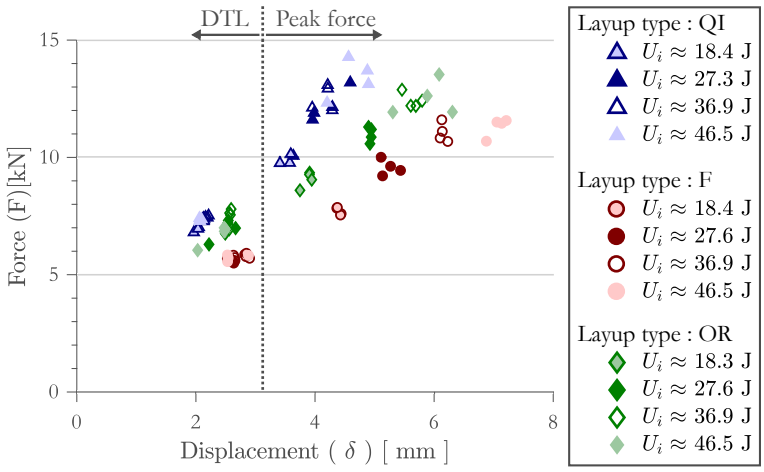

Figure 5.5: Damage initiation and peak load of impact series in terms of force displacement

the spread within impact scenarios. The DTL is compared on a layup type basis. This follows from the shared hypothesis of Schoeppner and Abrate [80], Olsson *et al.* [86] and Davies and Zhang [10] that a DTL is independent of impact energy and approximately constant for any given specimen size, material and layup sequence. The DTL results shown in Figure 5.3 and 5.5 support this hypothesis since each layup sequences appears to have a distinct DTL region that does not have any apparent variation to be correlated with impact energy.

5.2.3 Measurement of permanent indentation

The obtained displacement relation provides information of the impactor displacement over time. Even though this is equal to the deformation of the specimen during the impact event, the deformation after contact is not captured. The displacement after unloading is assumed to consist of both a residual plate deflection (δ_p) and an indentation (α_p) as illustrated by Figure 5.7. The permanent indentation damage is therefore measured separately. The permanent indentation measurements consist of both depth and width measurements.

Dent depth measurement

The permanent indentation depth measurements are performed using a dial gauge, which is attached to a support rig providing a flat reference surface. The dial gauge is calibrated using the specimen edges, which minimizes the error with respect to the residual permanent deflection. Consecutively, the support structure is moved parallel to reference edges to deepest point of the dent. The depth measurement is repeated along all four edges of each specimen to minimize measurement error. The process of calibration and depth measurement is illustrated in Figure 5.6.

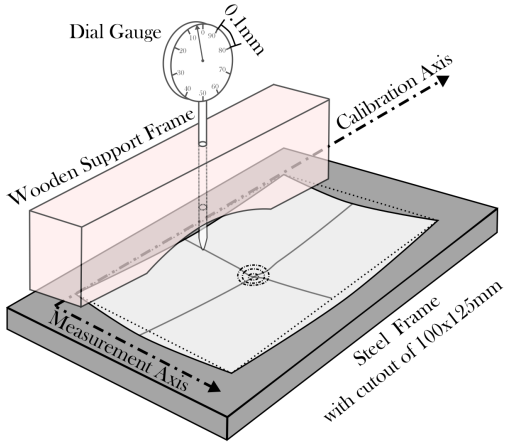

Figure 5.6: Indentation depth measurement approach using dial gauge

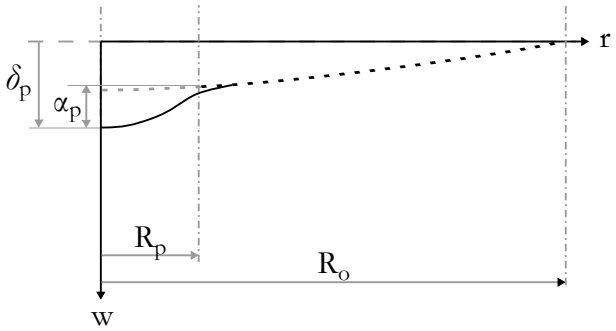

Figure 5.7: Illustration of residual deformation (δ_p) and indentation (α_p)

The indentations measured directly after impact are shown in Figure 5.8. In addition to the individual indentation measurements, a range indication per case is shown (i.e. each combination of energy and layup type). These ranges are defined by the sample mean and coefficient of variation, as given in Table 5.3.

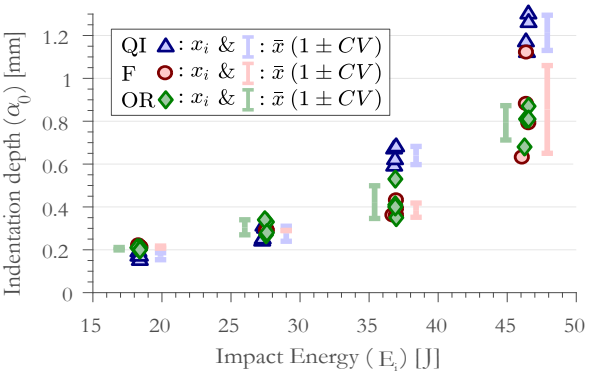

Figure 5.8: Measured permanent indentation as function of impact energy

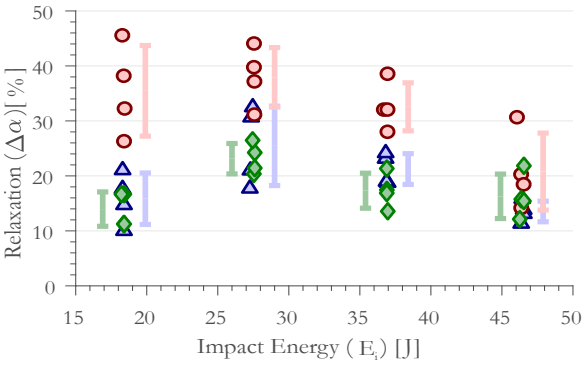

Figure 5.9: The relaxation of indentation 6 days after impact

Table 5.3: The indentation of each layup type as function of impact energy

Layup ID	Indentation Measurement			Impact Energy 18.4 J	27.5 J	36.9 J	46.4 J
F	a_0	$\bar{x}$	mm	0.21	0.29	0.39	0.86
		CV	%	*2.4*	-	*8.6*	*23.9*
	a_{6d}	$\bar{x}$	mm	0.14	0.18	0.26	0.69
		CV	%	*11.1*	*8.7*	*12.9*	*31.5*
OR	a_0	$\bar{x}$	mm	0.21	0.31	0.42	0.79
		CV	%	*2.8*	*11.5*	*18.1*	*10.1*
	a_{6d}	$\bar{x}$	mm	0.18	0.23	0.35	0.66
		CV	%	*0.8*	*8.1*	*17.3*	*6.4*
QI	a_0	$\bar{x}$	mm	0.17	0.28	0.64	1.21
		CV	%	*9.6*	*12.8*	*6.6*	*6.8*
	a_{6d}	$\bar{x}$	mm	0.14	0.20	0.50	1.05
		CV	%	*4.5*	*4.1*	*8.6*	*7.5*

The different layups have similar indentation depths at low energy impacts, while larger differences are observed at higher impact energies. Besides the difference between layups, there is considerable scatter within each independent layup. The differences between layups can be an indication of varying degree of damage resistance. Although the corresponding impact response needs to be considered to support this hypothesis. Similarly, the scatter within an impact cases needs to be investigated.

In addition to the measured indentation directly after impact, the indentation is measured again after 6 days to determine the relaxation after impact. The relaxation, $(\Delta\alpha)$ given by

$$\Delta\alpha = \frac{\alpha_0 - \alpha_6}{\alpha_0} 100\%, \tag{5.2}$$

is shown in Figure 5.9, and the sample case results are summarized in Table 5.3.

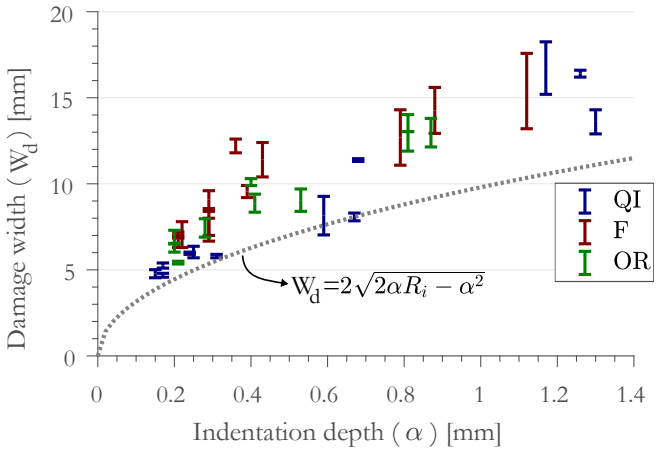

Figure 5.10: The measured dent width (min/max) versus the residual indentation depth

Dent width measurement

The damage width is measured using a caliper and is sensitive to measurement errors. This relates to the damage morphology and corresponding interpretation of the inspector, as discussed in section 1.2.3. As a generalization, a clear dent edge is not apparent and is therefore dependent on visual judgment of the inspector. The human error aspect of these width measurements can be quite significant, as is demonstrated in Appendix A.3. This limitation is acknowledged, and the width measurements of a single inspector are used. To minimize measurement errors, all specimens are measured twice in an arbitrary sequence. This decreases the bias of the initial perceived width. The measured widths are shown in Figure 5.10 besides a reference curve based on the impactor shape. This reference curve is the expected lower bound of width measurements considering both the dent geometry and dent recovery during unloading [1]. As is described in subsection 1.3.6, the dent morphology does not perfectly follow a hemispherical shape, but smoothly transitions to the reference surface. The inner radius of curvature of the dent is expected to be larger than the impactor radius due to the non-uniform recovery of the dent (i.e. the shape of the dent is not equal to the shape of impactor).

5.3 Comparison of experimental results and MIDAS-C

The validation of MIDAS-C is two fold. The first part of the validation considers the Inductive Solution, and effectively determines whether an impact event can be reproduced. The second part continues with the Deductive part of MIDAS-C. The available damage dimensions, and known reference cases allows to evaluate the deductive solution.

[1] Dent recovery and relaxation refer to separate effects. The recovery of a dent refers to the difference between the maximum dent during impact and at end of impact. Whereas the dent relaxation covers the difference over time after the impact event.

5.3.1 Validation of Inductive MIDAS-C

The inductive verification of MIDAS-C consists of two parts. The goal of the comparison is to evaluate the permanent dent estimate of MIDAS-C with the experimental data. However, similar to the verification of Model Impact Damage on Metal Aircraft Structures (MIDAS-M), described in chapter 4, the validity of loading path estimate needs to be considered. First the predicted and measured impact response are compared, and subsequently the residual indentation estimate is evaluated.

Impact response

Within MIDAS-C, its is assumed that the loading phase of an impact event can be represented by three sequential phases. The comparison presented in this section addresses the validity of this assumption, and evaluates the accuracy of the individual steps. The recorded impact response ($\cdots$) and the corresponding prediction of MIDAS-C ($\blacksquare\blacksquare\blacksquare$) are shown in Figure 5.11, 5.12 and 5.13 for respectively layup types QI, F and OR. Within this section only the highest and lowest impact energy cases are shown (i.e 18.4 J and 46.5J). The remaining cases can be found in Appendix B.4. The difference between residual deformation (δ_p) and indentation (α_0) is shown by the residual indentation markers ($\circ$ and $\bullet$) and the end of loading lines ($\cdots$).

The impact response comparison at approximately 47 J indicates that the three loading phases are indeed present in the experimental data. Moreover, MIDAS captures the transition between the individual phases for both QI and OR laminates reasonably well, but overestimates the peak force in case of layup type F. The predicted initial loading slope up to the DTL is in good agreement with the experimental results, as shown by the comparison at impact energy of 18.3 J. The difference between the individual laminates is exemplified by a comparison of predicted loading path in Figure 5.14.

The second phase of impact is characterized by an increase in oscillation amplitude and change of slope in the force displacement curves. Similarly, the estimated DTL of both QI and OR laminates fall within the experimental bounds, whereas it is overestimated by approximately 15% for laminate F (see Table 5.4). The dynamic nature of the oscillations are not captured, but the relative change in amplitude is comparable the respective load drops in MIDAS. However, the predictions of laminate F start to diverge, while the trends of QI and OR still follow the experimental results. Similarly in the third phase, the predictions of QI and OR are within the bounds of the experimental data.

Within the description of MIDAS, three different approximations of the post fiber breakage behaviour have been proposed. These approximations are evaluated in Appendix B.2. The third alternative, which combines an additional structural deflection and rapid local penetration, provides the most appropriate approximation.

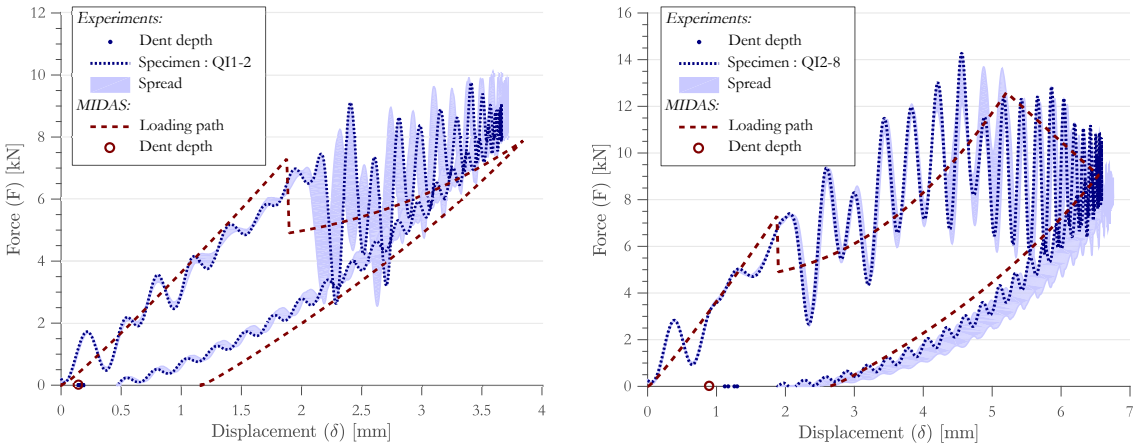

(a) Impact energy of 18J **(b)** Impact energy of 46J

Figure 5.11: Comparison of MIDAS-C with layup type QI

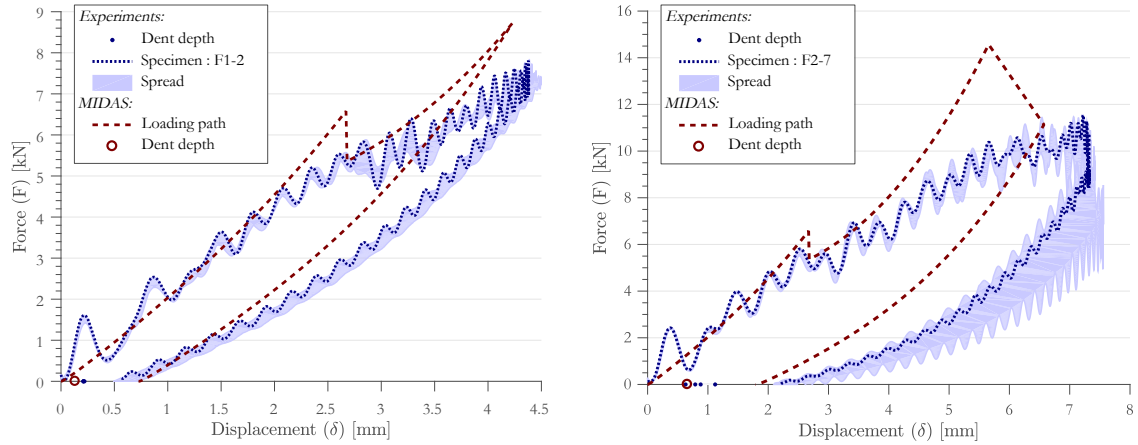

(a) Impact energy of 18J **(b)** Impact energy of 46J

Figure 5.12: Comparison of MIDAS-C with layup type F

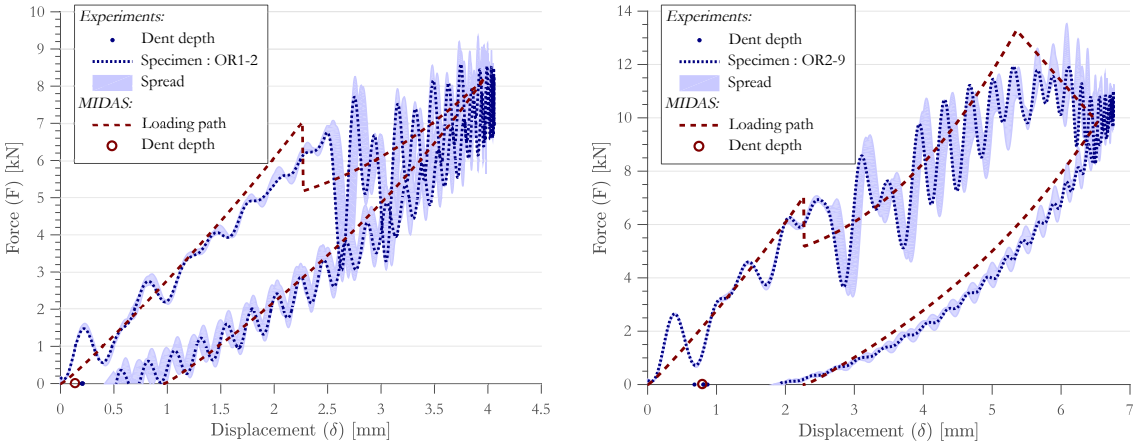

(a) Impact energy of 18J **(b)** Impact energy of 46J

Figure 5.13: Comparison of MIDAS-C with layup type OR

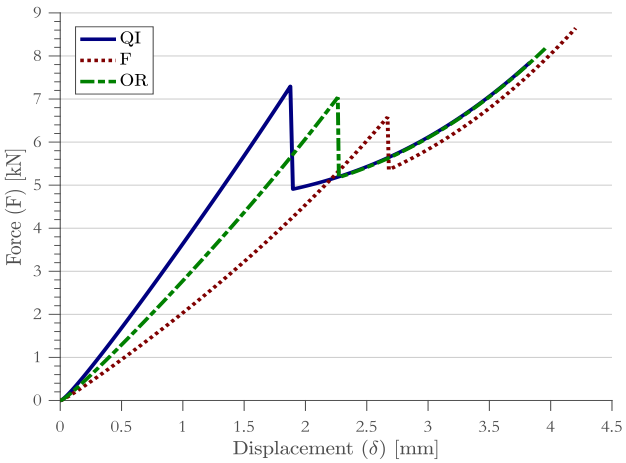

Figure 5.14: Difference in predicted loading slope of different layup types

Table 5.4: Comparison of the recorded and predicted DTL†

Layup	Experiments		MIDAS	
	μ kN	(σ) kN	$\hat{x}$ kN	$\hat{x}-\mu$ %
QI	7.3	(0.19)	7.3	0.2
F	5.7	(0.12)	6.6	15.8
OR	7.0	(0.45)	7.1	0.5

† sample mean (μ), sample standard deviation (σ) and $\hat{x}$ model estimate

Residual dent

The impact response comparison indicated that the experimental impact events shows that the impact events are reasonably reproduced. The validation of the corresponding residual dent estimates are, however, essential towards achieving the research goal MIDAS. The predicted residual dents are compared with the relaxed indentations measurements (i.e. six days after the impact event). The dent comparison is implemented in the typical knee-point diagram, which shows the increase in residual dent in terms of impact energy. The increasing slope after the initiation of fiber breakage is referred to as the knee-point. The predicted indentation and corresponding dent width are compared in Figure 5.11, 5.12 and 5.13 for respectively layup types QI, F and OR.

Based on the measured peak force and indentation described in section 5.2, the knee-point of QI laminate is expected at lower energies compared to both other layup types. This trend is indeed present in the predictions of MIDAS. The pre-IFB indentation predictions are only underestimated for the QI laminates, while the accuracy of the post-IFB predictions varies. The QI and OR indentations are respectively under and over estimated. The mean indentation of laminate F is reproduced, but the experimental results have a noticeable scatter. The permanent dent radius predictions contain larger differences. This deviation is expected based on the measurement scatter reported in Appendix A.3. The dent radius appears to be consistently underestimated, although it is slightly over estimated in two cases for the QI laminates.

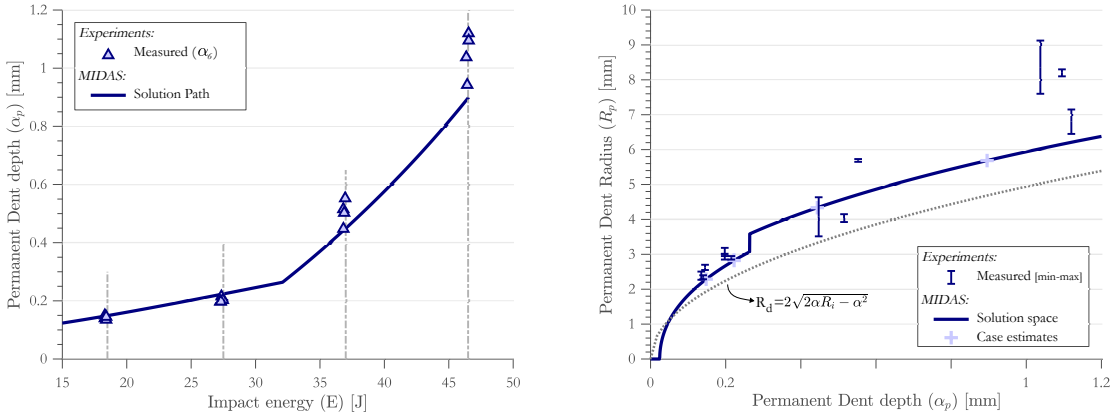

(a) Permanent indentation as function of energy **(b)** Dent radius as function of dent depth

Figure 5.15: Comparison of dent estimates with relaxed dent of lay up type QI

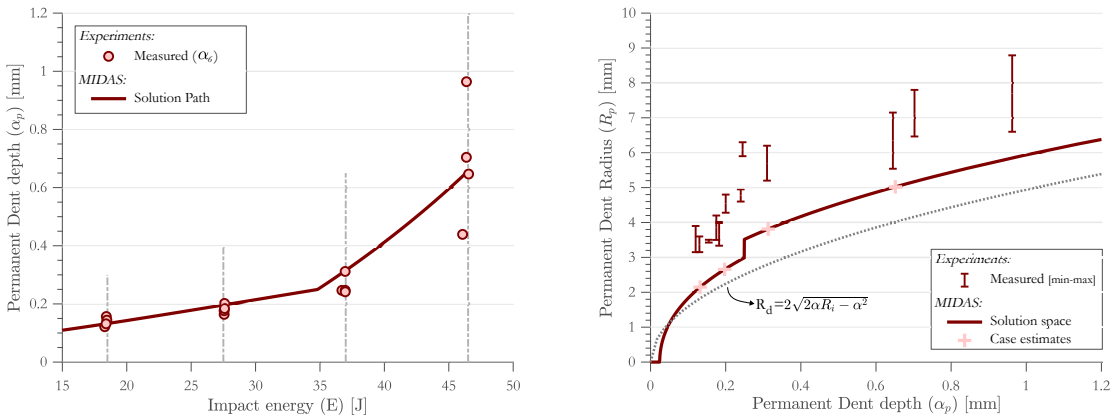

(a) Permanent indentation as function of energy **(b)** Dent radius as function of dent depth

Figure 5.16: Comparison of dent estimates with relaxed dent of lay up type F

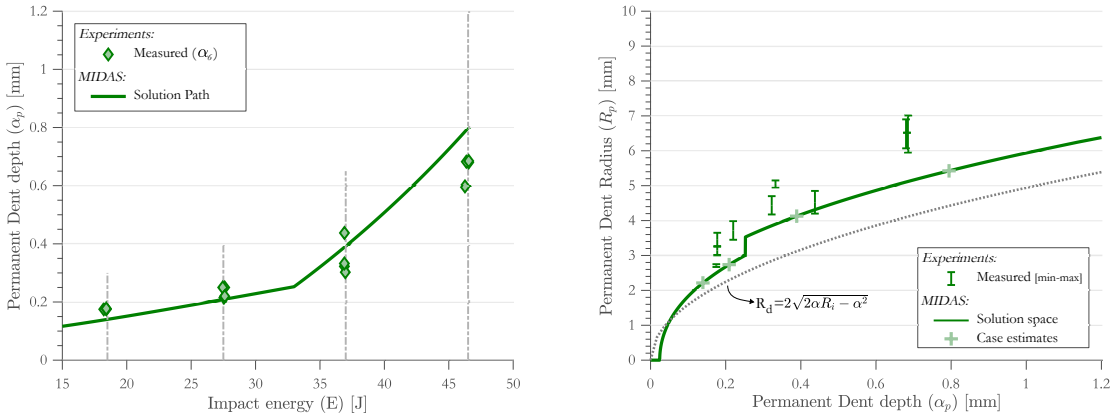

(a) Permanent indentation as function of energy **(b)** Dent radius as function of dent depth

Figure 5.17: Comparison of dent estimates with relaxed dent of lay up type OR

5.3.2 Validation of Deductive MIDAS-C

The validation of the inductive solution showed that the experimental impact events are reasonably reproduced. The force-displacement trends are captured, while the knee-point diagrams correspond in varying degrees. An alternative measure of the validity of MIDAS-C is based on the deductive solution, in which the experimental cases are estimated based on the residual dent measurements. This validation step is again performed in two steps. In the initial step, the impactor radius is known and only the impact energy needs to be determined. In the second step, both the impact radius and impact energy are assumed to be unknown. This corresponds to more realistic application, in which only dent measurements are reported.

Prediction of impact energy based on known impactor radius

The first step of the deductive solution continues with the reported knee-point diagrams. The indentation measurements are interpolated in the knee-point diagram, which provides the resulting energy estimates. In Figure 5.18, the predicted impact energies and the relative prediction errors are shown as function of the experimental energy. The relative prediction error is defined as

$$\Delta x_i = \frac{x_i - \mu}{\mu} \cdot 100\% \tag{5.3}$$

in which x_i and μ refers to respectively the predicted and target values. Within this section, the x_i and μ terms correspond to impact energy. In the next section, the same relation is used to for both the impactor radius and impact energy. The resulting predictions are inline with the residual indentation comparison of the inductive validation. Within the post-IFB region, prediction error of all layup types is within 10%. The prediction error pre-IFB varies with the different layup types. The QI estimates remain consistently within 10%, while difference as large as 20% and 30% are observed for F and OR laminates. These differences could be expected by considering the respective knee-point diagrams (i.e Figure 5.16a and 5.17a. The indentation depth was consistently under estimated for OR layup, while the pre-IFB slope is slightly overestimated for F laminates. An alternative deductive solution using the

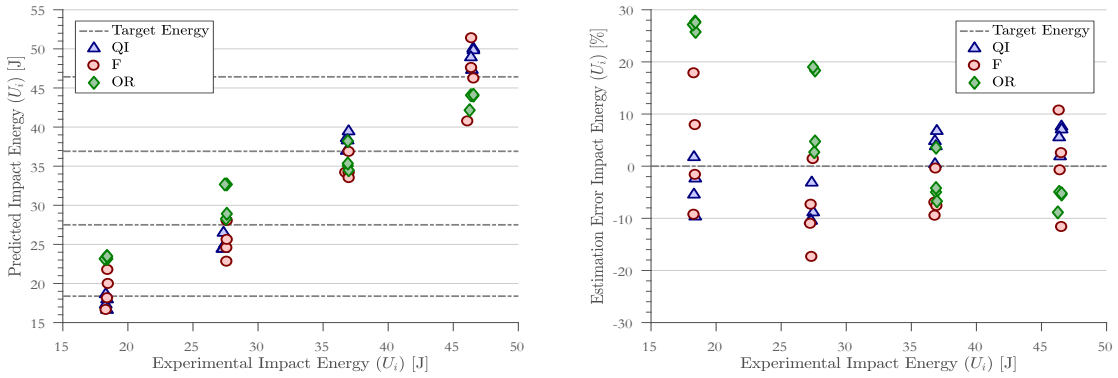

(a) Estimated impact energy **(b)** Estimation error

Figure 5.18: Estimated impact energy given a known impactor radius as function of experimental impact energy

known impactor radius continues with the measured dent radii. The predicted results deviate significantly from the target cases, as reported in Appendix B.3. The estimation driven by the residual indentation depth is therefor preferred.

Prediction of impact threat

The second step in the deductive validation requires an additional processing step to predict the impact threat. This processing step is referred to as the creation of the damage contour map, in which the damage dimensions (α_p and R_p) are mapped out as function of impactor radius and impact energy. This map is obtained by solving the inductive solution of MIDAS for a range of impactor radii. The individual impactor radii solutions cover the allowable impact energy range (i.e. up to penetration). The contour map of individual laminates is divided in two segments: before and after the initiation of fiber breakage. The discontinuity in the α_p-R_p curves requires this graphical separation.

The resulting contour maps are shown in Figure 5.20. The individual impactor radii are indicated by the - - - lines, while several reference energy levels are superimposed using ━ lines. The measured damage data is included in the damage contour maps. The range between the min-max dent radius is indicated by |—| . The intended target solution is highlighted by different markers. The △, ○ and ◇ refer to respectively layup type QI, F and OR. Each of the target solutions is encircled by two ellipses, which represent measurement errors of 10% or 25%. an The resulting contour maps provide an indication of the accuracy of MIDAS. For example, the target and measured damages are in relatively close proximity in the case of QI laminates compared to the differences of both F and OR layups.

The estimated impact threats corresponding to the measured damage properties are extracted from the contour map. The results are presented in two figures. Figure 5.19a shows the prediction with respect to the target cases, while the relative estimation error is shown in Figure 5.19b Different marker types and color combinations are used to indicate respectively the lay up type and target case. The △, ○ and ◇ refer to layup types QI, F and OR. The min-max measured dent radii are treated as individual data entries, and the resulting threat map shown in Figure 5.19a therefor does not not explicitly differentiate between the minimum and maximum threat estimates.

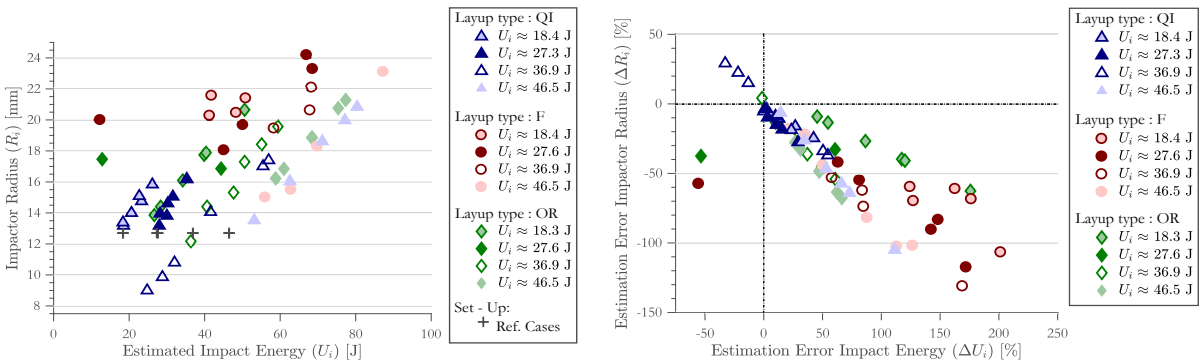

(a) Estimated impact threat **(b)** Estimation error

Figure 5.19: Comparison of estimated impact threat with respect to experimental data

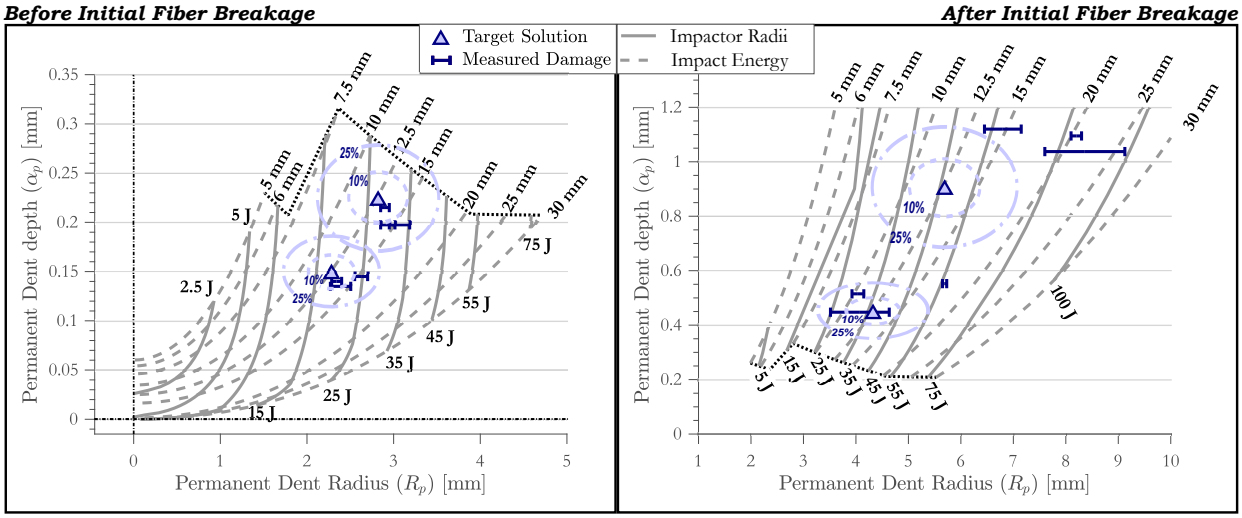

(a) Damage contour map of layup type QI

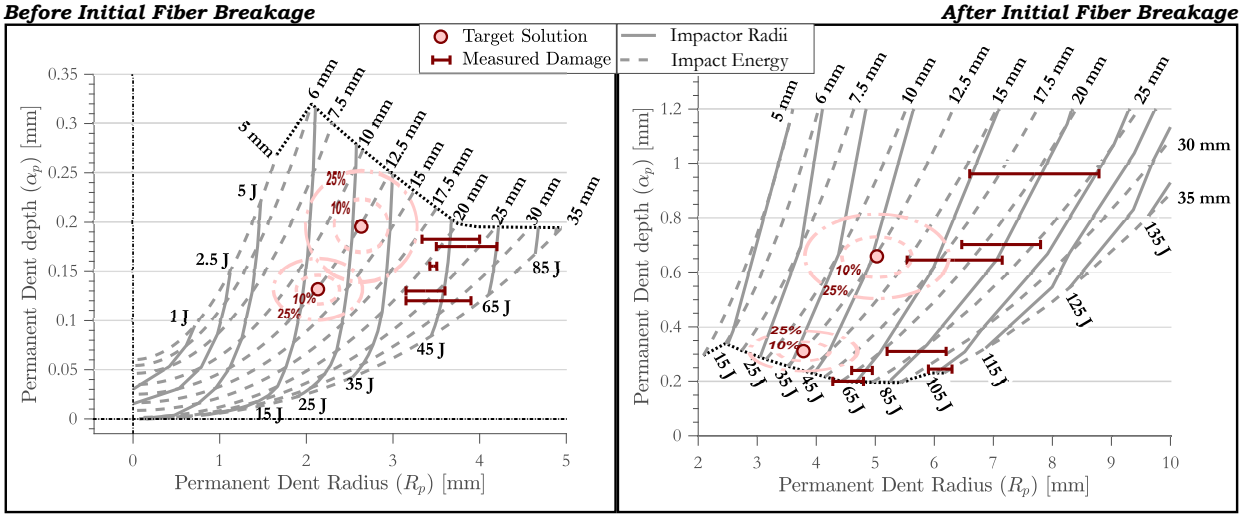

(b) Damage contour map of layup type F

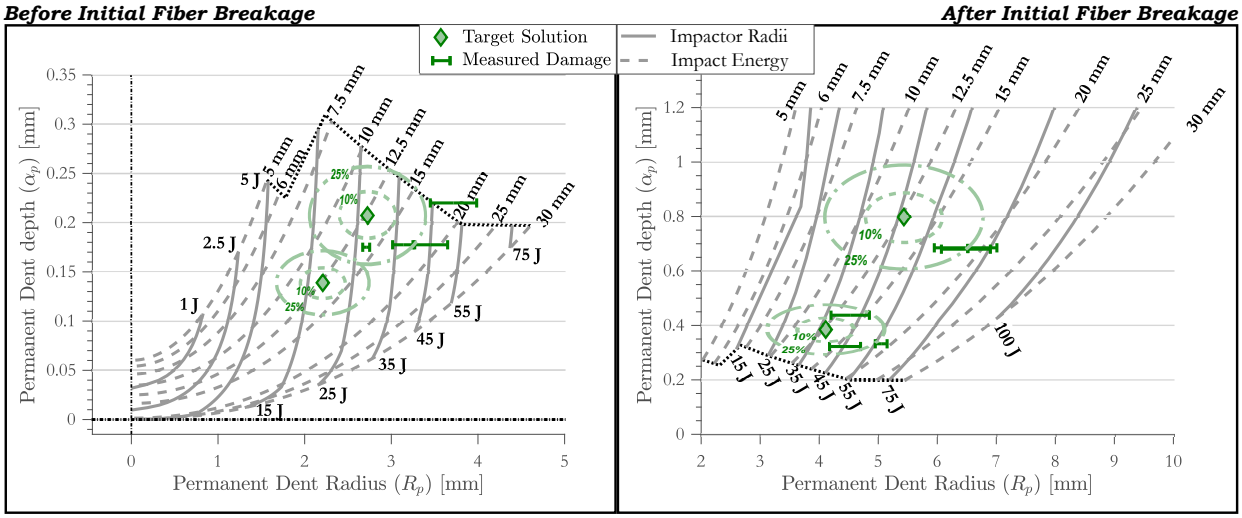

(c) Damage contour map of layup type OR

Figure 5.20: The expected damage dimension as function of both impact energy and impactor size

Chapter 6

Application

Based on the verification of MIDAS-M and the validation of MIDAS-C, a practical application of MIDAS is considered. The case study is based on structural damage data from a major European carrier. The case study is developed in collaboration with V.S.V. Dhanisetty. The indentation damages found on a Boeing 777 fleet are implemented in MIDAS-M to deduce to the impact threats. These threats are subsequently analyzed using MIDAS-C for a composite target structure. The resulting damage predictions provide an estimate of impact damages for the next-generation aircraft fleet, such as Boeing 787 or the Airbus A350. This chapter first addresses the differences in residual deformations in composite and metal structures, before the case study step up, and subsequently conversion process with MIDAS is described.

6.1 Interpretation of the residual deformations

The conversion process originates from an industry need to address impact damage on composite structures based on the experience with metals. An important aspect of this conversion is the interpretation of maintenance personnel. For example, Haase and Mikulik [26] indicates that maintenance personnel could wrongfully interpret impact incidents on composite structures as minor due to their experience with metal structures. Resulting in the (possibly wrong) assumption that no significant damage is generated. This misinterpretation actually relates to the perception of the residual deformations.

In chapter 3, two different approaches are described to model impact (MIDAS) on metal (-M) and composite (-C) targets. The respective approaches are required to obtain the material dependent (different) residual deformations. The differences in terms of the assumed deformation shape during loading is discussed in subsection 3.1.3. MIDAS-M implements a transition region between the local and global deformation modes based on penetration limits, while the composite variant focuses on the subsurface damage types using only the local and global deformation modes. Similarly, the residual deformations (after an impact event) differ for both material types, which is illustrated in Figure 6.1.

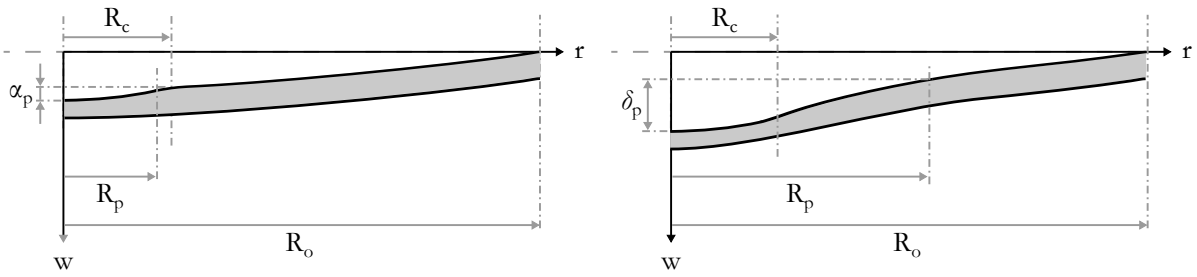

(a) Composite target (MIDAS-C) **(b)** Metal target (MIDAS-M)

Figure 6.1: Differences in residual deformation shapes in MIDAS

In both models, the residual deformation shape consists of a global and local deformation part, but the deformation perceived by personnel is assumed to consist of only the local deformation. This includes the transition region in case of MIDAS-M. The residual deformation radius (R_p) in metal targets is therefore larger than the contact radius (R_c), while it is smaller in the case of composite targets. The residual deformation depth is defined by the height difference between center of contact and the residual deformation radius, and therefore differs for both material types. In composite targets, the residual deformation depth is typically referred to as the residual indentation (α_p) and can be seen as a local reduction of thickness. In metal targets, on the other hand, the residual deformation is referred to as the dent depth (δ_p), which includes an additional deformation component besides the reduction of thickness. This could result in dent depths several times the plate thickness. The composite damage sizes obtained in the conversion process, which is described in section 6.3, are therefore expected to be smaller than the originally measured metal dimensions. The residual deformation definitions are based on the assumed perception of maintenance personnel, and highlight the underlying cause of the interpretation bias addressed by Haase and Mikulik [26] or similarly by Cook *et al.* [1].

6.2 Case study set up

The case study set up considers two aspect of the practical scenario. The first part addresses the appropriate target plate dimensions based on fuselage designs of wide-body aircraft, while the second part discusses the implementation of the maintenance data set.

6.2.1 Definition of appropriate target plates

The case study is intended to apply the research objective by using damages found on Boeing 777 to predict impact damage on Boeing 787. The target plates have to represent respective aircraft's fuselage structures. The case study's target plates are based on the work of Haase and Mikulik (CODAMEIN)[26], in which fuselage dimensions of both Boeing 777 and 787 are summarized and a representative (composite) aircraft structure is defined. The layup sequence for this fuselage section is $[(0/90)/0/45/90/-45/0/45/90/-45]_s$. The top layer (indicated by (0/90)) is a fabric ply with a thickness of 0.25 mm, while the remaining layers are unidirectional plies with thicknesses of 0.15 mm. Unfortunately, the required composite material properties are not specified by Haase and Mikulik. The composite material used in the

Table 6.1: Range of wide-body aircraft fuselage dimensions [26]

Aircraft	Dimensions		
	$a_{stringer}$ mm	b_{frame} mm	t_{skin} mm
B777	230	530	1.0-2.6
B787	227	610	~

Table 6.2: Material properties of Al2524 [126, 127]

Elasto-Plastic (EP)		
σ_y MPa	σ_u MPa	ε_f %
275.8	413.7	21

Table 6.3: Material properties of AS4/8552 carbon epoxy of Hexcel with assumed ply thickness

UD Ply Properties					UD Ply Strength				
E_{11} GPa	E_{22} GPa	G_{12} GPa	ν_{12} -	t mm	X_t MPa	Y_c MPa	Y_t MPa	Y_c MPa	S_{12} MPa
131	9.2	4.8	0.3	0.15	2068	1531	64	268	92

validation chapter is therefore assumed applicable for the composite target plate. The range of fuselage dimensions and the relevant material properties are summarized in Table 6.1—6.3.

A proper comparison of the Boeing 777 and 787 impact damages requires that the respective plate definitions have similar design criteria. This implies that both target plates should fail under the same applied edge loads N_i. The following five loading conditions are considered covering both in-plane strength and buckling behavior: uni-axial tension (ut), uni-axial compression (uc), pure shear (s), bi-axial tension (bt) and bi-axial compression (bc). The bi-axial tension requirement is based on the simplification that a fuselage can be considered a pressure vessel. The circumferential stress is therefore assumed twice the longitudinal stress (i.e. $\sigma_{xx} = \frac{1}{2}\sigma_{yy}$). The applied loads are assumed equal in the bi-axial compression case.

The composite reference plate is completely defined by (i) the indicated layup sequence, (ii) the material properties and (iii) the frame and stringer pitch specified in respectively Table 6.3 and 6.1. The failure loads of the composite plate are therefore used to determine a set of metal plate thicknesses, which are summarized in Table 6.4. These metal thicknesses fail at the respective composite failure edge loads. The procedure and the required design equations are reported in Appendix C. The resulting target plates are summarized in Table 6.5 and 6.6. The range of fuselage dimensions in Table 6.1 limited the feasible design space, while the edge failure load for buckling due to bi-axial compression defined the required metal plate thickness[1].

[1]The shear buckling load of the metal plate is lower than the composite alternative. However, equal shear failure would require a thickness outside the indicated design space (i.e. 2.9 mm > [1.0-2.6 mm])

Table 6.4: Failure loads of the composite plate and corresponding required metal plate thickness

Variable		In-plane					Buckling				
		ut	*uc*	*bt*	*bc*	*s*	*ut*	*uc*	*bt*	*bc*	*s*
N_i	kN/m	453.4	443.6	404.6	573.6	242.9	~	296.6	~	337.6	756.6
t_i	mm	1.59	1.56	1.22	2.01	1.47	~	2.52	~	2.45	4.23

Table 6.5: Design of target plates used in case study[†]

Material	Dimensions			Elastic Properties		
	a mm	**b** mm	**t** mm	**Ex** GPa	**Ey** GPa	**D** Nm
Composite	227	610	2.9	54.1	54.1	121.6
Metal	230	530	2.52	70	70	102.6

[†] the procedure to determine the elastic properties is summarized in Appendix D

Table 6.6: Failure loads of target plates used in case study

Material	In-plane Failure					Buckling Failure		
	N_{ut} kN/m	N_{uc} kN/m	N_{bt} kN/m	N_{bc} kN/m	N_s kN/m	N_{uc} kN/m	N_{bc} kN/m	N_s kN/m
Composite	453.4	443.6	404.6	573.6	242.9	33.8	29.6	756.6
Metal	718.2	718.2	829.3	718.2	414.7	36.8	29.6	159.7

6.2.2 Maintenance data

The case study is based on structural damage data of a Boeing 777 fleet from a major European carrier. The data covered a fleet of 75 aircraft in timespane from 2005 to 2015. The preparation and processing of the maintenance data is performed by V.S.V. Dhanisetty in line with the assumptions of MIDAS. The damage type is typically reported in a qualitative manner (e.g. referred to as dent, lighting strike, hole, etc). The appropriate damage types for this case study consist of only (i) dents or (ii) dents with scratches. Depending on the fuselage section, this corresponds to approximately 60-90% of the impact related damages. The quantitative data, on the other hand, specifies the dimensions of the dent in terms of length, width and/or depth. The implementation of MIDAS requires that the dent's dimensions are fully specified, and lack of any single parameter causes a particular data entry to be classified incomplete. An initial group of 479 verified dent descriptions is reduced to a sample set of 120. This sample set is used to estimate impact threat characteristics (i.e. the impactor radius and impact energy).

Within MIDAS, dents are assumed perfectly circular. The maintenance records, however, consists of elliptically shaped damages. The eccentricities of these damage entries are com-

pensated to an equivalent circular entry. The compensation is based on an equal damage area of the equivalent circular and reported elliptical dents. The approximated circular dent radius (R_p^*) is determined in Equation 6.1 using the semi minor and major axis of the ellipse (R_a and R_b). The generic circular approximation is justified by the distribution of the major/minor axis ratio, as summarized in Table 6.7. The distribution of measured dent depth and radius is shown in Figure 6.2 by means of an histogram and a fitted distribution. Four different distribution types have been tested in line with the the works of Chen *et al.* [2]: Weibull, log-logistic, lognormal, and normal. The goodness of fit comparison is performed by Chi-squared test to to determine an appropriate distribution. The procedure and results are summarized in Appendix C.2.

$$\pi R_a R_b = A_{ellipse} = \pi {R_p}^{*2} \tag{6.1a}$$

$${R_p}^* = \sqrt{R_a R_b} \tag{6.1b}$$

Table 6.7: Statistical distribution of measure of circularity of reported dent damages in terms of the ratio of major over minor axis (R_b/R_a)

Major/minor axis ratio				
mean	**median**	**mode**	**min**	**max**[†]
1.43	1.06	1.43	1.00	8.00

[†] significantly larger, than second highest ratio of 2.67

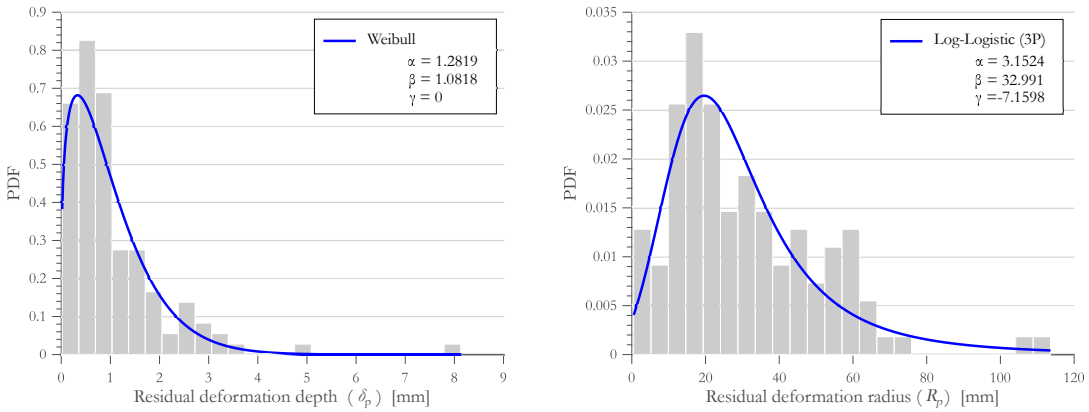

(a) Distribution of measured deformation depth **(b)** Distribution of measured deformation radius

Figure 6.2: Histograms of measured damage dimensions with distribution fit (see Appendix C.2)

6.3 Application of MIDAS

The described impact damages are implemented in MIDAS resulting in a deductive conversion from dents to threats and subsequently an inductive solution of composite dents. The estimated impact threats are compared with damage limits of both composites and metals.

6.3.1 Deductive procedure of MIDAS-M

In line with the deductive procedure described in subsection 5.3.2, a damage contour map is obtained for impacts on the metal target plate. The damage dimensions (δ_p and R_p) are mapped out as function of impactor radius and impact energy. This map is obtained by solving the inductive solution of MIDAS-M for a range of impactor radii. The resulting damage contour map is shown in Figure 6.3. The individual impactor radii are indicated by the ▪ ▪ ▪ lines, while several reference energy levels are superimposed using ▬ lines. The measured damage data is superimposed on the map to indicate damages of fuselage section A (■), B (◆), and C (●). In addition to the damage data and the predicted impact characteristics, a shaded grey area is added. This area corresponds to the repair limits typically found in Structural Repair Manual (SRM), as reported by Chen *et al.* [2]. Damages within this shaded area are defined as low consequence impacts, because they require temporary repairs within a specific time frame. Direct permanent repairs are required for damages outside these limits, and are therefore classified as high consequence impacts.

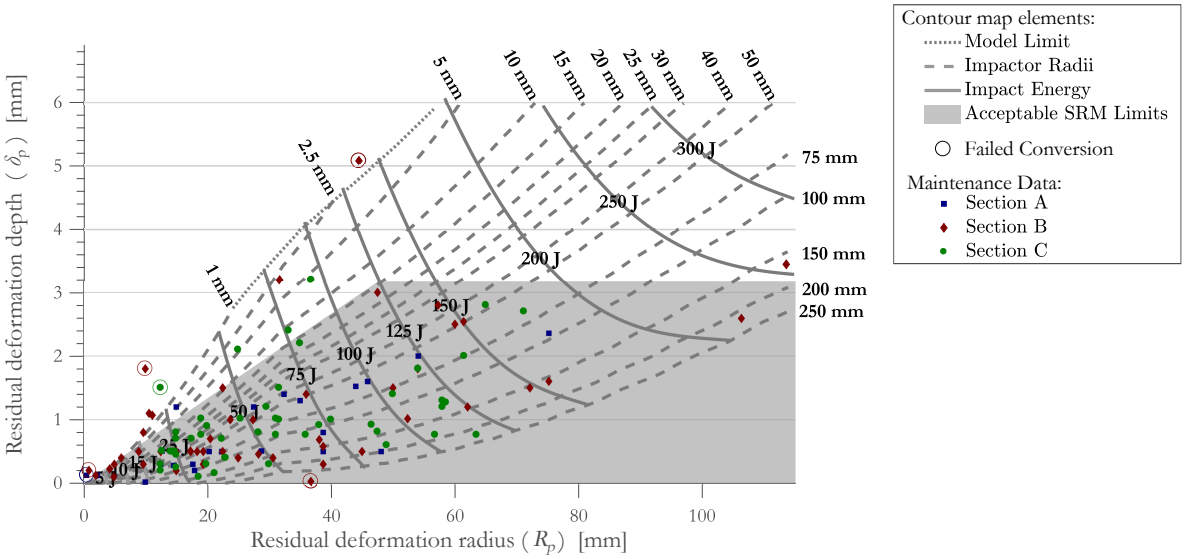

Figure 6.3: Damage contour map of MIDAS-M with maintenance damage

Besides the low- and high-consequence impact threats, there are seven data points that are significantly beyond the limits (highlighted with a ○). The damage entry of approximately 5mm deep and 45 mm wide falls in the region where penetration is expected to occur. A rough estimate would place the impact threat radius (R_i) between 2.5-5.0 mm and an energy of approximately 130J. On the other hand, the damage entry with a permanent radius (R_p) of approximately 40mm does not have a significant indentation depth, which would result in impactor radius larger than the plate size. The largest outlier of Section A has a residual deformation depth and radius of approximately 8.0 mm, and is not shown in the contour map. The remaining four data entries have at relatively deep dents compared to the dent width, and are all located to the left of the estimate of the 1mm impactor radius. The deductive solution procedure is therefore unable to converge on an appropriate solution for these seven scenarios. Besides these seven outliers, there are eight entries that are located on or just outside the contour map limits. MIDAS, however, converged to a solution within 10% of the recorded

damages, and they are therefore included in the conversion process. These entries have an estimated impactor radius of 1mm and impact energy ranging from 1-25J.

The estimated impact threats corresponding to the measured damages are extracted from the contour map, and the distribution of the expected impactor radius and impact energy are shown in Figure 6.2. A goodness of fit comparison is performed by Chi-squared, similar to the aforementioned damage distributions, and the distribution fitting is summarized in Appendix C.2. Figure 6.4a shows two impactor radius distributions. The first fit (▬) includes all converted entries, while the second fit (▪ ▪ ▪) excludes the eight outliers of 1mm, which are located on the limits of the contour map.

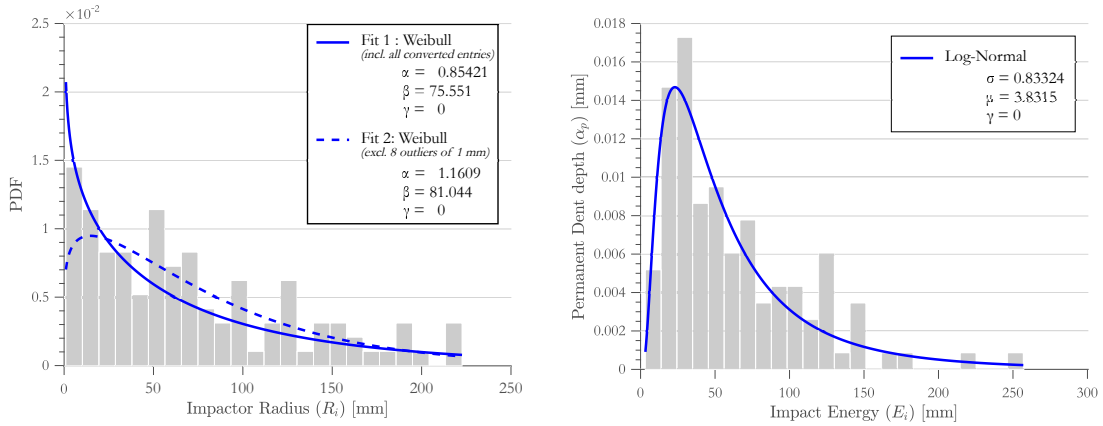

(a) Distribution of estimated impactor radius **(b)** Distribution of estimated impact energy

Figure 6.4: Histograms of measured damage dimensions with distribution fit (see Appendix C.2)

6.3.2 Inductive procedure of MIDAS-C

The second step of the conversion process refers to the deduction of damage on the composite plates. As a graphical representation, the results are summarized on an equivalent composite damage contour map shown in Figure 6.5. This map consists of two parts in line with the initial fiber breakage limit described in subsection 5.3.2. The resulting maps show that the majority of the threats result in a dent below the IFB limit, whereas only four cases are shown within the advanced fiber breakages stage. However, 18 entries are not included in the contour map illustration. These threats are expected to cause complete penetration. The conversion process is summarized in Table 6.8. These results are discussed in next section.

Table 6.8: Summary of sample data set conversion

Data Set		Metal			Composite			
Section ID	Sample size	# failed conversions	# low consequence	# high consequence	# No dent	# Residual dent	# IFB dent	# penetrations
A	23	2	20	1	7	12	0	2
B	47	4	34	9	9	20	2	12
C	50	1	46	3	12	29	2	6

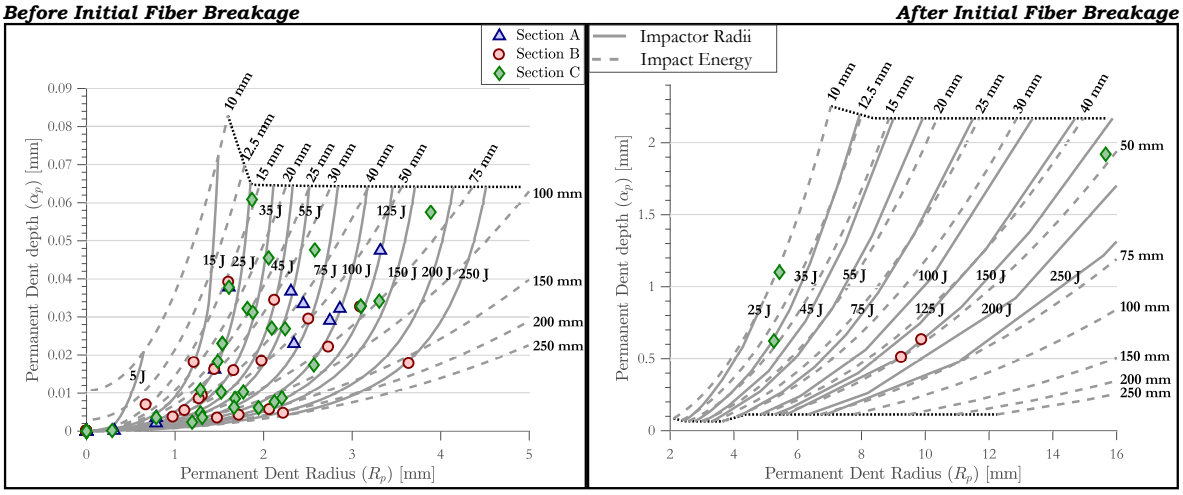

Figure 6.5: Damage contour map of MIDAS-C with predicted threats from MIDAS-M

6.3.3 Impact threat comparison

The distributions of damage for the metal and composite cases are shown in the respective damage maps. These provide a direct comparison of the measured and expected damages. Another visualization method converts the damage maps into threat maps. As described in the description of the metal contour, the distinction between low, and high consequence impact damage determines the required maintenance steps. These limits are superimposed on the threat map to provide a direct estimate of high or low consequence impact events. The resulting threat map of the data set is shown in Figure 6.6. The metal SRM limits are superimposed with a black line, while three different benchmarks are added in grey for the composite case. The stages refer to complete penetration (—), initiation of fiber breakage (- - -) and the threshold level for residual dents (-·-). Impacts threats below this last thresholds do not cause any residual indentation.

Comparison of both limits indicate that part of the low consequence impacts in metal will result in penetration of the composite plate (i.e. region between the gray — and black — line). On the other hand, the lower composite limit (-·-) indicates that a range of large impactors will not cause any residual indentation in the composite plate, while they do in metal plates. The summary of the conversion process in Table 6.8 highlights the increase in high consequence impact by moving from metals to composites. Although some aspects of the conversion process need to be investigated to evaluate the applicability, which is discussed in the next section.

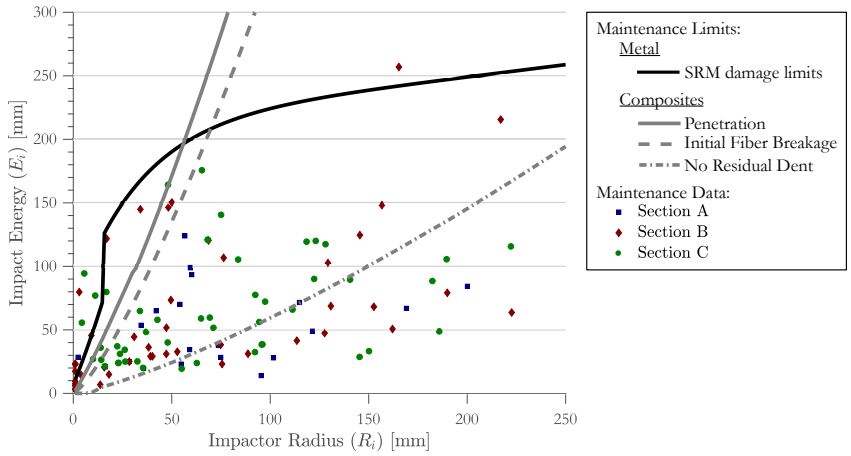

Figure 6.6: Impact threat estimates with respect to metal and composite maintenance limits

6.4 Discussion of the conversion process

The described conversion process provides a relevant and interesting comparison of impact threats to composite and metal structures. However, several aspects of the conversion need to be underlined the place the practicality of the conversion in perspective.

(I) Small mass impact threats

The impact threat distribution shown in Figure 6.4 indicates that a large portion of threats consist of impactor radii smaller than 10 mm. Within MIDAS all impact events are assumed quasi static and boundary independent events. However, as indicated by Olsson [87] small mass impact can be considered boundary dependent dynamic events.

(II) Plate boundaries

The plate definitions only consider a single frame and stringer pitch. The reference damage are in close proximity of the plate boundaries in some of the metal cases, while the plate boundaries are assumed simply supported. Similarly, the relatively large deflections occur within the solution procedure. The displacement of boundaries is not considered, and could be appropriate.

(III) Lack of delamination due to membrane dominating behaviour

The impact process of the composite damages is primarily driven by the membrane effects at large displacement, and only a limited bending force contribution is accounted for. As a result, the delamination threshold load is not reached.

(IV) Point load approximation of indentation

The upper limit of impactor radii used in the metal conversion considers impactor twice the size of the stringer pitch (i.e. impactor radii equal or larger than the stringer pitch). The impact behaviour is approximated by a local and global behaviour, in which the impact event is considered a point load. However, the validity of a point load needs to be evaluated for such large impactor radii.

These aspects are inherently part of MIDAS, and the validity of the corresponding assumptions will be discussed in the discussion chapter.

6.5 The way ahead: from Dents to Dollars

The described application of MIDAS allows a direct comparison of the impact threats to metal and composite structures. The standalone application of MIDAS results in a conversion of measured dents to predicted dents in respectively metal and composites structures. The promising potential of this conversion, however, focuses on the cost benefits of relevant impact threat predictions. This potential is investigated in a paper co-authored by V.S.V. Dhanisetty: *Predicting impact threats for aircraft structural damage risk assessment.* A key take away of this paper is that MROs can reduce annual maintenance cost and increase up-time of aircraft by means of successful mitigation of impact risks. The procedure to evaluate the risk of a particular impact threat follows the 5-step Safety Risk Management Process established by International Civil Aviation Organization (ICAO) [129]: hazard identification, hazard probability, hazard consequence, risk assessment, risk control/mitigation. However, in the current situation, both the identification and the probability of hazards are considered separately from the actual consequences and risks of hazards. This separation relates to inability to determine the impact threat from a given damage occurrence (i.e. match the consequence of a threat with the actual threat). This is the exact issue MIDAS solves by applying the deductive and inductive solution procedures. The indicated paper presents a methodology to systematically and fully address 4 of the 5 steps in ICAO's Safety Risk Management Process by solely using the MRO structural damage data and MIDAS. This leads to the conclusion that MIDAS does not solely convert Dents to Dents, but has the potential to move from Dents to Dollars.

Chapter 7

Conclusion, Discussion and Recommendations

This conclusion reviews to what extent the research questions are addressed and the corresponding steps to achieve the research objective. The discussion continues with the limitations of the analytical approach, which sets up the recommendations for future work. An important aspect of this concluding chapter is a trade-off between the scientific and practical value of this thesis. The research objective has been defined as:

"To predict impact damage on next-generation (composite) aircraft based on maintenance data of in-service (metal) aircraft"

which is evaluated by addressing the following two research questions:

I *To what extent can impact damage be predicted given a specific impact threat to an aircraft primary structure?*

II *To what extent can an impact threat be deduced from a given damage description on an aircraft primary structure?*

7.1 Conclusion

In order to achieve the research objective, the presented work focused on the relation between an impact threat and the corresponding residual deformation. An analytical approach is developed to Model Impact Damage on Aircraft Structures (MIDAS), which is used to either predict (induce) impact damage, or deduce impact threats for composite (-C) and metal (-M) targets. As part of the verification of the inductive solution of MIDAS, two numerical models (FEM) have been developed in ABAQUS, which have been validated by experimental results of Fagerholt et al. [18] and Lopes et al. (composite) [19].

The predictions of MIDAS-M and the metal FEM are in excellent agreement considering centrally impacted square metal plates with sides and thicknesses ranging between respectively 200–300 mm and 1.5–3.0 mm. Within this region, MIDAS-M is able to reproduce both the force-displacement path and the maximum or permanent deformation shapes in a fraction of the time of the numerical model (i.e. in 20 seconds compared to 12 hours).

On the other hand, the predictions of the composite numerical model and MIDAS-C are in good agreement with experimental results before the Damage Threshold Load (DTL), whereas the composite numerical model is unable to reproduce the experimental results beyond DTL. This relates to the lack of a ply separation law to properly account for delaminations. The verification of MIDAS-C is therefore deemed inconclusive. A validation of MIDAS-C using experimental impact data of F. Esrail (including delamination and fiber breakage) shows that the residual indentation and impact response predictions are in good agreement for a quasi-isotropic and orthotropic laminate using plies of 0^o, 90^o and $\pm 45^o$. The impact response predictions diverged for a highly orthotropic laminate, which primarily consist of $\pm 15^o$ plies. This relates to the radially averaging laminate properties in several steps of MIDAS-C, which is not appropriate for highly orthotropic laminates.

In addition to the inductive validation, the experimental results allowed a deductive validation of MIDAS-C. The deductive procedure is considered in two conditions: either partially-informed or not-informed (i.e. with knowledge of the impactor size or without any information of the impact threat). The partially-informed procedure, which only depends on the residual indentation depth, provides estimates with errors below 10% and 30% respectively for the quasi-isotropic and orthotropic laminate. The prediction errors increase to approximately 100% and 200% for respective laminates in the not-informed case. The increase of error is directly related to the dent width measurements. These measurements are highly sensitive to human error due to the variation in perceived dent sizes.

The respective good to excellent agreement of MIDAS-M and MIDAS-C with the available data from the field relate to the assumed contact behaviour and deformation shapes. The analytical approach in case of metal structures includes a transition region between the conventionally assumed local and global deformation modes. MIDAS-C, on the other hand, only includes the local and global deformation modes. The reduction of the local contact and the global bending or membrane stiffness terms upon damage initiation ensures that the impact response and residual indentation depths are in line with the experimental (composite) data.

The applicability of the models are illustrated by a case study, in which impact damages on a (composite) Boeing 787 fleet are predicted based on the maintenance records of a (metal) Boeing 777 fleet. The conversion process assumes equivalent metal and composite plates designs, which provide converged impact threat and damage estimates for 113 of the 120 damage entries. The estimated number of high consequence damages increased from 13 to 20 cases by moving from the Boeing 777 to the Boeing 787 fleet.

MIDAS is developed using several simplifications with respect to actual impact events on aircraft structures. The verified or validated analytical models provide reasonably accurate estimates for a wide range of impact threats within one minute compared to several hours for highly computational and time-intensive numerical case-by-case alternatives. Moreover, the not-informed deductive validation step illustrates that the discrepancy due to the measurement uncertainty is equally or more important as the deviation due to the model assumptions.

7.2 Discussion

As is briefly addressed in the conclusion, the applicability of this work is constrained by the primary model assumptions. These assumptions can be summarized in three categories by:

- (A) the simplifications of the impact event,
- (B) the assumed material response and modes of deformation,
- (C) and the perceived residual deformations.

The assumed material response and corresponding modes of deformation of (B) are the primary contribution of this thesis to the current state of the art. These assumptions are considered sufficiently appropriate as a result of the verification and validation steps. The perceived residual deformation by maintenance personnel of (C) is identified as a limitation of MIDAS. However, the simplifying assumptions of (A), which specify the impact threats and aircraft structure, need to be evaluated. This research addresses a part of the research question, which considers the ability of MIDAS to induce impact damage and deduce impact threats for rectangular flat composite and metal plates impacted by a rigid (steel) impactor. The validity of MIDAS to reproduce actual impact events on aircraft structures is not explicitly addressed. The primary simplifications of an impact event that have been used as starting point of the analytical development (chapter 3) are:

- **A-1** An impact threat is characterized by spherical impactor with a radius (R_i) and impact energy (U)
- **A-2** The target structure is simplified to flat plate that is either clamped or simply supported.
- **A-3** Impact events are boundary dependent and properly approximated as a quasi static event.
- **A-4** Impact events occur on the target's center and are perpendicular to its surface.

The effect of several model simplifications have been briefly addressed in the discussion of application chapter (see section 6.4). The literature review indicated that there are several types of impact threats. The assumed spherical shape of **A-1** serves as reasonable first order approximations of these threats, while the rigid nature of the impactor misses some relevant aspects. The impactor deformations of for example hail or the rubber bumpers of Ground Service Equipment (GSE) are not captured. Research suggests that these deformation modes could be addressed by assuming an increased contact area due to the perceived increase of impactor radius. However, dedicated research is required to evaluate and adapt MIDAS' applicability for these types of impact threats.

The quasi-static and boundary dependent assumption of **A-3** appears appropriate within the considered reference scenarios. However, a significant portion of the case study's predicted impacts threats have impactor radii below 10 mm. These threats would, for example, be classified as small mass boundary independent events by Olsson [87].

Moreover, the assumed boundary conditions of **A-2** effectively restrain the stringer and frame movements. The verification, validation and application chapter showed that large plate deflections are required to completely absorb and convert the impact energy. Part of this energy will in aircraft structures be taken up by stringer and frame displacement. In the same line of reasoning, the failure of these skin reinforcements is not explicitly addressed, while it is a primary mode of failure in GSE related impact events.

Finally, assumption **A-4** considers only perpendicular and centrally located impacts. This assumption allows a rapid generic approach for the entire range of reference damages, but underestimates the plate stiffness for off-center impacts. Even though the precise damage location with respect to stringer and frame boundaries is not always recorded, the accuracy of impact threat predictions will vary. However, the specific analysis of individual impact locations increases computation time and simplicity of the model. As a simplifying alternative, several reference locations could be considered. For example, impact locations with an offset boundary of 10%, 25% or 50% of the stinger and frame pitch from the plate could be provide direct estimates of the effect of off-center impacts. The need of such a simplification depends on the size and distribution of the reference damage data set considered.

Even though the indicated limitations provide relevant research perspectives for future work, the applicability and practical value of the current state of MIDAS should not be marginalized. Aircraft maintenance is a strict time constrained field of work, in which turn-around-times and decision-making within hours compared to days is preferred. The current state of MIDAS allows initial estimates within minutes for a wide range of impact threats, while the discrepancies of the indicated model limitations should be compared to the uncertainty caused by (human) measurement errors.

7.3 Recommendations

The presented work focused on the relation between an impact threat and the corresponding residual deformation. This relation is used to either (I) predict (induce) impact damage, or (II) deduce the impact threat. The recommendations for future work based on the presented work are two fold depending on the intended research purpose (i.e. considering a scientific or practical point of view).

From a practical perspective, a key next research step is to investigate the actual perception of residual damage by maintenance personnel and relate these insights to the predicted model deformations. The current state of MIDAS uses estimates of the plastic radius and discontinues change of deformation slope in respectively metal and composite plates. Cook [22] has performed some initial steps in the deformation shape perceptions, which separates the inner and outer radius of curvature of a dent. The transition region of MIDAS-M partly addresses this outer portion, while it is neglected in MIDAS-C. Future research should continue on the work of Cook, but more importantly guidelines need to be developed to defined the boundaries of residual indentation in the relatively smooth outer region.

From both a practical and scientific point of view, the model limitations addressed in the discussion need to be evaluated. The quasi-static approximation remains a reasonable initial estimate, whereas the limitations of the boundary dependencies restrict the practical value

of MIDAS. The deformation and failure of support structures is an essential requirement for future work. This relates to the detectability and the corresponding safety concerns of damage in support structures. The deductive solution with the addition of damages in sub-structures will become more challenging. This relates to both the specification of the extent of damage, and the variability of types of damages encountered.

From a scientific point of view, the extent of damage needs to be addressed. The current modelling efforts included stages of sub-surface damage and the penetration limits for respectively composite and metal targets. The limits of the respective stages provide a qualitative indication of the extent of damage, but (validated) quantitative estimates of the extent of damage are missing (i.e. size estimates of delaminations and regions of fiber failure). Similarly, the damage tolerance aspect of impact in terms of the residual strength estimates are not considered. These quantitative estimates allow a more detailed and well-informed maintenance planning. A key trade-off in this field of research remains time and computation intensive nature of complete quantitative damage estimates compared to the rapid qualitative estimates. The initial next development steps should focus on developing an appropriate numerical model to approximate subsurface damage types, and compare these with qualitative estimates of for example MIDAS. Based on those comparisons, the need for quantitative damage estimates and corresponding analytical models can be reconsidered.

Appendix A

Experimental results and post-processing

A.1 Post processing of experimentally recorded force response

During the impact experiments, as discussed in chapter 5, the impactor contact force is measured over time. An example of the recorded force history of specimen QI2.6 is shown in Figure A.1, which corresponded to an impact energy of 36.58 J. This recorded data requires post-processing for two reasons. Firstly, recorded data includes a significant time portion before and after the actual impact event. Secondly, the measured contact force contained noise. The noise can be seen in the recorded signal before and after the impact, which shows a reasonably flat response with a high frequency osciliation of a small amplitude.

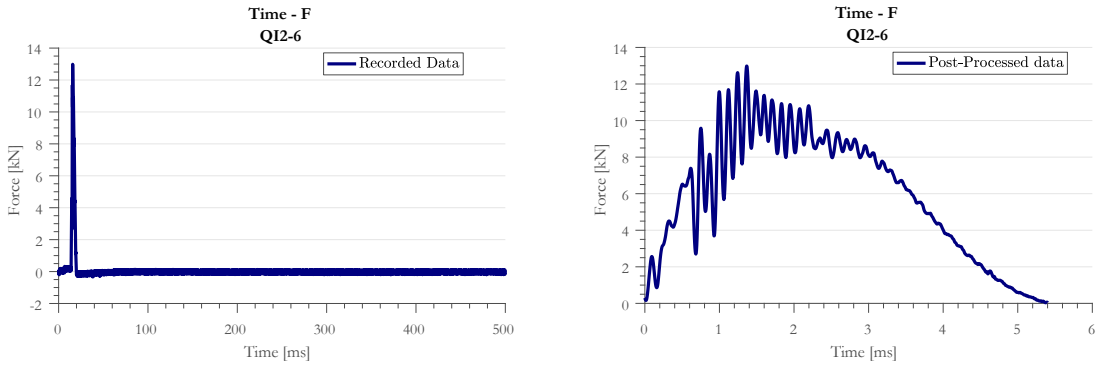

(a) Originally recorded data **(b)** Post-Processed data

Figure A.1: Recorded and post-processed contact force over time of specimen QI2.6 impacted with 36.58 J

The first step is isolating the actual impact event from the signal. The signal consists of three stages in time: 1) before impact, 2) impact and 3) after impact. In the last stage, the signal

remains reasonably constant. The end of impact corresponds to the maximum of the force integrated over time, as shown in top graph of Figure A.2. While the initiation of impact corresponds to a instantaneous increase in force, which could be obtained using the derivative of the force history. The use of the derivative is limited due to the contained noise. However, the trend can still be captured if averaged over a larger time interval. Therefore, the derivative is taken using a time step 10 times the sampling rate. The original and averaged derivatives are shown in the middle of Figure A.2. This shows that the averaged derivative reduces the effect of noise, and the initiation of impact can be deduced. The resulting impact region is shown on the bottom figure of Figure A.2.

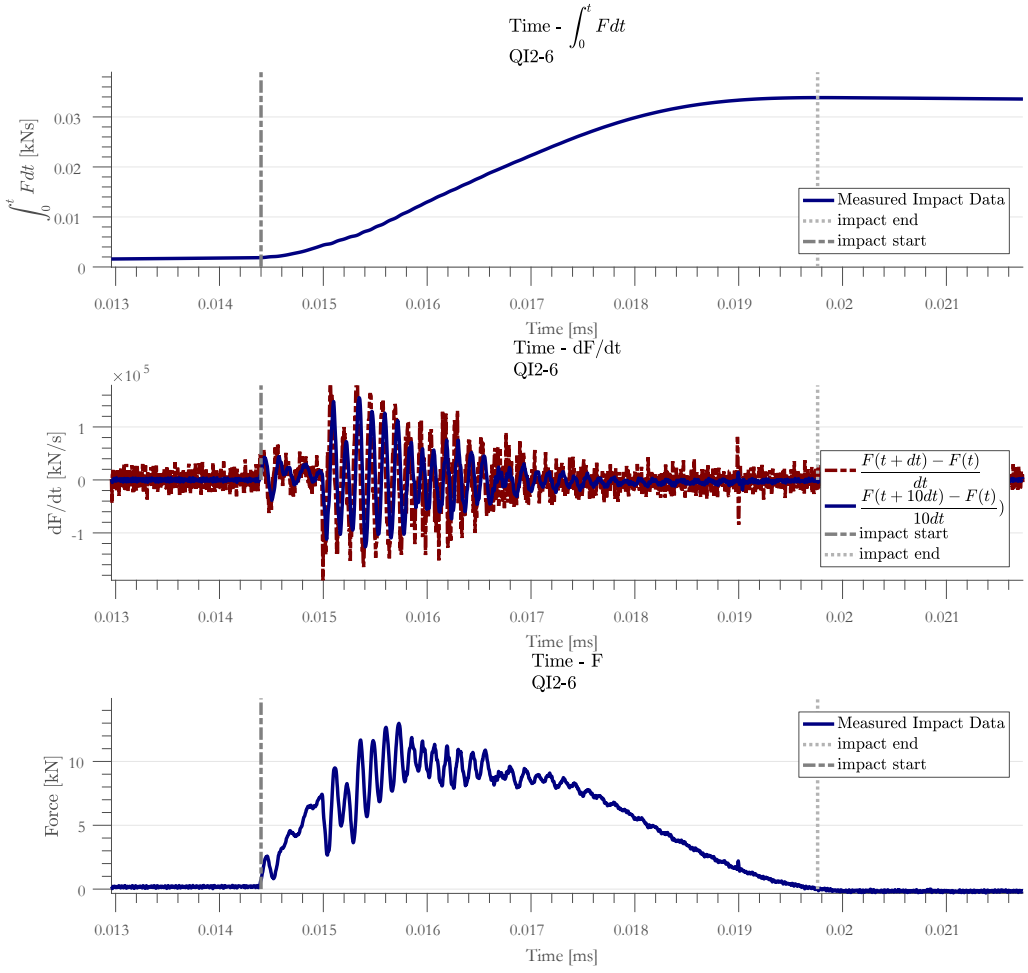

Figure A.2: Extraction of impact response from recorded signal

The described procedure allows the determination of the impact duration, but still contains the noise in the actual signal. The measured signal shows the general trend of the response, but the noise limits the readability, as well as that the vibrations in the system are not properly reproduced. Therefore a Savitzky-Golay (polynomial) smoothing filter is used to filter the noise out of the impact response, while maintaining it's oscillating behaviour. Savitzky-Golay filters are low-pass filters based on moving averaging windows in the time-domain compared

to frequency domain filters. In extension on moving averaging windows, the Savitzky-Golay filters superimpose polynomial weight on the center of the window, such that narrow peaks are still reproduces compared. The lowest order filter that approximates the recorded signal is desired, as it minimizes the effect of noise. Both a 3rd and 5th order Savitzky-Golay filter with an averaging window of 31 measurements approximate the recorded data well, as shown in Figure A.3. However, the 3rd order filter under estimates the peaks, which are important data characteristics of the impact response.

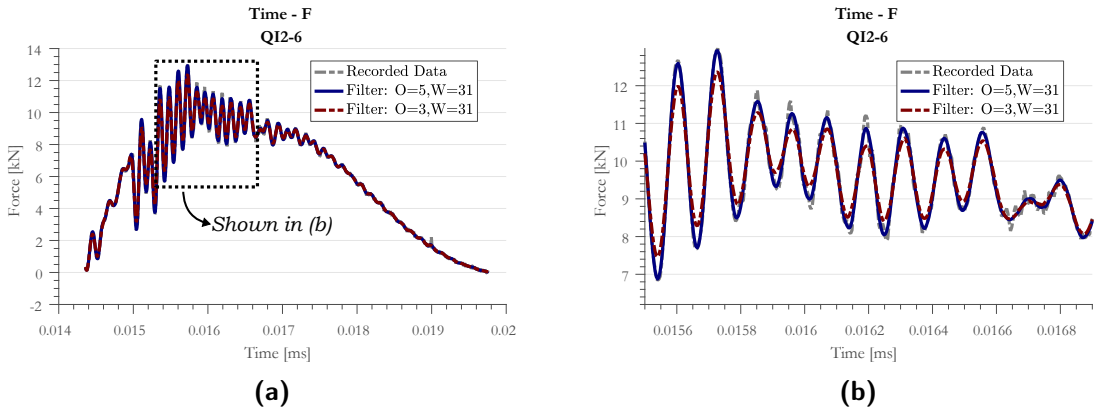

Figure A.3: Comparison of recorded force-time response with a 3rd and 5th order Savitzky-Golay filter

A.2 Determination of characteristics of impact response

This section elaborates on the impact characteristics described in subsection 5.2.2. The determination of the impact characteristic requires several post-processing steps. The following characteristics are determined:

Peak force indicated by subscript *peak* refers to the maximum force during an impact event

Max displacement indicated by subscript *max* refers to the maximum displacement during an impact event

Residual displacement indicated by subscript 0 refers to the impactor displacement directly after impact

DTL indicated by subscript DTL refers to the Delamination Threshold Load during an impact event

These characteristics are quantified in terms of force, displacement and absorbed energy. This section describes the determination of these quantities. A single parameter needs to be determined to obtain the remaining two characteristics[1].

[1] As indicated in Appendix A.1, the force, displacement and absorbed energy data entries are measured over time. The determination of a single parameters directly defines the remaining two (i.e. for a given force, the displacement and energy are obtained at the same time entry).

A.2.1 Determine peak force

The peak force is obtained from the force-time data vectors. The function `Find_PeakForce` is created in MATLAB to determine the characteristics as shown in the following code segment:

```
function [T_peak,d_peak,N_peak,E_peak] = Find_PeakForce(Ts,ds,Ns,Es);

    % Find maximum of Force variable (Ns)
    [N_peak,INpeak] = max(Ns);

    % Use max force index to obtain remaining variables
    T_peak = Ts(INpeak);    d_peak = ds(INpeak);    E_peak = Es(INpeak);
end
```

A.2.2 Determine max displacement

The max displacement is obtained from the displacement-time data vectors. The function `Find_MaxDisplacement` is created in MATLAB to determine the characteristics as shown in the following code segment:

```
function [T_dmax,d_dmax,N_dmax,E_dmax] = Find_MaxDisplacement(Ts,ds,Ns,Es);

    % Find maximum of displacement variable (ds)
    [d_dmax,Idmax] = max(ds);

    % Use max force index to obtain remaining variables
    T_dmax = Ts(Idmax);    N_dmax = Ns(Idmax);    E_dmax = Es(Idmax);

end
```

A.2.3 Determine residual displacement

The residual displacement is obtained from the displacement-time data entry. The point is defined as whenever the impact force returns to zero. The function `Find_ResidualDisplacement` is created in MATLAB to determine the characteristics as shown in the following code:

```
function [T_d0,d_d0,N_d0,E_d0] = Find_ResidualDisplacement(Ts,ds,Ns,Es);

    % Find point when force is equal or smaller than 0.
    [¬,Id0] = find(Ns < =0,1,'first');

    % Use max force index to obtain remaining variables
    T_d0 = Ts(Id0);    d_d0 = ds(Id0);    E_d0 = Es(Id0);

end
```

A.2.4 Determine Delamination Threshold Load (DTL)

The determination of the DTL requires several steps. The determination is based on the following two observations:

- (A) The DTL is followed by an apparent load drop Olsson [113]
- (B) The global bending stiffness decreases after DTL[80]

Based on these observations the peaks and valleys of the dynamic oscillations are determined to perform a bi-linear regression fit optimization. The bi-linear regression continues on observations (II) that there is a difference in stiffness before and after DTL. The initial linear regressions (i.e. pre-DTL) passes through the origin till approximately the DTL, and the second step (i.e. post-DTL) has a reduced slope. The procedure can be summarized by the following steps:

- (I) The peaks and valleys of individual impact response are isolated (see lines 1-32 of `Find_DTL`)
- (II) A bi-linear regression fit optimization is performed on this isolated data set (see `OptimizeLinearFit` and lines 25-31 of `Find_DTL`):
  - **a** determine first linear regression through origin (i.e. $y = b_1 x$) for isolated points (1 to n)
  - **b** determine second linear regression not through origin (i.e. $y = b_1 x + b_2$) for isolated points (n+1 to end), see
  - **c** combine first and second regression to bi-linear regression
  - **d** determine Root-Mean-Square-Error (RMSE) of bi-linear regression
  - **e** increase index n by one and repeat a-d
  - **f** Obtain optimized bi-linear regression due to least RMSE

Only the loading region before the peak load is considered. This relates to the possible post-fiber breakage region after the peak load. The RMSE optimization and the resulting bi-linear regressions of specimen OR1-11, F1-7 and QI1-7 are shown in Figure A.4, A.5 and A.6.

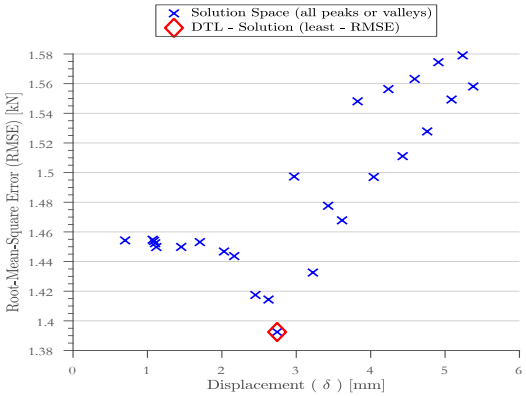

(a) Optimization of Root Means Square Error of bi-linear regression fit

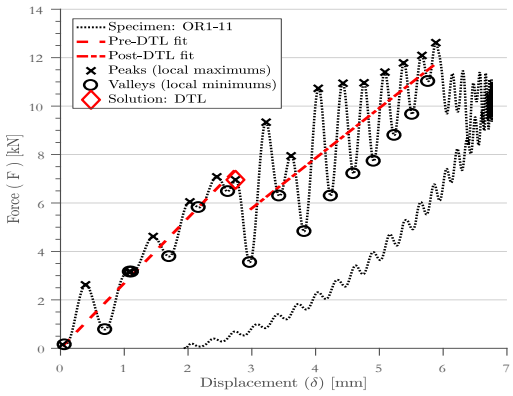

(b) Resulting bi-linear regression fit

Figure A.4: Determination of DTL for specimen : OR1-11

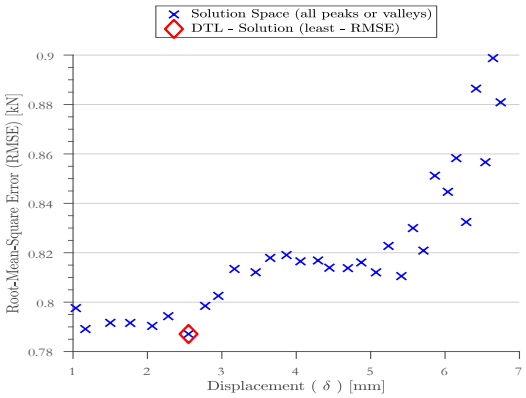

(a) Optimization of Root Means Square Error of bi-linear regression fit

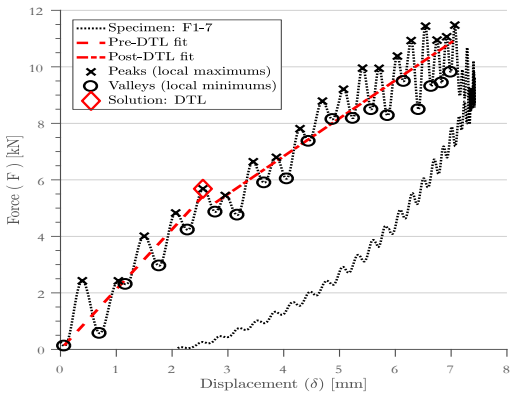

(b) Resulting bi-linear regression fit

Figure A.5: Determination of DTL for specimen : F1-7

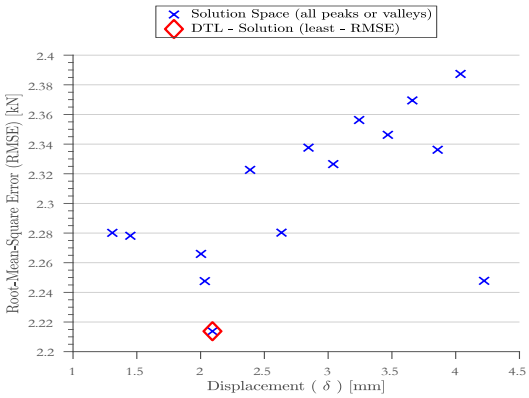

(a) Optimization of Root Means Square Error of bi-linear regression fit

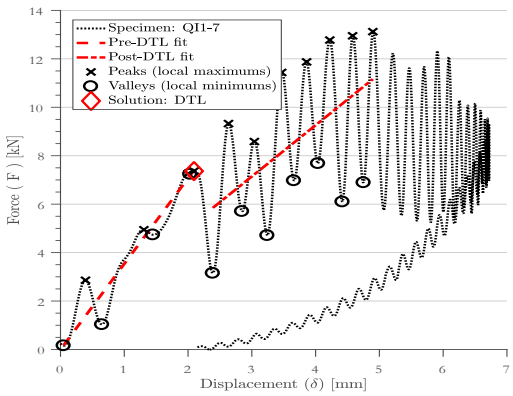

(b) Resulting bi-linear regression fit

Figure A.6: Determination of DTL for specimen : QI1-7

```
function [T_DTL,d_DTL,N_DTL,E_DTL]  = Find_DTL(Ts,ds,Ns,Es,name);

    %% Determine loading region of impact reponse (up to max displacement)
    [¬,¬,N_peak,¬] = ExperimentalData.Find_PeakForce(Ts,ds,Ns,Es);
    idx_dmax = find(Ns==N_peak);
    idx_loading = 1:idx_dmax+1;

    %% Loading variables
    Ts_load = Ts(idx_loading);      ds_load = ds(idx_loading);          ...
        Ns_load = Ns(idx_loading); Es_load = Es(idx_loading);

    %% Determine Peaks/Valleys of loading region
    [N_pks,d_pks] = findpeaks(Ns_load,ds_load);  %peaks
    [N_vls,d_vls] = findpeaks(-Ns_load,ds_load); %valleys

    %% Combine peaks and valleys into single vector
    d_ext = zeros(length(d_pks)+length(d_vls),1);
    if min(d_pks) < min(d_vls);
        % starting index == Peak
        d_ext(1:2:end) = d_pks;        d_ext(2:2:end) = d_vls;
    elseif min(d_pks) > min(d_vls);
        % starting index == Valley
        d_ext(1:2:end) = d_vls;        d_ext(2:2:end) = d_pks;
    end

    %% Bi-linear fit optimization
    % (i.e. separate d_ext-N_ext in two linear regression regions with
    % the Least Root Mean Square [of bi-linear segmentation])
    [Idx_DTL,N_fit_lin] = OptimizeLinearFit(d_ext,N_ext);

    % Resulting DTL variables
    T_DTL = T_ext(Idx_DTL);         d_DTL = d_ext(Idx_DTL);             ...
        N_DTL = N_ext(Idx_DTL);    E_DTL = E_ext(Idx_DTL);

end
```

```
function [Idx_lin,N_fit_lin] = OptimizeLinearFit(d_avg,N_avg);
%% Obtain bi-linear fit
% Segment 1)
%   - linear fit through Origin
%   - matlab code : b = x\y                     --> y_fit = b*x
% Segment 2)
%   - linear fit not through Origin
%   - matlab code : b = [ones(length(x),1) x]\y --> y_fit = b*x

    idx = []; %Initialize index variable
    for i = 1:length(d_avg)-7;
        idx = [idx i];

        %% Obtain bi-linear fit
        [y_fit1_lin] = LinearRegression(d_avg(1:i+3), N_avg(1:i+3),true);
        [y_fit2_lin] = LinearRegression(d_avg(i+4:end), N_avg(i+4:end),false);

        % Combine resulting fitting parts
        N_fit_lin{i} = [y_fit1_lin' y_fit2_lin'];
```

```
20
21          %Determine Square Error (i.e. [1/n*sum((N_avg-N_fit).^2]^0.5)
22          [SSresid_lin(i)] = ObtainRootMeanSquareError(N_fit_lin{i},N_avg);
23      end
24
25      % Find idx for minimum error
26      [¬,Idx_lin] = min(SSresid_lin);
27
28      % Obtain Optimized Fit results
29      N_fit_lin = N_fit_lin{Idx_lin};
30      Idx_lin = Idx_lin + 3; % DTL idx correponds to end point of first ...
            segment (i.e. off set by 3 w.r.t. line 15)
31  end
32
33  function [SSresid] = ObtainRootMeanSquareError(N_fit,N_avg)
```

A.3 Human error in damage width measurements

As discussed in subsection 5.2.3, the dent width measurements are sensitive to human errors. This relates to the interpretation of the damage and a clear dent edge is not apparent. To evaluate the effect of inspectors judgment, a group of 12 participants were asked to measure the dent width of 5 impacted specimens. The selected specimens consisted of the three layups (F/QI/OR) and all 4 impact energies. Each participant measured the samples individually after receiving the following instructions:

- The width of the indentation needs to be measured using a caliber.
- Measure once in the x-direction (smaller edge of specimen).
- Measure once in the y-direction (longer edge of specimen).
- Evaluate whether a large width is observed in arbitrary direction and measure this width.
- The edge of the dent is defined as first observable change in slope. Each participant is advised to rotated the specimen with respect to the light.

The resulting measurements are shown in Figure A.7. The minimum, maximum and mean measurement in each direction is shown. In addition, the standard deviation around the mean is indicated by the box. The results show that significant variation in measurements are reported.

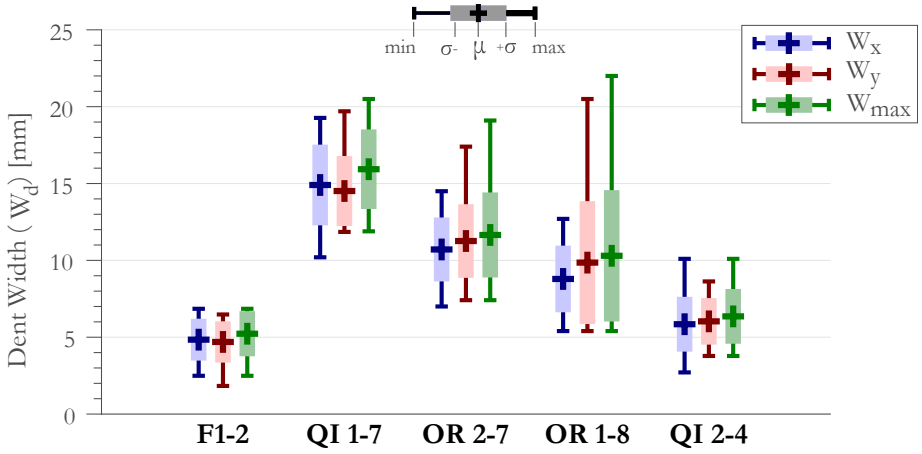

Figure A.7: Variation of measured dent width of a group of 12 students

A.4 Experimental impact response results

The impact responses of layup types F, QI and OR are shown in Figure A.8, A.9 and A.10. The results are summarized on a case by case basis (i.e given combination of impact energy and lay up type). This shows that variation exists within a single impact case.

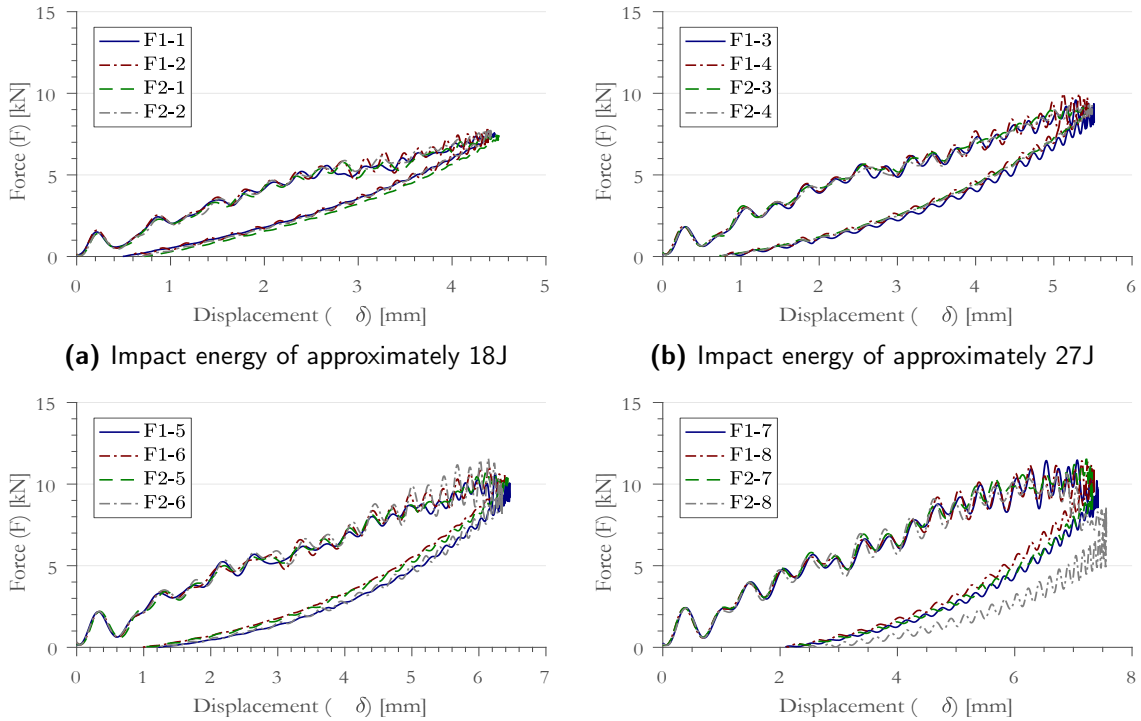

(a) Impact energy of approximately 18J

(b) Impact energy of approximately 27J

(c) Impact energy of approximately 37J

(d) Impact energy of approximately 46J

Figure A.8: Variation impact response of layup type F with constant impact energy.

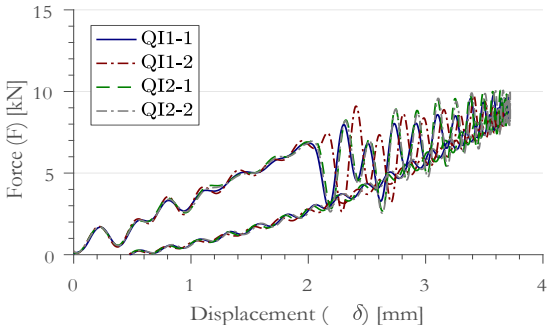

(a) Impact energy of approximately 18J

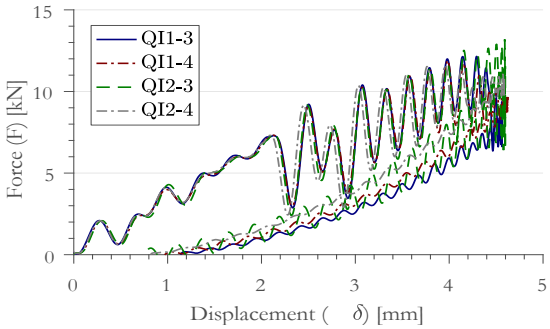

(b) Impact energy of approximately 27J

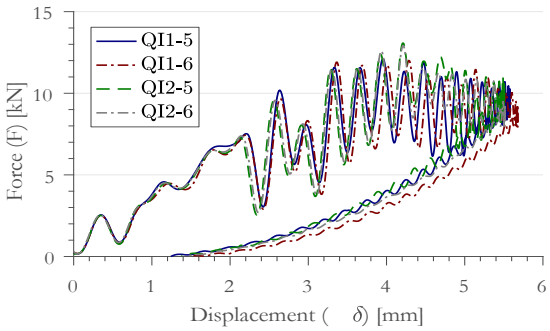

(c) Impact energy of approximately 37J

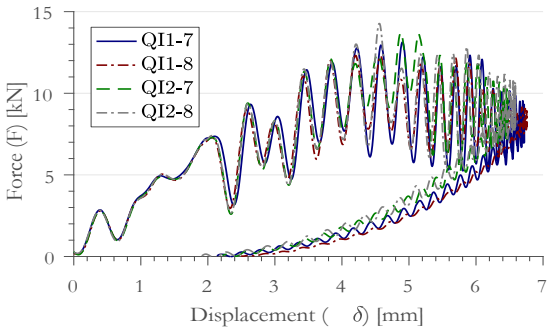

(d) Impact energy of approximately 46J

Figure A.9: Variation impact response of layup type QI with constant impact energy.

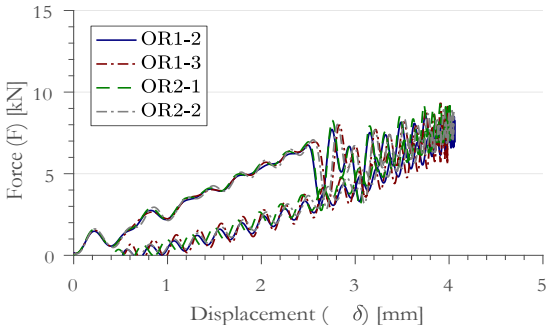

(a) Impact energy of approximately 18J

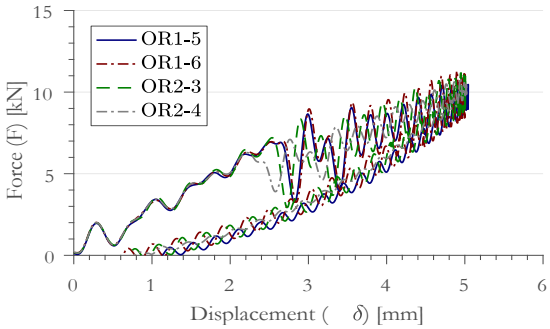

(b) Impact energy of approximately 27J

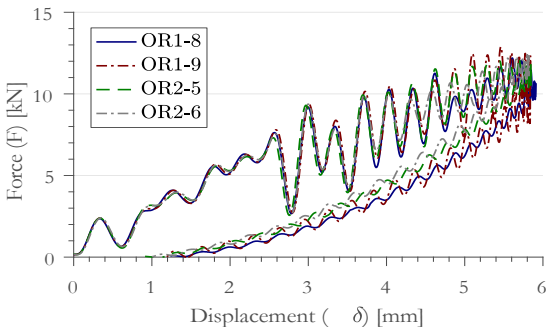

(c) Impact energy of approximately 37J

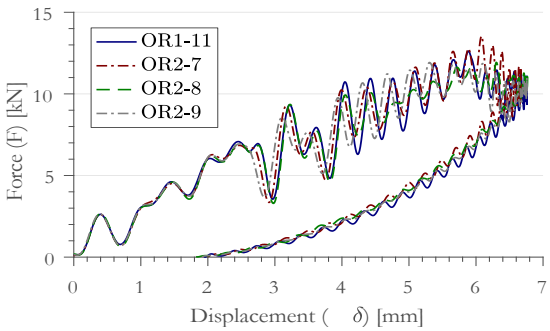

(d) Impact energy of approximately 46J

Figure A.10: Variation impact response of layup type OR with constant impact energy

Appendix B

Additional validation MIDAS-C

In subsection 3.3.2, several methods have been proposed to predict the progressive loading behaviour after either DTL or IFB. This appendix briefly elaborates on the different estimates and shows the differences. In addition, an alternative deductive solution is shown using the permanent dent radius instead of the relaxed dent depth.

B.1 Comparison of DTL load drop estimates

The initiation of, and the residual load after delamination have been estimated using the DTL of single and multiple equivalent circular delaminations. The estimate of the equivalent number of delaminating interfaces (n^*) followed from the relation given by Olsson [81] using a scaling factor based on bending stiffness mismatch of either Liu [120] or Morita *et al.* [20]. This section briefly compares the different estimates with respect to experimental data of F.Esrail. For simplicity, the generic equations of (n^*) from Olsson [81]and the modified version to using either Liu's or Morita's bending stiffness mismatch are summarized in Equation B.1.

$$\begin{aligned} n^* &= \bar{A}\left[\bar{A}_{45}\, n_{\Delta 45} + n_{\Delta 90}\right] && \text{Generic from Olsson [81]} \\ &= \bar{A} \sum_{i=1}^{n} \frac{\beta_i}{\beta_{max}} && \text{modified using Morita } \textit{et al.} \text{ [20]} \\ &= \bar{A} \sum_{\Delta\theta} \bar{A}_\theta n_{\Delta\theta} && \text{modified using Liu [120]} \end{aligned} \tag{B.1}$$

B.2 Comparison of IFB path estimates

In subsection 3.3.2, several progressive loading path estimates have been proposed. Within the context of conservatism two outer limits were proposed using pure penetration without any additional structural deflection, and a third alternative assuming loss of the residual bending load and some additional deflection followed by pure penetration was proposed. This final

alternative appears best suited to reproduce an impact event. The comparison of the models is based on a comparison of the actual load paths, and the final indentation estimates. The highest impact level is ideal for this comparison, as a larger region after IFB is available. The impact response estimates allow a visual comparison of the path estimates, while the typical knee point diagram compares the actual estimates. Both comparisons are shown for each specimen type in Figure B.1 to Figure B.3.

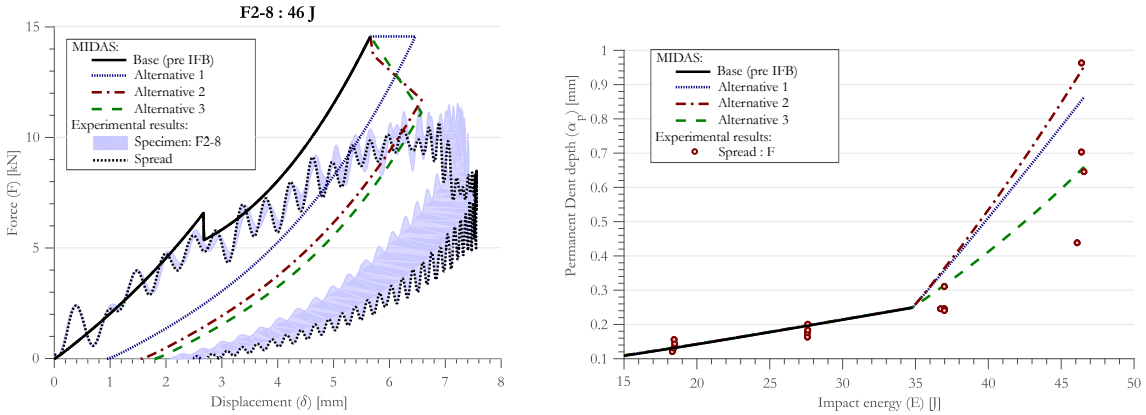

(a) Comparison of the impact response estimates

(b) Comparison of permanent indentation estimates

Figure B.1: Comparison the three penetration path alternatives with respect to layup type F

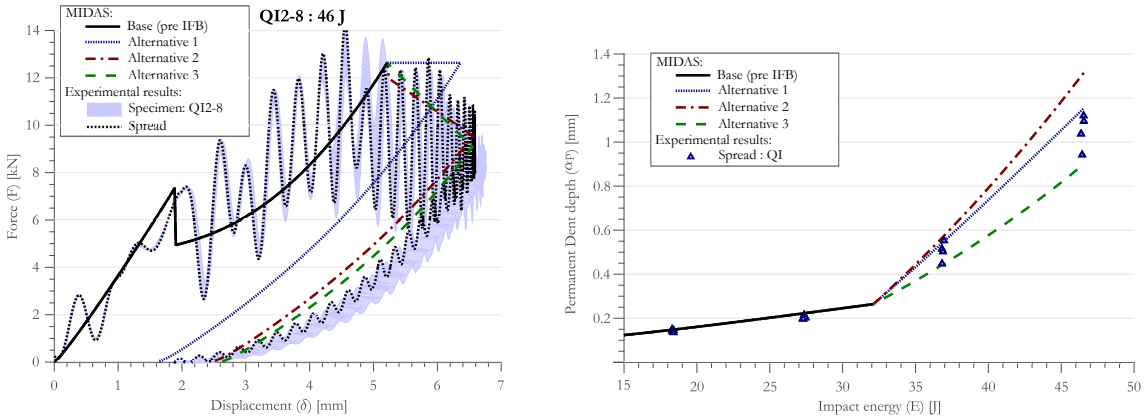

(a) Comparison of the impact response estimates

(b) Comparison of permanent indentation estimates

Figure B.2: Comparison the three penetration path alternatives with respect to layup type QI

The impact response comparisons show that the point of IFB is reasonably predicted for both QI and OR layups, while it is significantly overestimated for layup type F. The impact response comparisons show that the first approximation under estimates the total deflection and overestimates the force at end of loading. The reduction of impact load in both other alternatives show reasonable agreement with the experimental data. The final indentation estimates, however, show that the the second alternative significantly overestimates the indentation depths.

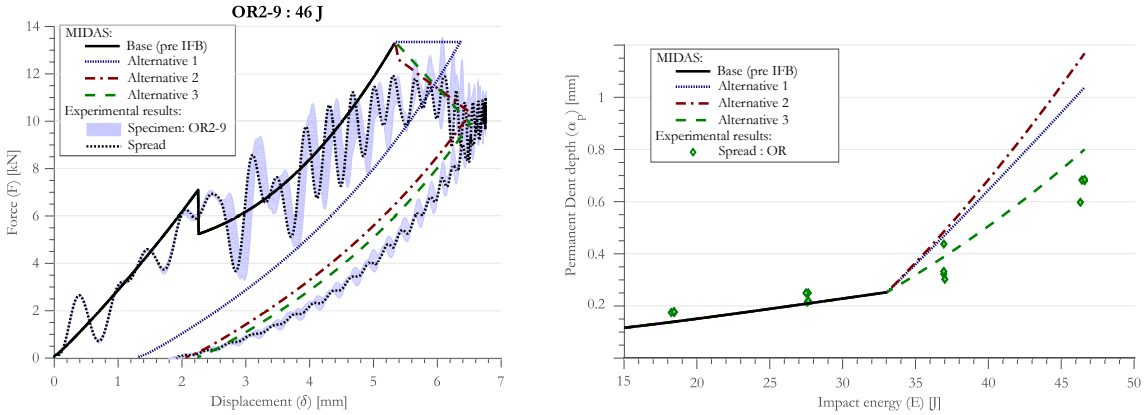

(a) Comparison of the impact response estimates

(b) Comparison of permanent indentation estimates

Figure B.3: Comparison the three penetration path alternatives with respect to layup type OR

It is expected that the indentation estimates of alternative 2 surpass alternative 1, as effectively a larger indentation is required to achieve same energy level (i.e. (1) and (2) have pure indentation paths, while (1) has a constant force compared to a decreasing force of (2)). The lower bound estimate of (3), which includes some additional structural deflection, has a lower estimate compared to (2). The indentation estimate have significant scatter, and for example Figure B.2b, shows that all results are contained in the upper and lower bound estimates of (1) and (3). While (1) significantly over estimates the indentations estimates for OR specimens. An overall comparison shows that the third alternative has the best approximation of both the impact response as well as the permanent indentation estimates.

B.3 Deductive Solution procedure using plastic radius

Within the validation of MIDAS, the deductive solution procedure for a known impact radius was presented. This section provides an alternative approximation using the permanent dent radius in stead of the relaxed indentation depth. The predicted and relative errors are shown in Figure B.4.

The estimated impact energies shown in Figure B.4a indicate that the use of plastic radius is not an appropriate estimation factor. The predictions of the target energy at approximately 18.6 J overspans both the 27.4 J and the 37.3 J cases. This estimation error ties back with the measurement error of the residual dent radius.

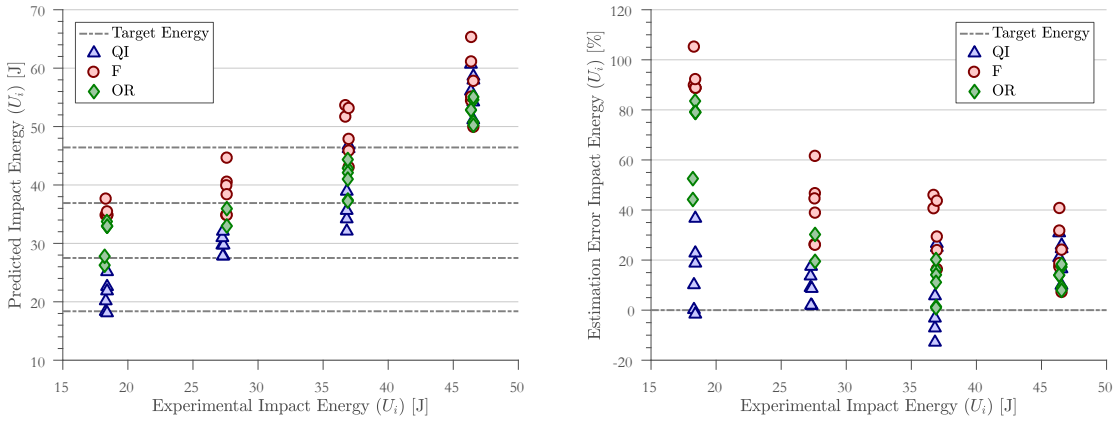

(a) Estimated impact energy **(b)** Estimation error

Figure B.4: Estimated impact energy given a known impactor radius as function of experimental impact energy using the plastic radius

B.4 Comparison of all impact events with MIDAS

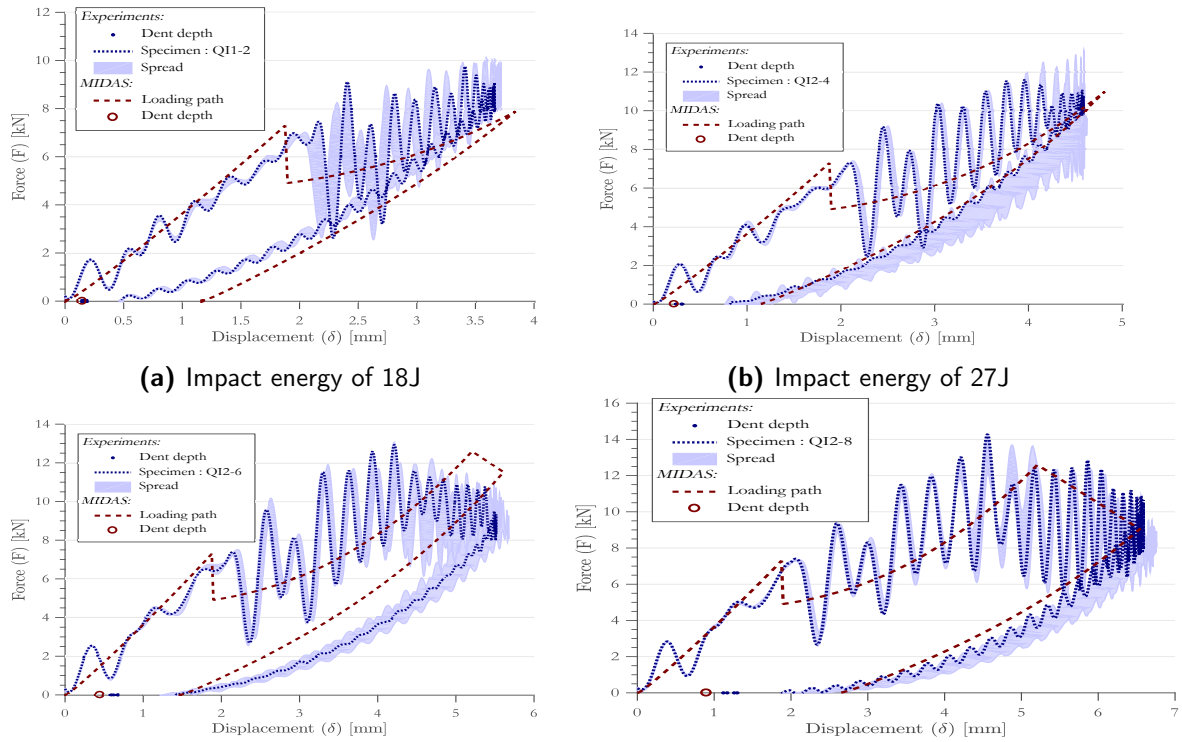

(a) Impact energy of 18J **(b)** Impact energy of 27J

(c) Impact energy of 36J **(d)** Impact energy of 46J

Figure B.5: Comparison of MIDAS-C with layup type QI

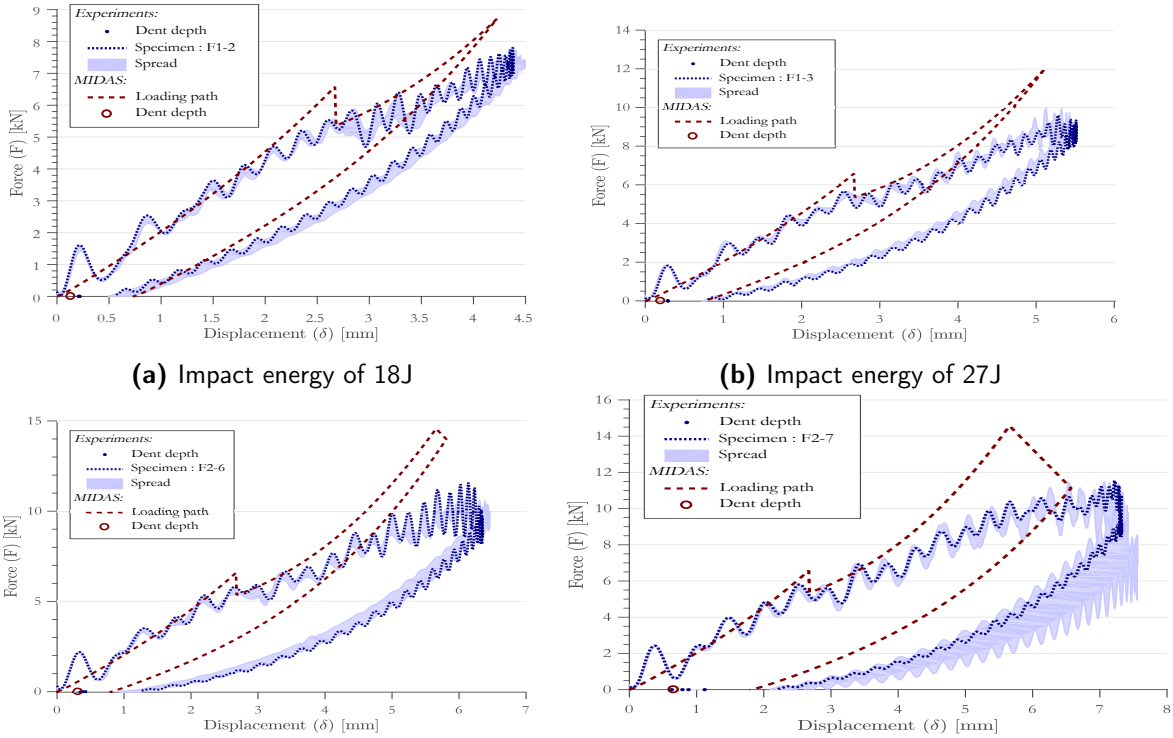

(a) Impact energy of 18J

(b) Impact energy of 27J

(c) Impact energy of 36J

(d) Impact energy of 46J

Figure B.6: Comparison of MIDAS-C with layup type F

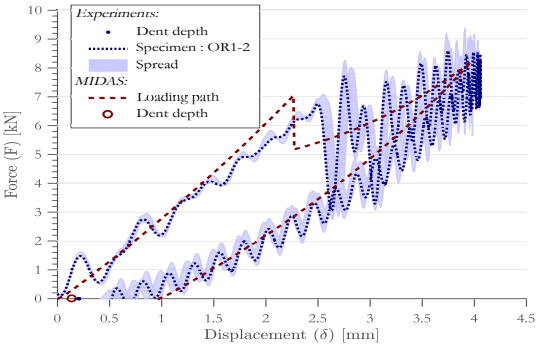

(a) Impact energy of 18J

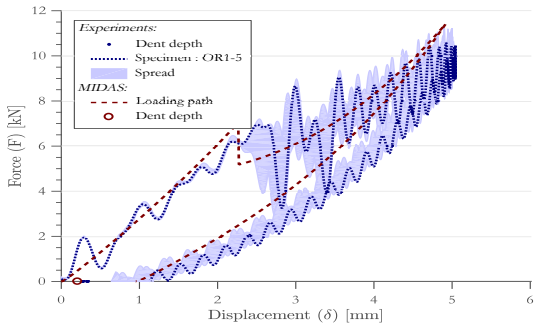

(b) Impact energy of 27J

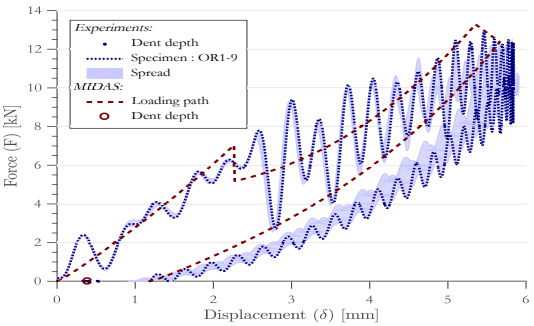

(c) Impact energy of 36J

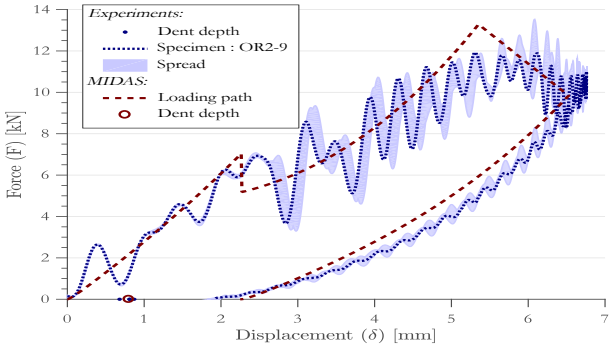

(d) Impact energy of 46J

Figure B.7: Comparison of MIDAS-C with layup type OR

Appendix C

Case study

C.1 Design of case study plates

A proper comparison of the Boeing 777 and 787 impact damages requires that the respective plate definitions have similar design criteria. To that extent, design criteria are defined covering the in-plane strength and buckling behaviour of the plates. The composite target plate is explicitly defined by (i) the layup sequence and (ii) the fuselage dimensions of a Boeing 787. The feasible design space of the metal target plate, on the other hand, is only constrained by the fuselage dimensions of the Boeing 777. The edge failure loads of the composite plates are used to determine an equivalent metal plate. The resulting design is summarized in Table C.1 and C.2, and the following sections describe the respective failure criteria. As indicated in Table C.2, the buckling due to bi-axial compression drives the metal design.

Table C.1: Design of target plates used in case study

Material	**Dimensions**			**Elastic Properties**		
	a mm	**b** mm	**t** mm	**Ex** GPa	**Ey** GPa	**D** Nm
Composite	227	610	2.9	54.1	54.1	121.6
Metal	230	530	2.52	70	70	102.6

C.1.1 In-plane failure requirement

The in-plane strength criterion is based on the requirement that both plates should withstand the same applied edge loads (i.e. the load applied per unit length). The edge failure loads of the composite plate are determined by a first-ply failure analysis using the Tsai-Wu failure criterion (Equation C.1), while the von mises yield criterion is used for the metal plate (see Equation C.2) [56]. The design variable for first-ply failure is adjusted by means of knockdown

Table C.2: Failure loads of target plates used in case study

Material	In-plane Failure					Buckling Failure		
	N_{uc} kN/m	N_{ut} kN/m	N_{bt} kN/m	N_{bc} kN/m	N_s kN/m	N_{uc} kN/m	N_{bc} kN/m	N_s kN/m
Composite	453.4	443.6	404.6	573.6	242.9	33.8	29.6	756.6
Metal	718.2	718.2	829.3	718.2	414.7	36.8	29.6	159.7

factors ($f_{_{KD}}$) to account for material scatter ($_{\text{MAT}}$), environmental conditions ($_{\text{ETW}}$) and reduced strength in case of BVID ($_{\text{BVID}}$).

$$\frac{\sigma_x^2}{X^tX^c} + \frac{\sigma_y^2}{Y^tY^c} - \sqrt{\frac{1}{X^tX^c}\frac{1}{X^tX^c}}\sigma_x\sigma_y + \left(\frac{1}{X^t} - \frac{1}{X^c}\right)\sigma_x + \left(\frac{1}{Y^t} - \frac{1}{Y^c}\right)\sigma_y + \frac{\tau_{xy}^2}{S^2} = 1 \tag{C.1}$$

$$\frac{\sigma_{xx}^2}{\sigma_y^2} + \frac{\sigma_{yy}^2}{\sigma_y^2} - \frac{\sigma_{xx}\sigma_{yy}}{\sigma_y^2} + \frac{3\sigma_{xy}^2}{\sigma_y^2} = 1 \tag{C.2}$$

The following five loading conditions are considered: uni-axial tension (ut), uni-axial compression (uc), pure shear (s), bi-axial tension (bt) and bi-axial compression (bc). The bi-axial tension requirement is based on the simplification that a fuselage can be considered a pressure vessel. The circumferential stress is therefore assumed twice the longitudinal stress (i.e. $\sigma_{xx} = \frac{1}{2}\sigma_{yy}$). The applied loads are assumed equal in the bi-axial compression case. The required plate thickness (t_i) per load case is determined by

$$t_i\, S_i = f_{_{KD}}\, N_i \quad \text{with} \quad \begin{aligned} f_{_{KD}} &= f_{_{KD,ETW}} \cdot f_{_{KD,BVID}} \cdot f_{_{KD,mat}} \\ &= 0.8 \cdot 0.65 \cdot 0.8 \end{aligned} \tag{C.3}$$

in which N and S refer to respectively the composite first-ply failure load and the metal failure stress, while subscript i indicates specific load case. The required thickness to achieve failure at the same edge load is summarized in Table C.5

Table C.3: Required plate thickness dependent on the In-plane failure criteria

Design variable	Unit	Uni-axial tension ut	Uni-axial compression uc	Bi-axial tension s	Bi-axial compression bt	Pure shear bc
N_i	kN/m	1089.8	1066.4	972.7	1378.9	584.0
$N_{i_{KD}}$	kN/m	453.4	443.6	404.6	573.6	242.9
S_i	MPa	285	285	329	285	165
t_i	mm	1.59	1.56	1.22	2.01	1.47

C.1.2 Buckling failure requirement

The second design criterion considers the buckling loads of plates. Three different buckling load conditions are considered : uni-axial compression, pure shear and bi-axial compression.

The buckling loads for composite and isotropic (metal) plates are obtained from respectively Kassapoglou [56] and Roark *et al.* [130]. In the following subsections the individual buckling approximations are given, while the resulting thickness requirements are summarized in Table C.4. The required shear thickness in case of buckling is not within the provided thickness range of a Boeing 777. However, the corresponding (composite) shear buckling edge load exceeds the first-ply failure load in shear. The shear buckling load is therefor not considered a driving factor.

Table C.4: Required plate thickness dependent on the buckling criteria

Design variable	Unit	Uni-axial compression	Bi-axial compression	Pure shear
		uc	*bt*	*s*
N_i	kN/m	296.6	337.6	756.6
t_i	mm	2.52	2.45	4.23

Table C.5: Required plate thickness dependent on the In-plane failure criteria

Design variable	Unit	Uni-axial		Bi-axial		Pure shear
		tension	compression	tension	compression	
		ut	*uc*	*s*	*bt*	*bc*
N_i	kN/m	~	296.6	337.6	~	756.6
t_i	mm	~	2.52	2.45	~	4.23

All isotropic (metal) buckling approximations have an equation of the form:

$$N_{i,m} = K_i \frac{Et^3}{1-\nu^2} f_i \tag{C.4}$$

in which K_i and f_i represent a load and shape factor relevant for the respective cases. The required plate thickness for each case can therefore be obtained by

$$t_i = \sqrt[3]{\frac{N_{i,c}}{K_i f_i} \frac{1-\nu^2}{E}}. \tag{C.5}$$

Uni-axial compression

The composite uni-axial compression buckling failure criterion is given by

$$N_{x,c} = \frac{\pi^2}{a^2}\left[D_{11}m^2 + 2(D_{12}+2D_{66})\left(\frac{a}{b}\right)^2 + D_{22}\left(\frac{a}{b}\right)^4 \frac{1}{m^2}\right], \tag{C.6}$$

in which a, b and D_{ij} terms refer to the plate edges and D matrix terms. The expression needs to be minimized for m to obtain the failure edge load. The isotropic (metal) buckling edge load is given by:

$$N_{x,m} = K_x \frac{Et^3}{(1-\nu^2)b^2} \tag{C.7}$$

The K_x term depends on the ratio $\frac{a}{b}$ and is given by Roark *et al.* [130, p. 730]. For respectively loading in longitudinal and transverse direction the K_x terms becomes 6.46 and 3.36.

Shear buckling load

The shear buckling load is determined based on approximation method given by two alternative methods for $(a/b) = 0$ and $0.5 \leq (a/b) \leq 1$ by Kassapoglou [56]. The aspect ratio of the plate is 0.434 and an interpolation between the two solutions is proposed. The $0.5 \leq (a/b) \leq 1$ is given by:

$$\begin{aligned} N_{xy} &= \frac{\pi^4 b}{a^3} \frac{1}{\sqrt{\frac{14.28}{D1^2} + \frac{40.96}{D1D2} + \frac{40.96}{D1D3}}} \\ &\text{with} \\ D1 &= D_{11} + 2(D_{12} + 2D_{66})\left(\tfrac{a}{b}\right)^2 + D_{22}\left(\tfrac{a}{b}\right)^4 \\ D2 &= D_{11} + 18(D_{12} + 2D_{66})\left(\tfrac{a}{b}\right)^2 + 81D_{22}\left(\tfrac{a}{b}\right)^4 \\ D3 &= 81D_{11} + 18(D_{12} + 2D_{66})\left(\tfrac{a}{b}\right)^2 + D_{22}\left(\tfrac{a}{b}\right)^4 \end{aligned} \tag{C.8}$$

and the $(a/b) = 0$ approximation is given by:

$$\begin{aligned} N_{xy} &= \frac{\pi^2}{2\left(\frac{a}{b}\right)^2 a^2 \tan\alpha} \left[\begin{array}{l} D_{11}\left[1 + 6\tan^2\alpha AR^2 + \tan^4\alpha AR^4\right] \\ \\ +2(D_{12} + 2D_{66})\left[AR^2 + \tan^2\alpha AR^4\right] + D_{22}AR^4 \end{array} \right] \\ &\text{with} \\ AR &= \left[\frac{D_{11}}{D_{11}\tan^4\alpha + 2(D_{12} + 2D_{66})\tan^2\alpha + D_{22}}\right]^{1/4} \\ 0 &= 3D_{11}AR^4\tan^4\alpha + \left(6D_{11}AR^2 + 2\left(D_{12} + 2D_{66}\right)AR^4\right)\tan^2\alpha \\ &\quad - \left(D_{11} + 2\left(D_{12} + 2D_{66}\right)AR^2 + D_{22}AR^4\right) \end{aligned} \tag{C.9}$$

The isotropic (metal) shear buckling edge load is given by:

$$N_{xy,m} = K_{xy} \frac{Et^3}{(1-\nu^2)b^2} \tag{C.10}$$

The K_{xy} term again depends on the ratio $\frac{a}{b}$ and is 5.25 as given by Roark *et al.* [130, p. 732].

C.1.3 Bi-axial compression buckling load

The bi-axial compression buckling load is again obtained from both Roark *et al.* and Kassapoglou. The applied edge loads in longitudinal and transverse direction are assumed equal. The composite and metal buckling loads are given by minimizations of respectively Equation C.11 and C.12 over m and n.

$$N_{xx,c} = \frac{\pi^2}{a^2\left(m^2 + n^2\left(\frac{a}{b}\right)^2\right)}\left[D_{11}m^4 + 2(D_{12} + 2D_{66})m^2n^2\left(\frac{a}{b}\right)^2 + D_{22}n^2\left(\frac{a}{b}\right)^4\right] \tag{C.11}$$

$$N_{xx,m} = K_{xx}\frac{Et^3}{1-\nu^2}\left(\frac{m^2}{a^2} + \frac{n^2}{b^2}\right) \quad \text{with} \quad K_{xx} = 0.823 \tag{C.12}$$

C.2 Distributions of damage and impactor characteristics

In the application chapter several histograms, and corresponding distribution fits are summarized. These distributions originate from a comparison of several distributions: (I) log-logistic, (II) Logistic, (III) LogNormal, (IV) Normal and (V) Weibull. The log-logistic, lognormal and Weibull fits considered both the two and three parts estimations. The indicated distributions were selected in line with the work of Chen *et al.* [2]. The goodness of fit is determined based on the χ^2-test. The results are summarized in Table C.6.

Table C.6: Summary of goodness of fit comparison of distributions using Chi-square test (Relative rank is shown in brackets)

	Goodness of Fit p-values of χ^2-test									
Distribution	**Measured**		**Measured**		**Estimated**		**Estimated**		**Estimated**[†]	
Distribution	**dent radius**		**dent depth**		**impact energy**		**impactor radius**		**impactor radius - V2**[†]	
Log-Logistic	0.23712	(5)	0.50299	(6)	0.10573	(5)	0.03411	(7)	0.80401	(4)
Log-Logistic (3P)	0.4881	(1)	0.59512	(4)	0.19016	(3)	0.43588	(3)	0.91647	(2)
Logistic	0.01344	(8)	0.000001	(7)	0.03542	(7)	0.17155	(5)	0.11936	(8)
lognormal	0.30563	(3)	0.80628	(2)	0.31192	(1)	0.07301	(6)	0.54535	(6)
lognormal (3P)	0.43453	(2)	0.78945	(3)	0.13261	(4)	0.50278	(2)	0.87878	(3)
Normal	0.03792	(7)	0.0000004	(8)	0.03945	(6)	0.20315	(4)	0.1579	(7)
Weibull	0.16161	(6)	0.80795	(1)	0.03019	(8)	0.50667	(1)	0.95792	(1)
Weibull (3P)	0.27084	(4)	0.57526	(5)	0.19345	(2)	~	(8)	0.79211	(5)

[†] The predictions on the contour boundary are excluded. This related to 1mm impactor radii.

Appendix D

Development of MIDAS code

D.1 Summary of MIDAS core components

Chapter 3 describes the analytical approach to model impact damage on aircraft structures. The main steps of the inductive and deductive procedures are summarized in Figure D.1 and D.2. The impact response essentially depend on the defined target of the impact event. This target is defined as *Target Plate* object in MATLAB programming environment. The definition of the plate object is described in Appendix D.2.

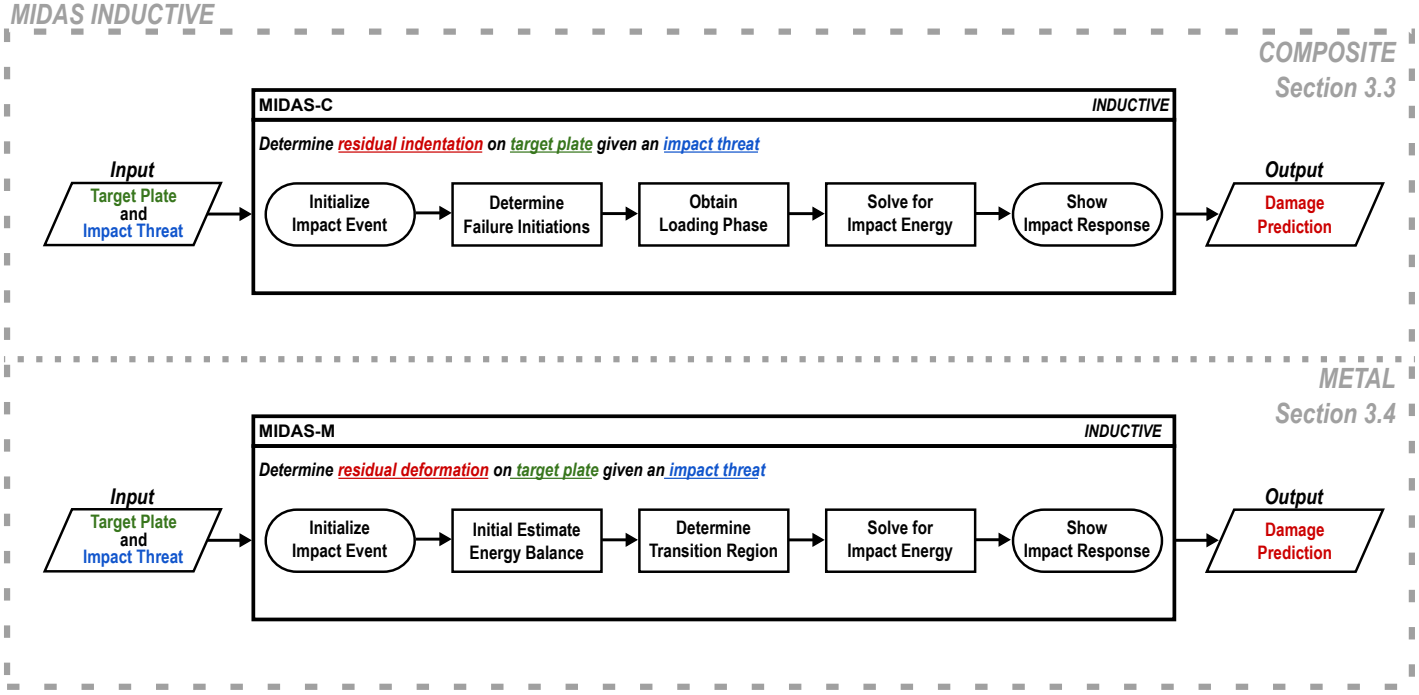

Figure D.1: Flowchart summary of inductive procedure of MIDAS

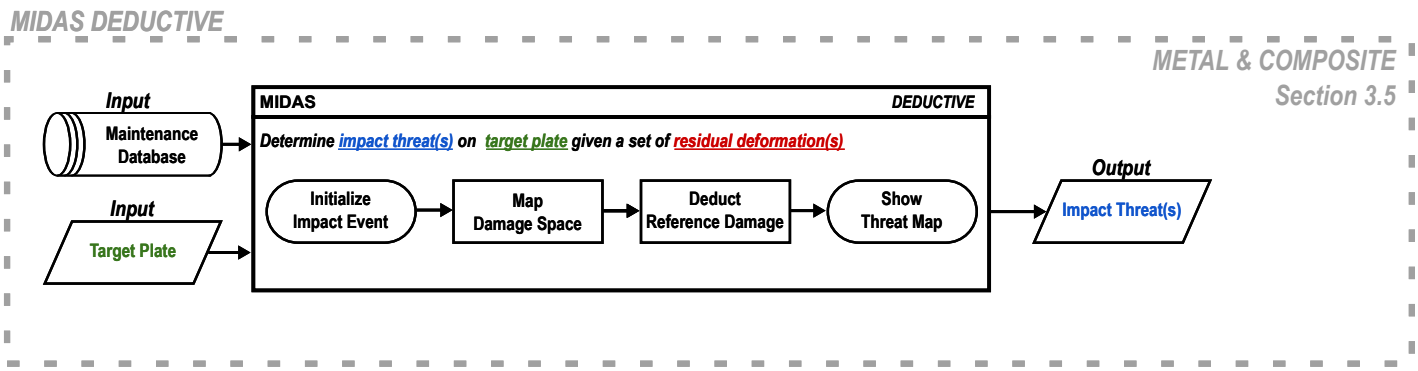

Figure D.2: Flowchart summary of deductive procedure of MIDAS

D.2 Plate object definition

The input of the inductive and deductive MIDAS procedures is an *Target Plate* object in MATLAB programming environment. This plate object is defined by the plate design (i.e. the plate dimensions and materials). As described in section 3.2, the impact event is dependent on the plate stiffness and deformation profiles. The *Target Plate* can be considered an isolated container (variable) with independent functions. All relevant plate properties are stored within this container, and the required characteristics are determined by the independent functions. The relevant steps are summarized in the flowchart shown in Figure D.3. This section elaborates on some of the relevant steps not described in chapter 3. The plate properties are a results of Classical Laminated Plate Theory, as summarized in Appendix D.2.1. The comparison between circular plate and plate theory approximations discussed in section 3.2 is reported in Appendix D.2.2. The determination of the circular plate stiffness terms and the delamination threshold properties requires the radially averaging of plate properties.

D.2.1 Review of Classical Laminated Plate Theory

The composite plate properties are obtained from Classical Laminated Plate Theory. This section briefly summarizes the key steps and equations, which are described by Kassapoglou [56]. The anisotropic nature of composite materials follows from the directional properties of the constituents. The relation between plate deformation and loading is given by Equation D.1.

$$\begin{Bmatrix} N_x \\ N_y \\ N_{xy} \\ M_x \\ M_y \\ M_{xy} \end{Bmatrix} = \begin{bmatrix} A_{11} & A_{12} & A_{16} & B_{11} & B_{12} & B_{16} \\ A_{21} & A_{22} & A_{26} & B_{21} & B_{22} & B_{26} \\ A_{61} & A_{62} & A_{66} & B_{61} & B_{62} & B_{66} \\ B_{11} & B_{12} & B_{16} & D_{11} & D_{12} & D_{16} \\ B_{21} & B_{22} & B_{26} & D_{21} & D_{22} & D_{26} \\ B_{61} & B_{62} & B_{66} & D_{61} & D_{62} & D_{66} \end{bmatrix} \begin{Bmatrix} \varepsilon_{xo} \\ \varepsilon_{yo} \\ \gamma_{xyo} \\ \kappa_x \\ \kappa_y \\ \kappa_{xy} \end{Bmatrix} \tag{D.1}$$

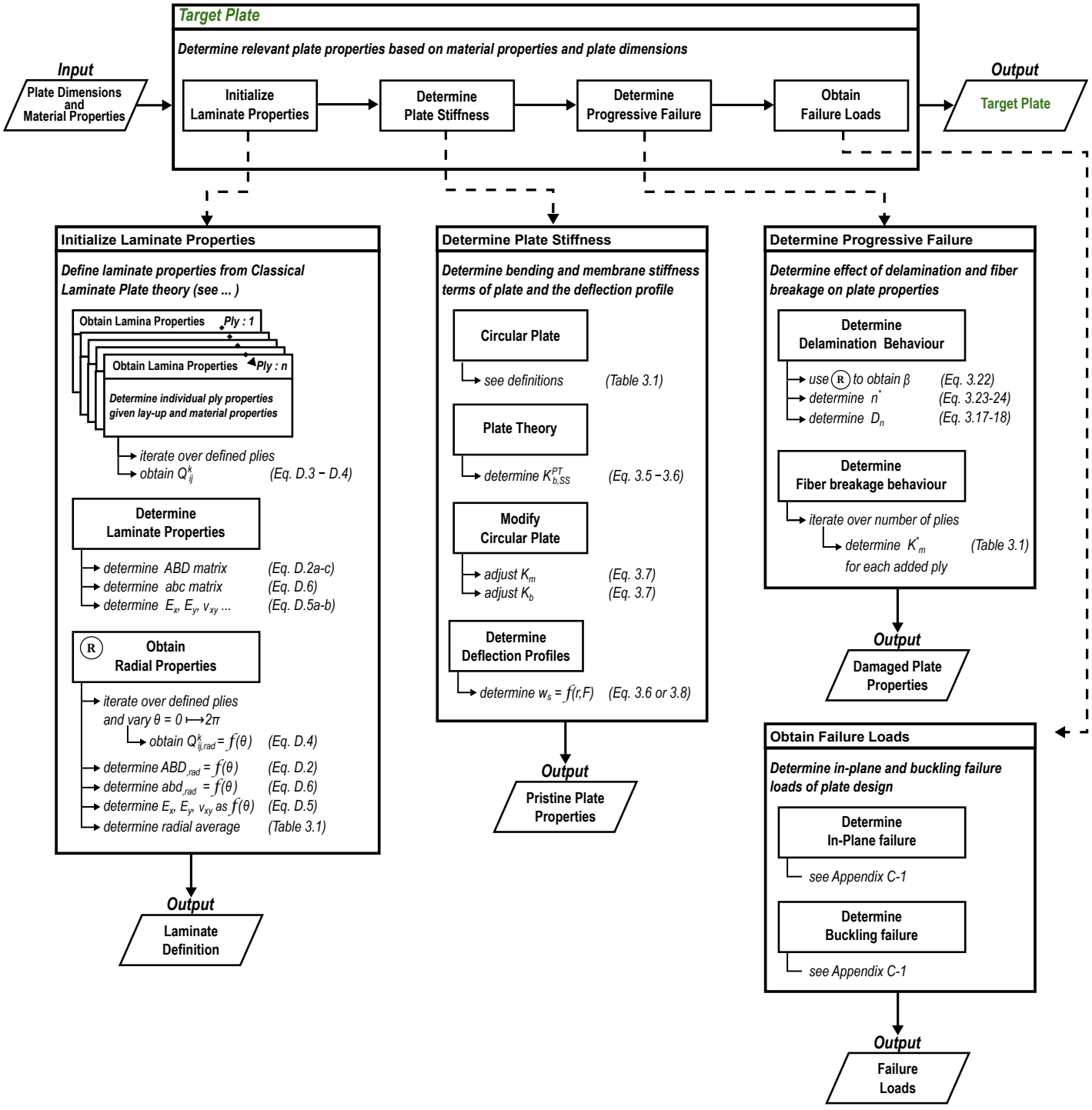

Figure D.3: Flowchart summary of plate object in MATLAB

in which the terms A_{ij}, B_{ij} and D_{ij} are defined by

$$A_{ij} = \sum_{k=1}^{n} Q_{ij}(z_k - z_{k-1}) \qquad \text{with} \quad i,j = 1,2,6 \tag{D.2a}$$

$$B_{ij} = \sum_{k=1}^{n} \frac{Q_{ij}}{2}(z_k^2 - z_{k-1}^2) \tag{D.2b}$$

$$D_{ij} = \sum_{k=1}^{n} \frac{Q_{ij}}{3}(z_k^3 - z_{k-1}^3) \tag{D.2c}$$

The summation covers the total number of plies (n), and the Q_{ij} terms refers to the individual plies (k) stiffness tensor elements. These stiffness tensors are defined in the global systems coordinate system (i.e. in case of an aircraft structure from front to aft). The individual ply stiffness tensor are obtained from their uni-direction properties rotated to obtain the global properties with respectively Equation D.3 and D.4.

$$Q_k^{UD} = \begin{bmatrix} Q_{xx} & Q_{xy} & 0 \\ Q_{xy} & Q_{yy} & 0 \\ 0 & 0 & Q_{ss} \end{bmatrix} = \begin{bmatrix} \dfrac{E_L}{1-\nu_{LT}\nu_{TL}} & \dfrac{\nu_{TL}E_L}{1-\nu_{LT}\nu_{TL}} & 0 \\ \dfrac{\nu_{TL}E_L}{1-\nu_{LT}\nu_{TL}} & \dfrac{E_T}{1-\nu_{LT}\nu_{TL}} & 0 \\ 0 & 0 & G_{LT} \end{bmatrix} \tag{D.3}$$

$$\begin{aligned}
Q_{11}^{(\theta)} &= m^4 Q_{xx} + n^4 Q_{yy} + 2m^2n^2 Q_{xy} + 4m^2n^2 Q_{ss} \\
Q_{22}^{(\theta)} &= n^4 Q_{xx} + m^4 Q_{yy} + 2m^2n^2 Q_{xy} + 4m^2n^2 Q_{ss} \\
Q_{12}^{(\theta)} &= m^2n^2 Q_{xx} + m^2n^2 Q_{yy} + (m^4 + n^4) Q_{xy} - 4m^2n^2 Q_{ss} \\
Q_{66}^{(\theta)} &= m^2n^2 Q_{xx} + m^2n^2 Q_{yy} - 2m^2n^2 Q_{xy} + (m^2 - n^2)^2 Q_{ss} \\
Q_{16}^{(\theta)} &= m^3n Q_{xx} - mn^3 Q_{yy} + (mn^3 - m^3n) Q_{xy} + 2(mn^3 - m^3n) Q_{ss} \\
Q_{26}^{(\theta)} &= mn^3 Q_{xx} - m^3n Q_{yy} + (m^3n - mn^3) Q_{xy} + 2(mn^3 - m^3n) Q_{ss}
\end{aligned} \tag{D.4}$$

in which E, G and ν refer to the Young modulus, shear modulus and the Poisson ratio. The subscripts L and T refer to the longitudinal and transverse direction, while $m = \cos(\theta)$ and $n = \sin(\theta)$. The laminate stiffness properties in different directions are defined for symmetric laminates by Equation D.5 using Equation D.6 for the a and d terms.

$$E_{1m} = \frac{1}{ta_{11}} \qquad E_{2m} = \frac{1}{ta_{22}} \qquad G_{12m} = \frac{1}{ta_{66}} \qquad \nu_{12m} = -\frac{a_{12}}{a_{11}} \qquad \nu_{21m} = -\frac{a_{12}}{a_{22}} \tag{D.5a}$$

$$E_{1b} = \frac{12}{t^3 d_{11}} \qquad E_{2b} = \frac{12}{t^3 d_{22}} \qquad G_{12b} = \frac{12}{t^3 d_{66}} \qquad \nu_{12b} = -\frac{d_{12}}{d_{11}} \qquad \nu_{21b} = -\frac{d_{12}}{d_{22}} \tag{D.5b}$$

$$\begin{bmatrix} a & b \\ b & d \end{bmatrix} = \begin{bmatrix} A & B \\ B & D \end{bmatrix}^{-1} = \begin{bmatrix} a_{11} & a_{12} & a_{16} & b_{11} & b_{12} & b_{16} \\ a_{21} & a_{22} & a_{26} & b_{21} & b_{22} & b_{26} \\ a_{61} & a_{62} & a_{66} & b_{61} & b_{62} & b_{66} \\ b_{11} & b_{12} & b_{16} & d_{11} & d_{12} & d_{16} \\ b_{21} & b_{22} & b_{26} & d_{21} & d_{22} & d_{26} \\ b_{61} & b_{62} & b_{66} & d_{61} & d_{62} & d_{66} \end{bmatrix} \tag{D.6}$$

The subscripts b and m refer to bending and membrane deformations. The use of stiffness definitions D.5a or D.5b depends on the deformation scenario. The bending and membrane stiffness approximations given in Table 3.1 for example use the radially averaged results of respectively D.5a or D.5b. On the other hand, the case study plate design summary in chapter 6 assumes membrane stiffness terms.

D.2.2 Comparison of plate stiffness approximations

In section 3.2 two alternative bending stiffness approximations are described. The circular plate approximation based on definitions from Shivakumar *et al.* [15] or rectangular plate definitions obtained from plate theory. This section compares the results of both approximations for metal and composite scenario's. The metal and composite material properties correspond to the properties defined in chapter 6. In Figure D.4 the effect of plate size and plate thickness for metals is compared, which shows a constant relative difference of approximately 7.5%.

However, the comparison in terms of changing aspect ratio shows increasing differences (see Figure D.5). The circular plate approximation remains constant, due to the inscribed circle approximation[1].

Larger differences are observed in case of composite plates. This is shown in Figure D.6. The relative difference between the laminates change depending on the aspect ratio. Laminate F is consistently under estimated by approximately 25%, while the percentage difference of Laminate QI increases from an over estimation of 10% to 25%.

[1]The inscribed circle refers to circle centered at the point of impact that reaches up to the nearest boundary. The results in a circle with a diameter equal to the smallest side of a rectangular plate in case of an impact on the plates center

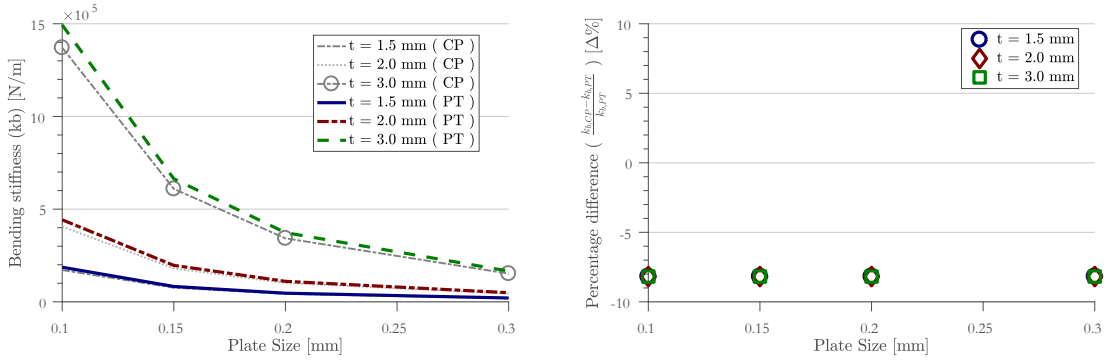

(a) Absolute bending stiffness **(b)** Percentage difference CP and PT

Figure D.4: Bending stiffness approximations as function of plate thickness and square plate size

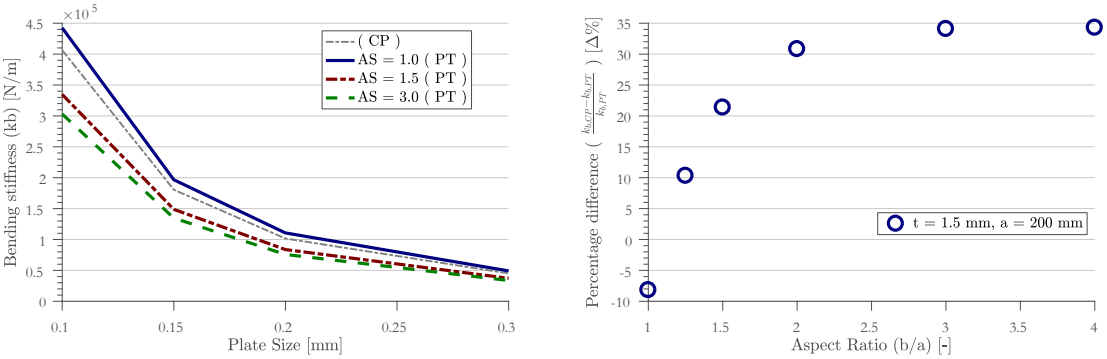

(a) Absolute bending stiffness **(b)** Percentage difference CP and PT

Figure D.5: Bending stiffness approximations as function of plate thickness and square plate size

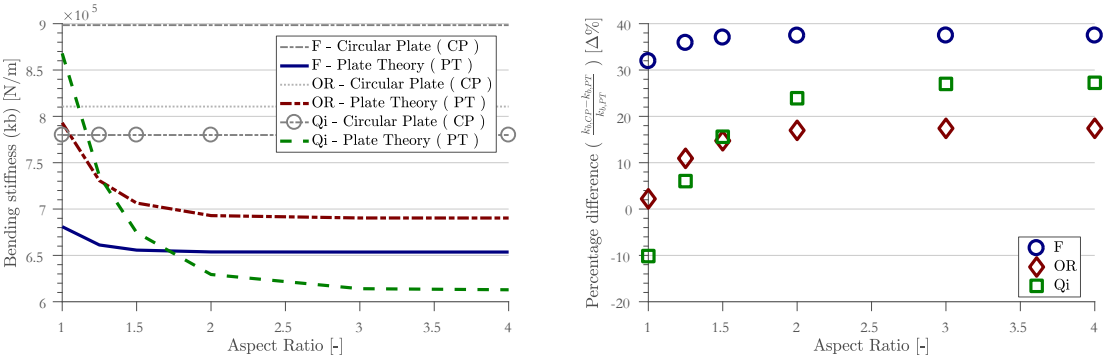

(a) Absolute bending stiffness **(b)** Percentage difference CP and PT

Figure D.6: Bending stiffness approximations as function of aspect ratio for various composite lay ups

Appendix E

additional Verification

E.1 Effect of friction coefficient in FEM

As indicated in subsection 4.1.1, a friction coefficient of 0.15 is used throughout this study within the FEM simulations. This section elaborates on a range of possible friction coefficients and compares the effect on the final results. The comparative study of friction coefficient (μ) is based on the 7.92 m/s impact reference case of Fagerholt *et al.* [18]. The FEM settings are identical to the settings described in subsection 4.2.1 with the exception of the friction coefficient (i.e. which is varied between 0.05 and 2.0). A mesh size of 1mm us, which is considered sufficiently converged (see Figure 4.2a and 4.2b). The following characteristic parameters are compared in the evaluation of range of the friction coefficients:

- **I** Artificial strain energy
- **II** Max displacement
- **III** Max force

The max displacement and force are relevant characteristics in the verification steps, as used in subsection 4.2.2. These indicate the end of loading condition for a single impact scenario. The artificial strain energy is used to evaluated convergence of a single FEM simulations[1]. The percentage difference of the artificial strain energy and max displacement are within 1% as shown in Figure E.1. The percentage difference is taken with respect to the μ = 0.15 used in this thesis.

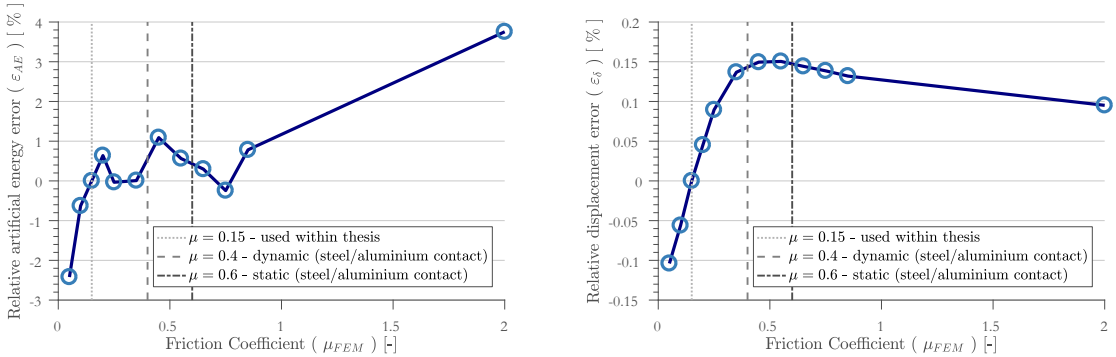

(a) Artificial strain energy **(b)** Max displacement

Figure E.1: Percentage difference of a range friction coefficients w.r.t to μ = 0.15

Larger differences are observed in terms of peak force, as shown in Figure E.2. However, over the range of friction coefficients, the differences are within 10%. The friction coefficient definition in ABAQUS originates from Coulomb friction laws. Typical reported values for contact between aluminum and steel surfaces are 0.6 and 0.4 for respectively static and dynamic conditions. A friction coefficient of 0.4 could therefore be seen as more appropriate, but the difference w.r.t the used 0.15 is only 2%. The used friction coefficient is therefore still assumed as an appropriate setting to perform the verification study.

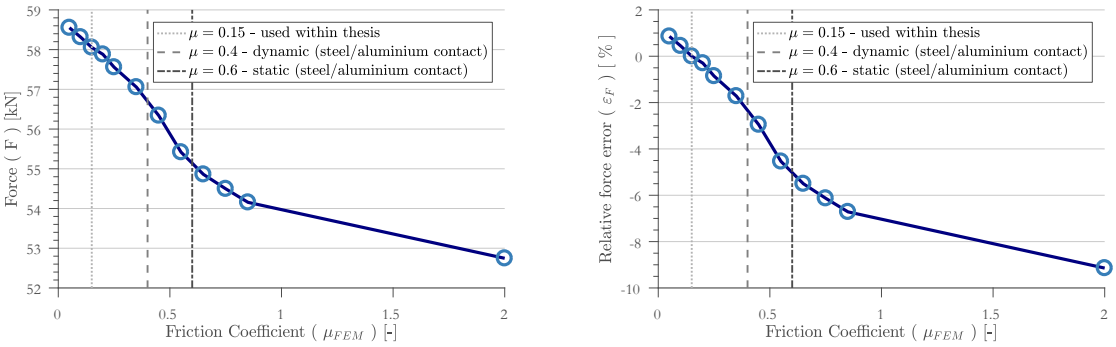

(a) Absolute peak force results **(b)** Percentage difference w.r.t to μ = 0.15

Figure E.2: Variation of peak force for a range friction coefficients

[1] A single FEM simulation does not account for a converged result, but the magnitude of the artificial strain energy (AE) can be used as measure of convergence. The reference case of μ = 0.15 is converged, and similar AE values are therefore assumed sufficiently converged.

Bibliography

[1] L. Cook, A. Boulic, D. Harris, P. Bellamy, and P. Irving, *Reliability of Damage Detection in Advanced Composite Aircraft Structures*, Tech. Rep. (Safety Regulation Group, Cranfield University, 2013).

[2] X. Chen, H. Ren, and C. Bil, *Inspection Intervals Optimization for Aircraft Composite Structures Considering Dent Damage,* Journal of Aircraft **51**, 303 (2014).

[3] B. Bachtel, *Foreign Object Debris and Damage Prevention,* AER0 (1998).

[4] I. Mccreary, *The economic cost of FOD to airlines,* (2008).

[5] C. Prather, M. Smalley, B. Clifton, and J. Johnston, *Airport Cooperative Research Program*, Tech. Rep. (Transportation Research Board, Washington, D.C., 2011).

[6] H. Kim, G. K. DeFrancisci, and Z. M. Chen, *Ground vehicle blunt impact damage formation to composite aircraft structures,* Advanced Composite Materials **23**, 53 (2013).

[7] D. Mohotti, M. Ali, T. Ngo, J. Lu, P. Mendis, and D. Ruan, *Out-of-plane impact resistance of aluminium plates subjected to low velocity impacts,* Materials and Design **50**, 413 (2013).

[8] W. J. Cantwell and J. Morton, *The impact resistance of composite materials—a review,* Composites **22**, 347 (1991).

[9] U. Polimeno and M. Meo, *Detecting barely visible impact damage detection on aircraft composites structures,* Composite Structures **91**, 398 (2009).

[10] G. A. O. Davies and X. Zhang, *Impact damage prediction in carbon composite structures,* International Journal of Impact Engineering **16**, 149 (1993).

[11] S. Abrate, *Modeling of impacts on composite structures,* Composite Structures **51**, 129 (2001).

[12] G. A. O. Davies and R. Olsson, *Impact on composite structures,* The Aeronautical Journal **108**, 541 (2004).

[13] B. C. Simonsen and L. P. Lauridsen, *Energy absorption and ductile failure in metal sheets under lateral indentation by a sphere,* International Journal of Impact Engineering **24**, 1017 (2000).

[14] Y.-w. Lee, J. C. Woertz, and T. Wierzbicki, *Fracture prediction of thin plates under hemi-spherical punch with calibration and experimental verification,* International Journal of Mechanical Sciences **46**, 751 (2004).

[15] K. N. Shivakumar, W. Elber, and W. Illg, *Prediction of Impact Force and Duration Due to Low-Velocity Impact on Circular Composite Laminates,* Journal of Applied Mechanics **52**, 674 (1983).

[16] D. S. Cairns, *A Simple, Elasto-Plastic Contact Law for Composites,* Journal of Reinforced Plastics and Composites **10**, 423 (1991).

[17] R. Olsson and T. B. Block, *Criteria for skin rupture and core shear cracking induced by impact on sandwich panels,* Composite Structures **125**, 81 (2015).

[18] E. Fagerholt, F. Grytten, B. E. Gihleengen, M. Langseth, and T. B??rvik, *Continuous out-of-plane deformation measurements of AA5083-H116 plates subjected to low-velocity impact loading,* International Journal of Mechanical Sciences **52**, 689 (2010).

[19] C. S. Lopes, O. Seresta, Y. Coquet, Z. Gürdal, P. P. Camanho, and B. Thuis, *Low-velocity impact damage on dispersed stacking sequence laminates. Part I: Experiments,* Composites Science and Technology **69**, 926 (2009).

[20] H. Morita, A. Hamamoto, T. Adachi, and K. Matsumoto, *Influence of impact velocity and lay-up parameter on impact damage resistance of CF/PEEK laminates,* in *36th Structures, Structural Dynamics and Materials Conference*, Vol. 2 (American Institute of Aeronautics and Astronautics, Reston, Virigina, 1995).

[21] V. S. Dhanisetty, W. J. Verhagen, and R. Curran, *Multi-criteria weighted decision making for operational maintenance processes,* Journal of Air Transport Management (2017), 10.1016/j.jairtraman.2017.09.005.

[22] L. Cook, *Visual inspection reliability for composite aircraft structures*, Ph.D. thesis, Cranfield University (2009).

[23] *Definition of impact in English,* (2018).

[24] R. Olsson, *Engineering method for prediction of impact response and damage in sandwich panels,* Journal of Sandwich Structures and Materials **4**, 2 (2002).

[25] H. Kim, G. Defrancisci, D. Whisler, and J. Rhymer, *Impact Damage Formation on Composite Aircraft Structures,* Federal Aviation Administration Joint Advanced Materials & Structures (JAMS) , 1 (2015).

[26] P. Haase and Z. Mikulik, *Composite damage metrics and inspection*, Tech. Rep. (European Aviation Safety Agency (EASA), Hamburg, 2012).

[27] J. Rhymer, H. Kim, and D. Roach, *The damage resistance of quasi-isotropic carbon/epoxy composite tape laminates impacted by high velocity ice,* Composites Part A: Applied Science and Manufacturing **43**, 1134 (2012).

[28] H. Kim and K. T. Kedward, *Modeling hail ice impacts and predicting impact damage initiation in composite structures,* AIAA Journal **38**, 1278 (2000).

[29] S. Neidigk, *Detection and characterization of hail impact damage in carbon fiber aircraft structure*, Tech. Rep. (Federal Aviation Administration, New Jersey, 2013).

[30] P. Field, W. Hand, G. Cappelluti, A. McMillan, A. Foreman, and M. Willows, *Hail Threat Standardisation*, Tech. Rep. (EASA, 2010).

[31] H. Kim, D. A. Welch, and K. T. Kedward, *Experimental investigation of high velocity ice impacts on woven carbon/epoxy composite panels,* Composites Part A: Applied Science and Manufacturing **34**, 25 (2003).

[32] D. Whisler and H. Kim, *Effect of impactor radius on low-velocity impact damage of glass / epoxy composites,* Journal of Composite Materials **46**, 3137 (2012).

[33] C. Fualdes and E. Morteau, *Composites @ Airbus damage tolerance methodology,* (2006).

[34] I. McCreary, *Runway Safety*, Tech. Rep. (Insight SRI, Washington, 2011).

[35] J. Hilkevitch, *Airports zoom in on threat of debris,* (2008).

[36] Federal Aviation Administration (FAA), *Airport Foreign Object Debris (FOD) Management - AC 150/5210-24,* (2010).

[37] S. N. Nguyen, E. S. Greenhalgh, J. M. R. Graham, A. Francis, and R. Olsson, *Runway debris impact threat maps for transport aircraft,* Aeronautical Journal **118**, 229 (2014).

[38] H. Kim, J. Halpin, and G. DeFrancisci, *Impact Damage of Composite Structures,* in *Long-Term Durability of Polymeric Matrix Composites*, edited by K. V. Pochiraju, G. P. Tandon, and G. A. Schoeppner (Springer US, Boston, MA, 2012) Chap. 5, pp. 143–180.

[39] N. Toso and A. Johnson, *EASA - LIBCOS âĂŞ Significance of Load upon Impact Behaviour of Composite Structure*, Tech. Rep. (German Aerospace Center (DLR), Stuttgart, 2011).

[40] S. Heimbs, *Computational methods for bird strike simulations: A review,* Computers and Structures **89**, 2093 (2011).

[41] S. Georgiadis, A. J. Gunnion, R. S. Thomson, and B. K. Cartwright, *Bird-strike simulation for certification of the Boeing 787 composite moveable trailing edge,* Composite Structures **86**, 258 (2008).

[42] EASA, *Protection from debris impacts,* amending Decision 2003/2/RM (2013).

[43] *Transport Safety Report - Ground operations occurrences at Australian airports 1998 to 2008*, Tech. Rep. ((ATSB) Australian Transport Safety Burea, 2009).

[44] A. D. Balk, *Safety of ground handling*, Tech. Rep. (Nationaal Lucht- en Ruimtevaartlaboratorium (NLR), 2008).

[45] M. Lacagnna, *Progress report on FSF efforts to stem the toll of ground accidents,* AEROSAFTYWORLD , 20 (2007).

[46] H. U. Kim, T. U. Hahn, G. U. DeFrancisci, D. U. Whisler, J. U. Rhymer, and Z. U. Chen, *Impact Damage Formation on Composite Aircraft Structures,* FAA Joint Advanced Materials and Structures Center of Excellence Meeting , 1 (2009).

[47] H. Kim, *Impact Damage Formation on Composite Aircraft Structures,* Ucsd Faa Jams , 1 (2012).

[48] G. K. Defrancisci, Z. M. Chen, and H. Kim, *Blunt impact damage formation in frame and stringer stiffened composites panels,* Proceeding of The 18th International Conference on Composite Materials (2011).

[49] G. Defrancisci, *High Energy Wide Area Blunt Impact on Composite Aircraft Structures*, Ph.D. thesis, UNIVERSITY OF CALIFORNIA (2013).

[50] Z. U. Chen, *Experimental and Numerical Investigation of Wide Area Blunt Impact Damage to Composite Aircraft Structures*, Ph.D. thesis, University of California San Diego (2015).

[51] P. Haase, P. Bishop, R. S. Thomson, E. Isambert, S. Waite, and E. G. Sanchez, *CODAMEIN-II - Composite Damage Metrics and Inspection (high energy blunt impact threat)*, Tech. Rep. (Bishop GmbH 0 Aeronautical Engineers, Hamburg, 2011).

[52] E.-H. Kim, M.-S. Rim, I. Lee, and T.-K. Hwang, *Composite damage model based on continuum damage mechanics and low velocity impact analysis of composite plates,* Composite Structures **95**, 123 (2013).

[53] C. T. A. T. T. Kassapoglou, *Modeling the Effect of Damage in Composite Structures : Simplified Approaches.* (2015).

[54] A. International, *ASTM D7136/D7136M-15 Standard Test Method for Measuring the Damage Resistance of a Fiber-Reinforced Polymer Matrix Composite to a Drop-Weight Impact Event*, Tech. Rep. (ASTM International, West Conshohocken, PA, 2015).

[55] EASA, *AMC 20-29 : Composite Aircraft Structure,* Acceptable Means of Compliance (AMC) , 1 (2010).

[56] C. T. A. T. T. Kassapoglou, *Design and Analysis of Composite Structures : with Applications to Aerospace Structures.* (2013).

[57] H. Karlsen, *UK Aerospace Maintenance, repair and Overhaul & Logistic Industry Analysis*, Tech. Rep. 275 (UK Department for Business Innovation & Skilss, London, 2016).

[58] R. Pavkovic, A. Dramsi, and J. Armstrong, *Maintenance, Repair and Overhaul (MRO)*, Tech. Rep. (Capgemini, 2009).

[59] K. B. Katnam, L. F. M. Da Silva, and T. M. Young, *Bonded repair of composite aircraft structures: A review of scientific challenges and opportunities,* Progress in Aerospace Sciences **61**, 26 (2013).

[60] J. H. Heida and J. M. Müller, *In-service inspection and monitoring of composite aerospace structures (NLR-TP-2013-435)*, Tech. Rep. (National Aerospace Laboratory (NLR), Amsterdam, 2013).

[61] C. Richard Cassady, W. Paul Murdock, and E. A. Pohl, *Selective maintenance for support equipment involving multiple maintenance actions,* European Journal of Operational Research **129**, 252 (2001).

[62] D. P. Roach and T. M. Rice, *A Quantitative Assessment of Advanced Nondestructive Inspection Techniques for Detecting Flaws in Composite Laminate Aircraft Structures,* , 348 (2016).

[63] S. Waite, *MIL-17 Maintenance Workshop*, Tech. Rep. July (European Aviation Safety Agency, Chicago, 2006).

[64] J. Baaran, *Study on visual inspection of composite structures EASA.2007/3,* (2009).

[65] *CAP 562 Civil Aircraft Airworthiness Information and Procedures,* (2013).

[66] A. Baker, S. Dutton, and D. Kelly, *Repair Technology,* in *Composite Materials for Aircraft Structures* (2004) Chap. 10, pp. 369–402.

[67] C. Kassapoglou, K. Rangelov, and S. Rangelov, *Repair of Composites: Design Choices Leading to Lower Life-Cycle Cost,* Applied Composite Materials **24**, 945 (2017).

[68] M. A. Caminero, S. Pavlopoulou, M. Lopez-Pedrosa, B. G. Nicolaisson, C. Pinna, and C. Soutis, *Analysis of adhesively bonded repairs in composites: Damage detection and prognosis,* Composite Structures **95**, 500 (2013).

[69] A. Baker, *A Proposed Approach for Certification of Bonded Composite Repairs to Flight-Critical Airframe Structure,* Applied Composite Materials **18**, 337 (2011).

[70] A. Baker, A. Gunnion, and J. Wang, *On the certification of bonded repairs to primary composite aircraft components,* Journal of Adhesion **91**, 4 (2015).

[71] M. Richardson and M. Wisheart, *Review of low-velocity impact properties of composite materials,* Composites Part A: Applied Science and Manufacturing **27**, 1123 (1996).

[72] B. Liu, R. Villavicencio, and C. Guedes Soares, *On the failure criterion of aluminum and steel plates subjected to low-velocity impact by a spherical indenter,* International Journal of Mechanical Sciences **80**, 1 (2014).

[73] P. Beynet and R. Plunkett, *Plate Impact and Plastic Deformation by Projectiles,* Experimental Mechanics **11**, 64 (1971).

[74] T. A. Sebaey, E. V. González, C. S. Lopes, N. Blanco, and J. Costa, *Damage resistance and damage tolerance of dispersed CFRP laminates: The bending stiffness effect,* Composite Structures **106**, 30 (2013).

[75] H. Liu, B. G. Falzon, and W. Tan, *Predicting the Compression-After-Impact (CAI) strength of damage-tolerant hybrid unidirectional/woven carbon-fibre reinforced composite laminates,* Composites Part A: Applied Science and Manufacturing **105**, 189 (2018).

[76] S. Abrate, *Impact on Laminated Composites: Recent Advances,* Applied Mechanics Reviews **47**, 517 (1994).

[77] H. Kim, G. Defrancisci, D. Whisler, and J. Rhymer, *Impact Damage Formation on Composite Aircraft Structures,* in *Federal Aviation Administration Joint Advanced Materials & Structures (JAMS)* (2009) pp. 1–37.

[78] S. Abrate, *Impact on Laminated Composite Materials,* Applied Mechanics Reviews **44**, 155 (1991).

[79] A. Wagih, P. Maimí, E. V. González, N. Blanco, J. R. S. De Aja, F. M. De La Escalera, R. Olsson, and E. Alvarez, *Damage sequence in thin-ply composite laminates under out-of-plane loading,* Composites Part A: Applied Science and Manufacturing **87**, 66 (2016).

[80] G. A. Schoeppner and S. Abrate, *Delamination threshold loads for low velocity impact on composite laminates,* Composites: Part A **31**, 903 (2000).

[81] R. Olsson, *Analytical prediction of damage due to large mass impact on thin ply composites,* Composites Part A: Applied Science and Manufacturing **72**, 184 (2015).

[82] M. R. M. Suki and M. Jamal-Omidi, *A Numerical Study on Aluminum Plate Response under Low Velocity Impact,* International Journal of Engineering **30**, 440 (2017).

[83] D. S. Cairns, *A Simple, Elasto-Plastic Contact Law for Composites,* Journal of Reinforced Plastics and Composites **10**, 423 (1991).

[84] P. O. Sjöblom, T. J. Hartness, and T. M. Cordell, *Low-Velocity Impact Testing Composite Materials Tholes,* Journal of COMPOSITE MATERIALS **22**, 30 (1988).

[85] E. V. González, P. Maimí, P. P. Camanho, C. S. Lopes, and N. Blanco, *Effects of ply clustering in laminated composite plates under low-velocity impact loading,* Composites Science and Technology **71**, 805 (2011).

[86] R. Olsson, M. V. Donadon, and B. G. Falzon, *Delamination threshold load for dynamic impact on plates,* International Journal of Solids and Structures **43**, 3124 (2006).

[87] R. Olsson, *Mass criterion for wave controlled impact response of composite plates,* Composites Part A: Applied Science and Manufacturing **31**, 879 (2000).

[88] W. He, Z. Guan, X. Li, and D. Liu, *Prediction of permanent indentation due to impact on laminated composites based on an elasto-plastic model incorporating fiber failure,* Composite Structures **96**, 232 (2013).

[89] T. A. Sebaey, E. V. González, C. S. Lopes, N. Blanco, P. Maimí, and J. Costa, *Damage resistance and damage tolerance of dispersed CFRP laminates: Effect of the mismatch angle between plies,* Composite Structures **101**, 255 (2013).

[90] N. Razali, M. T. H. Sultan, F. Mustapha, N. Yidris, and M. R. Ishak, *Impact Damage on Composite Structures âĂŞ A Review,* The International Journal Of Engineering And Science **3**, 8 (2014).

[91] A. Poursartip, D. Delfosse, and G. Pageau, *Instrumented impact testing at high velocities,* Journal of Composites, **15** (1993).

[92] S. N. A. Safri, M. T. H. Sultan, N. Yidris, and F. Mustapha, *Low velocity and high velocity impact test on composite materials âĂŞ A review,* The International Journal of Engineering and Science (IJES) **3**, 50 (2014).

[93] *ASTM D6264/D6264M-17 Standard Test Method for Measuring the Damage Resistance of a Fiber-Reinforced Polymer-Matrix Composite to a Concentrated Quasi-Static Indentation Force*, Tech. Rep. (ASTM International, West Conshohocken, PA,, 2017).

[94] *ASTM D5628-10 Standard Test Method for Impact Resistance of Flat, Rigid Plastic Specimens by Means of a Falling Dart (Tup or Falling Mass)*, Tech. Rep. (ASTM International, West Conshohocken, PA, 2010).

[95] A. S. Yigit and A. P. Christoforou, *Limits of asymptotic solutions in low-velocity impact of composite plates,* Composite Structures **81**, 568 (2007).

[96] H. Singh and P. Mahajan, *Analytical modeling of low velocity large mass impact on composite plate including damage evolution,* Composite Structures **149**, 79 (2016).

[97] F. Esrail and C. Kassapoglou, *An efficient approach for damage quantification in quasi-isotropic composite laminates under low speed impact,* Composites Part B: Engineering **61**, 116 (2014).

[98] R. Olsson, *Closed form prediction of peak load and delamination onset under small mass impact,* Composite Structures **59**, 341 (2003).

[99] A. P. Christoforou and A. S. Yigit, *Characterization of impact in composite plates,* Composite Structures **43**, 15 (1998).

[100] A. P. Christoforou and A. S. Yigit, *Scaling of low-velocity impact response in composite structures,* Composite Structures **91**, 358 (2009).

[101] R. OLSSON, *Impact response of orthotropic composite plates predicted from a one-parameter differential equation,* AIAA Journal **30**, 1587 (1992).

[102] A. P. Christoforou, A. S. Yigit, and M. Majeed, *Low-Velocity Impact Response of Structures With Local Plastic Deformation: Characterization and Scaling,* Journal of Computational and Nonlinear Dynamics **8**, 011012 (2012).

[103] T. M. Tan and C. T. Sun, *Use of statical indentation laws in the impact analysis of laminated composite plates,* Journal of Applied Mechanics **52**, 6 (1985).

[104] N. Jones, *Impact loading of ductile rectangular plates,* Thin-Walled Structures **50**, 68 (2012).

[105] M. Langseth and P. K. Larsen, *The behaviour of square steel plates subjected to a circular blunt ended load,* International Journal of Impact Engineering **12**, 617 (1992).

[106] T. A. Sebaey, E. V. González, C. S. Lopes, N. Blanco, and J. Costa, *Damage resistance and damage tolerance of dispersed CFRP laminates: Effect of ply clustering,* Composite Structures **106**, 96 (2013).

[107] E. Fuoss, P. V. Straznicky, and C. Poon, *Effects of stacking sequence on the impact resistance in composite laminates. Part 1: Parametric study,* Composite Structures **41**, 67 (1998).

[108] L. S. Kistler and A. M. Waas, *On the response of curved laminated panels subjected to transverse impact loads,* International Journal of Solids and Structures **36**, 1311 (1999).

[109] A. Rastegari, A. Salonen, M. Bengtsson, and M. Wiktorsson, *Condition Based Maintenance in Manufacturing Industries: Introducing Current Industrial Practice and Challenges,* ICPR Parana; Brazil **28** (2013).

[110] A. P. Christoforou, *Impact dynamics and damage in composite structures,* Composite Structures **52**, 181 (2001).

[111] R. L. Taylor and S. Govindjee, *Solution of Clamped Rectangular Plate Problems*, Tech. Rep. (University of California, Berkeley, 2002).

[112] a. S. Yigit and a. P. Christoforou, *On the impact of a spherical indenter and an elastic-plastic transversely isotropic half space,* Composites Engineering **4**, 1143 (1994).

[113] R. Olsson, *Analytical prediction of large mass impact damage in composite laminates,* Composites Part A: Applied Science and Manufacturing **32**, 1207 (2001).

[114] G. A. O. Davies and P. Robinson, *Predicting Failure by Debonding/Delamination,* in *AGARD Conf. Proc.*, December (Patras, 1992) pp. 51–58.

[115] H. Suemasu and O. Majima, *Multiple delaminations and their severity in nonlinear circular plates subjected to concentrated loading,* Journal of Composite Materials **32**, 123 (1998).

[116] S. Timoshenko and S. Woinowsky-Krieger, *Thoery of Plates and Shells*, 2nd ed. (McGraw-Hill, 1959) p. 591.

[117] R. Olsson, *Analytical model for delamination growth during small mass impact on plates,* International Journal of Solids and Structures **47**, 2884 (2010).

[118] T. A. Sebaey and E. Mahdi, *Using thin-plies to improve the damage resistance and tolerance of aeronautical CFRP composites,* Composites Part A: Applied Science and Manufacturing **86**, 31 (2016).

[119] K. Levin, *Characterization of delamination and fiber fractures in carbon fiber reinforced plastics induced from impact,* in *Mechanical Behaviour of Materials VI* (Elsevier, 1992) pp. 519–524.

[120] D. Liu, *Impact-Induced Delamination - A view of bending stiffness mismatching,* Composite Materials **22**, 674 (1988).

[121] E. Fuoss, P. V. Straznicky, and C. Poon, *Effects of stacking sequence on the impact resistance in composite laminates. Part 2: prediction method,* Composite Structures **41**, 177 (1998).

[122] A. Big-Alabo, P. Harrison, and M. P. Cartmell, *Contact model for elastoplastic analysis of half-space indentation by a spherical impactor,* Computers and Structures **151**, 20 (2015).

[123] Dassault Systèmes, *ABAQUS Documentation*, 6th ed. (Providence, RI, USA, 2013).

[124] F. Grytten, T. Børvik, O. S. Hopperstad, and M. Langseth, *Low velocity perforation of AA5083-H116 aluminium plates,* International Journal of Impact Engineering **36**, 597 (2009).

[125] J. Zhu, *Investigation of low velocity im- pact on advanced hybrid laminates*, Tech. Rep. (Delft University of Technology, Delft, 2018).

[126] C. A. Baptista, A. M. Adib, M. A. Torres, and V. A. Pastoukhov, *Describing fatigue crack growth and load ratio effects in Al 2524 T3 alloy with an enhanced exponential model,* Mechanics of Materials **51**, 66 (2012).

[127] L. R. Botvina, G. I. Nesterenko, A. P. Soldatenkov, Y. A. Demina, and A. A. Sviridov, *Development of short fatigue cracks in aluminum alloy 2524-T3 specimens,* Russian Metallurgy (Metally) **2017**, 322 (2017).

[128] C. S. Lopes, *Damage and Failure of Non-Conventional Composite Laminates*, Ph.D. thesis, TU Delft (2009).

[129] International Civil Aviation Organization, *Safety Management Manual (SMM)* (International Civil Aviation Organization, 2013).

[130] R. J. Roark, W. C. Young, and R. Plunkett, *Journal of Applied Mechanics*, Vol. 43 (1976) p. 522.